

Sensitivity and Backgrounds of Phase-I and II of the COMET Experiment

Benjamin Edward Krikler
of Imperial College London

A dissertation submitted to Imperial College London
for the degree of Doctor of Philosophy

Abstract

Declaration

This dissertation is the result of my own work, except where explicit reference is made to the work of others, and has not been submitted for another qualification to this or any other university. This dissertation does not exceed the word limit for the respective Degree Committee.

Benjamin Edward Krikler

Acknowledgements

Contents

1. Theory	2
2. The COMET Experiment	4
2.1. Overview of Signal and Backgrounds	5
2.2. General Experimental Techniques	8
2.2.1. Proton Beam Energy and Production Target	8
2.2.2. Particle Transport through Bent Solenoids	9
2.2.3. Stopping Target Material and Beam Pulsing	12
2.3. COMET Phase-I	15
2.4. COMET Phase-II	17
2.5. Schedule and Status	19
3. Offline Software and The COMET Simulation	23
3.1. Developing the COMET Offline Framework	23
3.2. Overview of ICEDUST	26
3.3. The COMET Simulation	28
3.3.1. Handling Geometry	30
3.3.2. Field Calculation	33
3.3.3. Production Target Simulations	36
3.3.4. Extending the Geant4 Physics Modelling	38
4. Phase-II Optimisation	44
4.1. Optimisation Strategy	44
4.2. Production Target Optimisation	46
4.2.1. Configuration	46
4.2.2. Length Scan	47
4.2.3. Radius scan	49
4.2.4. Final Result	52

4.3.	Dipole Strengths of the Muon Beamline	53
4.3.1.	Large-sample Production Target Simulation	53
4.3.2.	The Optimised Dipole Field Strengths	54
4.4.	Electron Spectrometer's Dipole	56
4.4.1.	Method and Potential Short-comings	56
4.4.2.	Results	57
4.5.	Stopping Target Position	60
4.6.	Collimators in the Muon Beamline	66
4.6.1.	Collimator Placement	67
4.6.2.	Collimator Height Optimisation	70
4.7.	The Beam and Decay-in-Orbit Blockers	74
4.8.	Summary of optimised parameters	77
4.9.	Future optimisations	78
5.	Phase-II Signal Sensitivity	80
6.	Phase-II Backgrounds	81
6.1.	Antiproton Induced Backgrounds	81
6.1.1.	Antiproton Production Rate and Spectrum	81
6.1.2.	Simulating Antiprotons	84
6.1.3.	Antiproton Transmission	85
6.1.4.	Delayed Pion Production	85
A.	Drifts in a Bent Solenoid	87
A.1.	Uniform Solenoidal Field	87
A.2.	Field in a Bent Solenoid	87
A.3.	Drift Calculation	88
A.3.1.	Gradient Drift	88
B.	Kinematic End-point for Anti-proton Production	90
C.	Revisiting the Stopping Target Region	91
List of Acronyms		93
Bibliography		94

Chapter 1.

Theory

1. "Who ordered that?" – The author upon presentation of 'ika-no-ikizukuri' (live squid sashimi), in Fukuoka, North Kyushu
2. History of the muon and its importance to the development of the standard model
3. Lepton Flavour: Neutrinos and the Charged Leptons
4. Muon-to-electron Conversion and the Physics of Muonic Atoms

Chapter 2.

The COMET Experiment

The COMET experiment will search for COherent Muon to Electron Transitions with a single-event-sensitivity of around 3×10^{-17} . This amounts to an improvement of four orders of magnitude compared to the current limit [11] which requires some significant changes to the way the experiment operates compared to its predecessor.

Reaching such a sensitivity requires that COMET stops many muons in aluminium, maintaining a high signal acceptance, whilst suppressing potential background sources to well below a single event during the lifetime of the experiment. This tension between simultaneously high signal sensitivity and background suppression can be translated into the more specific requirements of:

- a very high intensity muon beam,
- a low energy muon beam,
- a thin stopping target and low material budget detector,
- the use of timing information of signal process with respect to backgrounds.

The design of COMET realises these goals by using several novel experimental techniques, and as such it has been decided to operate in two stages, Phase-I and Phase-II. Phase-I aims both to help understand these techniques, the muon beam, and key backgrounds rates, as well as making an intermediate measurement of μ - e conversion at a sensitivity of 3×10^{-15} —two orders of magnitude better than the SINDRUM-II experiment. Phase-II will follow and should achieve the final objective of 3×10^{-17} .

2.1. Overview of Signal and Backgrounds

To understand the design of both phases of COMET a simple appreciation of the signal and types of backgrounds that must be considered is necessary.

From an experimental perspective, μ - e conversion is attractive because its signal is so simple: a single monoenergetic electron at close to the muon mass of 105 MeV/c, given by:

$$E_e = M_\mu - E_{\mu,\text{binding}} - E_{\text{recoil}} \quad (2.1)$$

where $M_\mu = 105.66 \text{ MeV}/c^2$ is the muon mass, $E_{\mu,\text{binding}}$ the binding energy of the muon in the ground state of the muonic atom, and E_{recoil} is the kinetic energy of the recoiling nucleus. In the aluminium target used for COMET (see section 2.2.3) the electron energy is $E_e = 104.97 \text{ MeV}$.

Typically μ - e conversion experiments discuss the conversion rate, rather than the full branching ratio, which is given by:

$$\mathcal{C.R.} = \frac{\Gamma(\mu\text{-}e \text{ conversion})}{\Gamma(\text{nuclear capture})} \quad (2.2)$$

The key difference between the full branching ratio and the conversion ratio is that by normalising to the number of muons that undergo nuclear capture, as opposed to the total number of stopped muons, the theoretical uncertainty due to the initial muon wave-function is reduced since this is needed to predict the decay rate.

From this, one defines the Single-Event Sensitivity (SES) to be:

$$\text{S.E.S}(\mu^- + N \rightarrow e^- + N) = \frac{1}{N_\mu \mathcal{B}_{\text{capture}} A_{\mu \rightarrow e}} \quad (2.3)$$

where N_μ is the number of muons stopped, $\mathcal{B}_{\text{capture}}$ is the branching ratio for muon nuclear capture, and $A_{\mu \rightarrow e}$ is the total acceptance of electrons coming from μ - e conversion.

The SES then is a statement purely of signal efficiency and does not account for background rates. It is clear, however, that for any observation to be confidently labelled as signal or, in the event of a null-observation, in order to set the tightest possible confidence limit, the background rate must be kept comparably low.

Type	Background	Number of events during run	
		Phase-I [29]	Phase-II [15]
Intrinsic	Muon Decay-in-Orbit	0.01	0.15
	Radiative Muon Capture	0.0019	< 0.001
	μ^- Capture w/ n Emission	< 0.001	< 0.001
	μ^- Capture w/ Charged Part. Emission	< 0.001	< 0.001
Prompt	Radiative Pion Capture	0.00028	0.05
	Beam Electrons		< 0.1*
	Muon Decay in Flight	≤ 0.0038	< 0.0002
	Pion Decay in Flight		< 0.0001
	Neutron Induced	$\sim 10^{-9}$	0.024
Delayed	Delayed Radiative Pion Capture	~ 0	0.002
	Anti-proton Induced	0.0012	0.007
	Other delayed B.G.	~ 0	—
Cosmic	Cosmic Ray Muons	≤ 0.01	0.002
	Electrons from Cosmic Ray Muons		0.002
Total background		< 0.032	< 0.34
Signal (Assuming $B = 1 \times 10^{-16}$)		0.31	3.8

Table 2.1.: Backgrounds for COMET Phase-I [29] and Phase-II [15]. Prompt backgrounds arise by protons that occur in between bunches and are therefore suppressed by the extinction factor. For Phase-I, the recently measured value of 10^{-12} was used for the extinction factor, but for Phase-II the older expectation of 10^{-9} was used. If this is not taken into account, the Phase-I estimates suggest a greater background to signal sensitivity than for Phase-II. *) Result was statistically limited.

Table 2.1 summarizes the results of previous studies for background rates at Phase-I and Phase-II. There are four groups of background source: intrinsic, prompt, delayed and cosmic sources.

Intrinsic processes are those that arise from muons stopping in the target and will always be present regardless of the muon beam purity and detector performance. Of these, the dominant background is muon decay in orbit (DIO), which is the standard model process of a muon decaying to an electron, emitting two neutrinos in the process. Although the decay of a free muon cannot produce electrons with energy greater than half the muon mass, once bound to a nucleus the neutrinos can be configured to carry

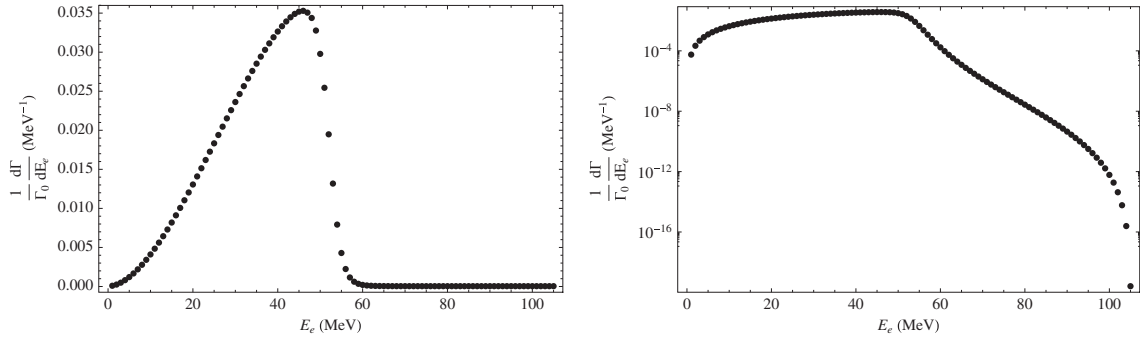


Figure 2.1.: Spectrum of electrons coming from muon decay-in-orbit by Czarnecki et al. [17]. The two spectra are the same, but left is on a linear-linear scale whilst the right plot is on a log-lin scale which shows clearly the high-energy tail reaching up to the μ - e conversion signal energy of 105 MeV.

away almost no kinetic energy, leaving only the nucleus and electron to determine the kinematics of the end-point configuration. From this it can immediately be seen that the maximum energy of the electron produced from muon decay-in-orbit is the same as for μ - e conversion (up to the neutrino mass), and indeed a tail in the spectrum of electrons coming from muon DIO extends all the way up to this point. However, clearly such a configuration occupies a tiny part of the phase space as can be seen from Fig. 2.1 which shows the spectrum of electrons from muon DIO in aluminium. It can be seen that whilst the high energy tail does reach up to about 105 MeV/c, the rate drops away very steeply above the free-muon decay end-point, falling some 18 orders of magnitude from its peak around 50 MeV/c.

Delayed and prompt processes come from impurities in the muon beam, be they pions, antiprotons, or high energy muons and electrons. The key distinction between these two is the timing at which the background is detected with respect to the arrival of the proton beam. For example, pions reaching the stopping target region are dangerous since they can produce high energy gamma rays which can pair produce to create 105 MeV electrons. Since pion capture against a nucleus is extremely fast (less than 1 ns) the timing of pion-induced backgrounds is determined solely by the arrival time of pions into the target region. In order to reach this region without decaying, the pions must be relatively high momentum of about 60 MeV/c or greater. As a result, backgrounds from pion capture are typically expected close to the arrival of protons at the production target. These sort of prompt processes are suppressed by using a pulse proton beam (discussed in more depth later) and ensuring very few protons in between pulses. Other beam related issues include the decay of muons and pions to electrons. An electron

of 100 MeV/c can be produced by muons or pions with greater than 70 or 50 MeV/c respectively, and so the flux of higher energy particles in the beam must also be removed.

Delayed processes are those where the timing of the proton beam cannot be used to improve suppression since the characteristic time between detection of the background and a proton on target for these processes is large compared to the beam pulsing. Possible sources of this delay include the mirroring of particles by the magnetic field, or by some heavy particle from the production target producing pions and high-energy electrons. At a given momentum, antiprotons travel considerably more slowly than muons or pions given their considerably larger mass, washing out any timing information from their production.

Finally cosmic backgrounds arise from high energy muons that pass through the building and enter the detector or beamline. Events where a muon decays to an electron which is then detected as 105 MeV are counted as backgrounds. In particular, muons that produce high energy electrons close to the target are dangerous since cuts on the reconstructed direction and position will be less effective.

All these processes will be discussed and evaluated in more depth in the section on background estimates.

2.2. General Experimental Techniques

Suppressing background rates while maintaining a high signal efficiency leads to several novel techniques being used in the COMET experimental set-up.

2.2.1. Proton Beam Energy and Production Target

The muon beam used in COMET is produced from the decay of a secondary pion beam created by protons striking a target. If maximising the muon intensity were the only concern, then both the proton beam power and atomic mass of the target material would similarly be maximised since the pion production cross section grows with these two parameters. However, the need to suppress background rates and maintain the mechanical and operational stability of the target constrains both of these parameters.

In particular, protons striking an individual, stationary (and, in theory, unbound) nucleon with more than about 6 GeV have sufficient energy to produce antiprotons which

travel relatively slowly (see 2.2.3) and can produce backgrounds. Since the antiproton yield grows very quickly above this threshold, it has been chosen to use protons with 8 GeV kinetic energy.

As well as the beam energy, the intensity is ideally maximised to increase the number of protons on target per second. For Phase-II running, the main ring will operate at $7 \mu\text{A}$ so that a beam power of 56 kW is achieved. Phase-I on the other hand will use a lower beam intensity of $0.4 \mu\text{A}$ or 3.2 kW.

Whilst a heavy metal target is preferable since it increases the number of nucleons that interact with the proton beam and therefore the pion yield, the target must maintain its mechanical strength. This requires the selection of a high melting point material and possibly the use of active cooling. To simplify the situation in Phase-I, a graphite target will be used which can be passively cooled by thermal radiation. In Phase-II however, tungsten has been selected due to its high melting-point of 3422 C, although water cooling will also likely be employed.

Finally, only those pions and muons emitted in the backwards direction with respect to the proton beam are captured and transported to the muon beamline. This is a strong way to reduce the high-energy components of the muon and pion distributions since the yields for low momentum pions in the forward and backwards directions are similar, whilst the high energy tail is greatly suppressed in the backwards direction. At this time however, there is a dearth of experimental measurements for pion production in the backwards direction with 8 GeV protons on a graphite or tungsten target. Fig. 2.2 shows a measurement of the cross section for pion production with 10 GeV protons on tantalum (which is adjacent to tungsten on the periodic table).

2.2.2. Particle Transport through Bent Solenoids

Both Phase-I and II make use of bent solenoids to help select particles of a particular momentum. In bent solenoids, a transverse dispersion occurs that is proportional to the momentum and charge of the particle passing through it.

Charged particles moving through a straight solenoid follow a helical trajectory, orbiting a point that moves parallel to the solenoidal axis with constant velocity fixed by the longitudinal momentum of the particle. The frequency that the particle rotates about this point (the cyclotron frequency or frequency of gyration) is determined by the transverse momentum.

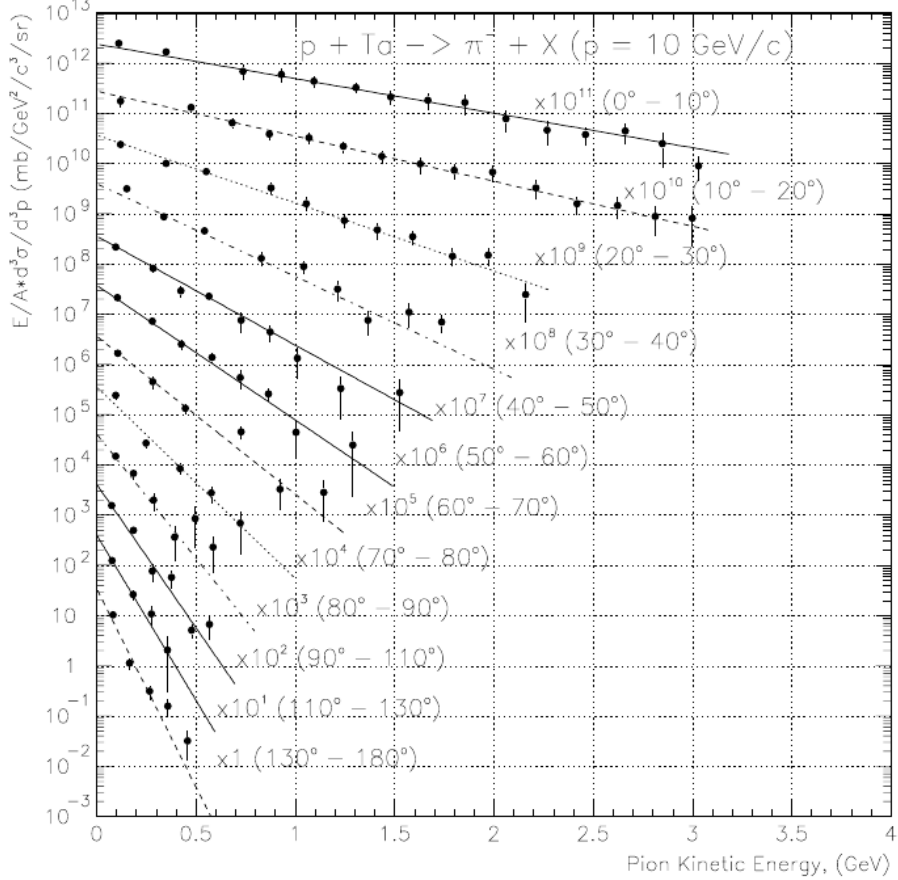


Figure 2.2.: Double differential cross section of pion production on a tantalum target from protons with 10 GeV kinetic energy (reproduced from Meco note 23 [18] which itself used [9]). It is clear that the high-energy component of the spectrum is suppressed as you move to higher production angles which is important for reducing background rates.

By comparison, if a charged particle moves through a solenoid channel that has been bent, the particle can still be considered to orbit a point, only now the motion of that point can be shown to drift vertically, out of the plane of bending. This drift arises from the gradient introduced to the field by bending the solenoid but also from the non-rectilinear coordinate system of the field lines. The total drift, D , of a particle with mass and charge m and q respectively through a solenoid bent with a fixed radius of curvature, R , is given by:

$$D = \frac{1}{qB} \left(\frac{s}{R} \right) \frac{p_L^2 + 0.5p_T^2}{p_L} \quad (2.4)$$

$$= \frac{1}{qB} \left(\frac{s}{R} \right) \frac{p}{2} \left(\cos \theta + \frac{1}{\cos \theta} \right) \quad (2.5)$$

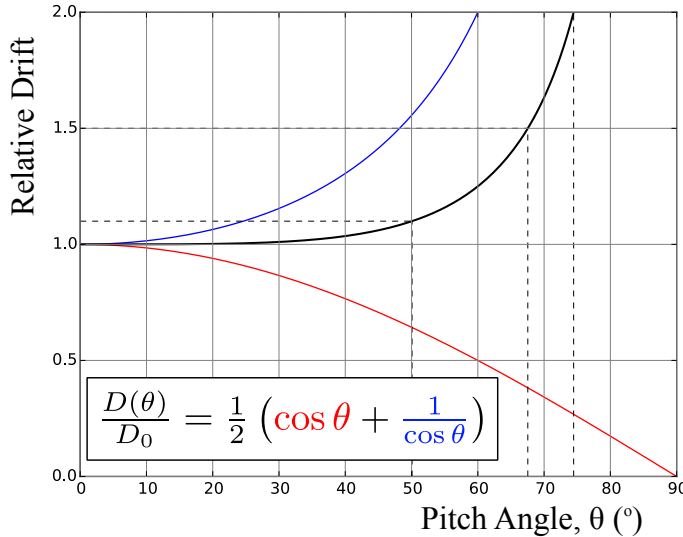


Figure 2.3.: Angular dependence of the magnitude of vertical drift in a bent solenoid field. The total variation (black) remains below 10% for pitch angles below 50° .

where B is the magnetic field strength¹, s is the distance travelled through the solenoid, p the momentum of the particle, with longitudinal and transverse components with respect to the solenoid axis, p_L and p_T respectively (see appendix A for a full derivation of these equations). The pitch angle, θ , is a property of the helical trajectory taken by the particle and defined as:

$$\theta = \tan^{-1} \left(\frac{p_T}{p_L} \right) \quad (2.6)$$

The angular dependence of equation (2.5) is shown in Fig. 2.3 where it can be seen that for angles below 50 degrees the variation in the drift is less than 10%, such that the drift is determined almost completely by the momentum of particles up to these angles.

Bent solenoids are used in COMET to disperse high-energy muons and pions in the muon beam for both Phase-I and II, and as a spectrometer system for electrons coming from the stopping target in Phase-II, which will both be described in more detail below.

Since the drift is proportional to the momentum of the particle, those with zero momentum would remain on axis, whilst higher momentum particles, including those of interest (105 MeV electrons in the Phase-II electron spectrometer and around 40 MeV/c muons in the muon beam line), drift to the sides. However, an additional vertical component is introduced to the magnetic field. If the solenoid were straight the axis of

¹Strictly speaking, B is the field strength along the path of the centre of gyration, which is constant for a fixed transverse distance from the focus of the bent solenoid.

a particle's helical trajectory would follow the field line. A vertical component would therefore cause the trajectories to move upwards with the field line itself, irrespective of the particle's momentum. The same result is true in a bent solenoid and since the drift this introduces is not proportional to momentum a vertical component can be used to select the momentum of particles which remain on axis.

Two techniques have been considered to introduce this vertical component: tilting the solenoid coils themselves, or adding additional dipole coils around the solenoids. COMET has opted to pursue the latter, using a special, proprietary winding technique developed by Toshiba to introduce a vertical component by placing additional conductor around the other solenoid coils. Since the current through these dipole coils can be altered separately to the solenoid coils, this approach has the advantage that the two components can be tuned against the other so that the optimal dipole field can be found whilst running or the on-axis momentum and charge shifted to study backgrounds or other physics searches. Additional collimator material can also be introduced to remove particles with undesirable momentum.

2.2.3. Stopping Target Material and Beam Pulsing

The combination of using backwards going pions and the long, bent-solenoid transport channel is already effective at removing potential background issues. In addition to these however, there is one further method which helps both to reduce beam-related backgrounds and improve the detector occupancy and reconstruction requirements: the use of a pulsed proton beam with a relatively light stopping target.

Since the signal process is coherent, its cross section grows roughly as the square of the number of nucleons (or protons, depending on the model)² until the muon is contained almost completely within the nucleus at which point the rate levels off. It is therefore desirable to use a high-Z target in order to increase the probability of conversion and indeed SINDRUM-II used both lead and gold targets, with its most stringent limit set on gold target [11].

However, as the nucleus gets larger, the lifetime of the muonic atom falls steeply due to the increase in the nuclear capture rate. This is illustrated in Fig. 2.4 where it can be seen that for elements heavier than iron ($Z > 26$) the muon lifetime is less than 200 ns.

²Although this growth is offset by the normalisation to the capture rate which is typically treated as incoherent so that it grows linearly with the number of nucleons. The overall conversion rate itself is roughly proportional to the atomic number for lighter elements.

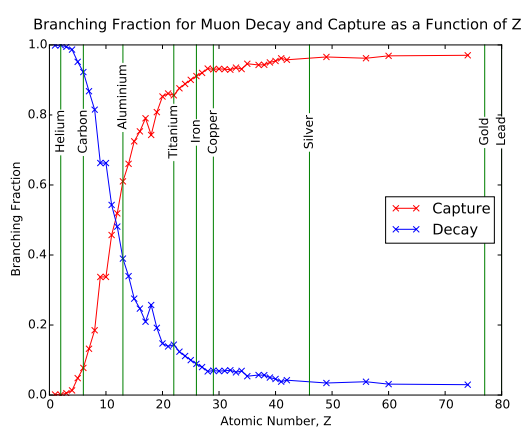
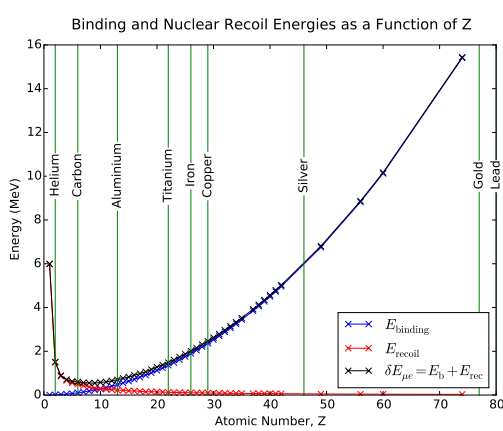
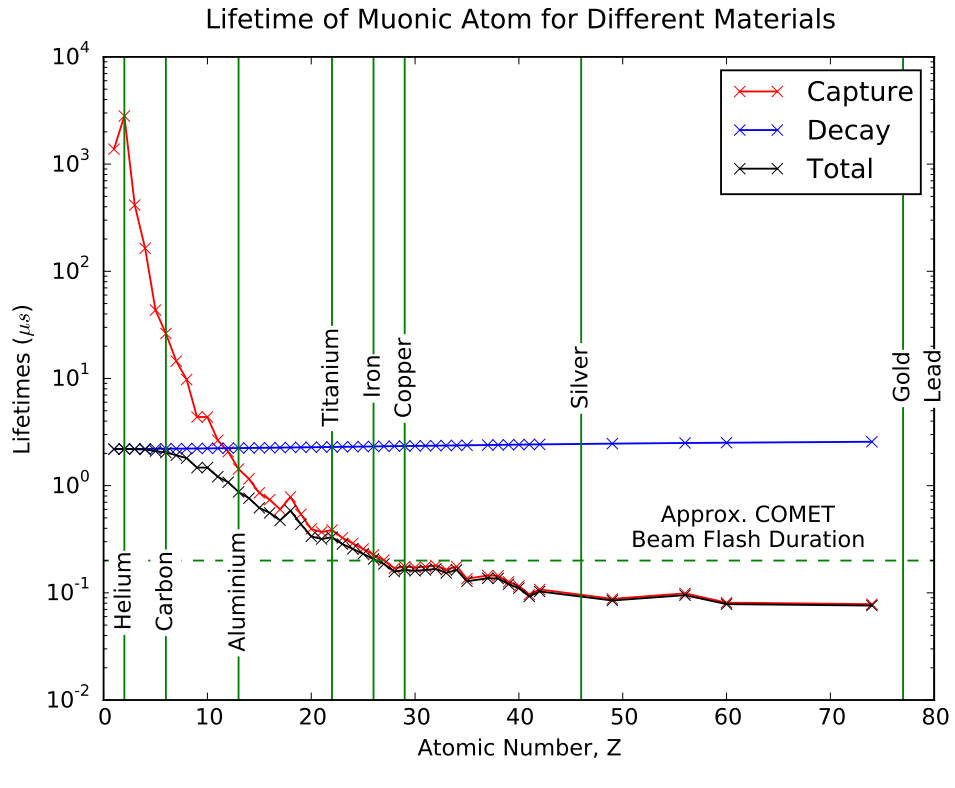


Figure 2.4.: The effect of changing the atomic number on the branching ratio, lifetime and electron energy spectrum end-point. For the branching ratio and lifetime plots, the partial rate for muon nuclear capture and decay-in-orbit are shown separately. The capture and decay rates are taken from the Geant4 [7] parametrisation for stopped negative muons. Only elements for which at least 1 isotope uses a measured value are plotted. The values for the end-point energy level are calculated using the Bohr model for the muon ground-state binding energy.

The COMET production target and beamline produces a beam flash that lasts for about 200 ns after the arrival of a proton. This means that for targets heavier than iron timing information can not be used to distinguish particles coming from the beam from those of muons stopped in the target.

Whilst these are the two dominant factors in deciding the target material, other factors like the mechanical stability, cost, isotopic purity and the stability of the daughter nuclei following muon capture on the target must also be considered. Accordingly, titanium and aluminium are considered the two most viable target materials. Titanium, in which the muon lifetime is about 330 ns, would be considerably harder to measure μ -e conversion so at this stage the COMET experiment is focussed on using aluminium where the muon lifetime is about 864 ns [28].

The J-PARC accelerator has buckets separated by 550 ns, although separations of multiples of this number can in principle be achieved. For COMET running the intention is to fill every other bucket so that a separation of $1.17 \mu\text{s}$ is achieved. Fig. 2.5 shows the beam timing schematically. A window from about 700 to 1100 ns after the proton beam arrival is then used to look for signal events, by which time most of the beam flash should have passed whilst signal events remain probable.

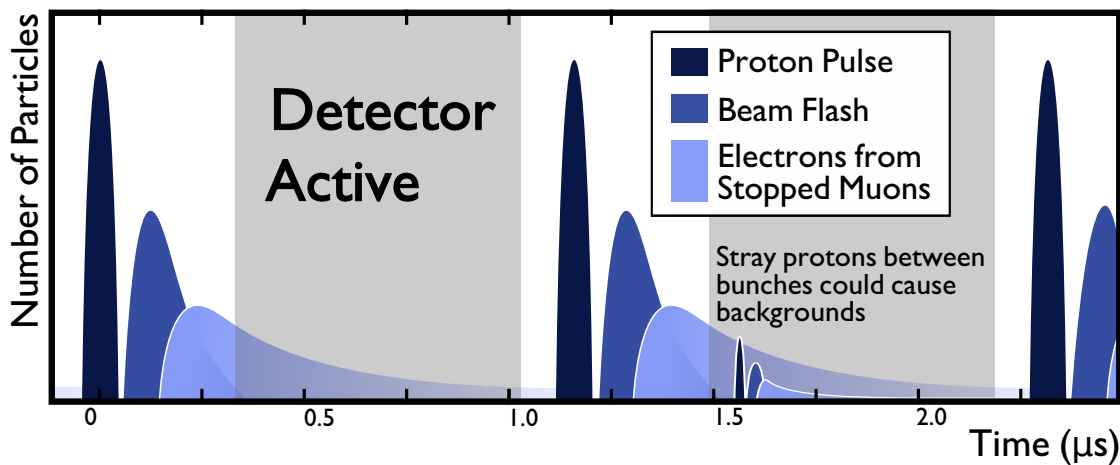


Figure 2.5.: Schematic for the timing structure used in the COMET experiment. Protons arrive at the production target in 100 ns bunches separated by about $1.17 \mu\text{s}$. These pulses create a flash of particles in the detector some 100 ns which lasts for about 300 ns. Muons that stop in that aluminium target last with a life-time of 864 ns, such that signal electrons would reach the detector in this time scale when the detector is able to be triggered. Very few protons should arrive in between bunches, else the corresponding secondaries could be detected as backgrounds.

Having a well-defined bunch structure is crucial for this scheme to work. Protons arriving in between bunches would produce (a fragment of) beam flash that could include high energy muons or pions which could result in background electrons arriving within the timing window. The extinction factor quantifies the rate of late arriving protons and is given by:

$$R_{\text{Extinction}} = \frac{N(p \text{ between bunches})}{N(p \text{ per bunch})} \quad (2.7)$$

Original estimates were made assuming $R_{\text{Extinction}}$ was around 10^{-9} [15] (about 1 out-of-time proton for every 7 Phase-I bunches) although recent measurements have been able to demonstrate extinction at a level of 10^{-12} [?] (about 1 out-of-time proton for every 7100 Phase-I bunches).

The bunch structure is initially defined by the linac at J-PARC which accelerates protons up to 600 MeV. The J-PARC Rapid Cycling Synchrotron ([RCS](#)) then takes these protons up to 3 GeV where up to two buckets can be stored at a time, although for COMET only one bunch at a time will be filled. The protons are then injected into the J-PARC Main Ring ([MR](#)) which accelerates them up the final energy of 8 GeV and is capable of storing up to 9 buckets at once. Using the Linac chopper alone would not be sufficient to produce the desired extinction factor since stray protons tend to drift into the unfilled buckets. Achieving the high extinction factor then is possible only by using the injection kicker from the [RCS](#) to the [MR](#) in a ‘double-kick’ mode. The kicker excitation length is set to two buckets (so that the [RCS](#) is completely emptied into the [MR](#)). The kicker is then activated again immediately after the first filled bunch has performed a complete rotation of the [MR](#) such that protons that had diffused into the second bunch of the [RCS](#) are now kicked away. Thus only every second bucket in the [MR](#) is filled and all other buckets are kept empty.

2.3. COMET Phase-I

Phase-I will see the construction of the COMET hall, the production target capture solenoids, the first 90 degrees of the bent muon transport solenoid, and the detector solenoid. The beamline is shown schematically in Fig. 2.6 where the two interchangeable detector systems can also be seen.

There are two key goals to Phase-I:

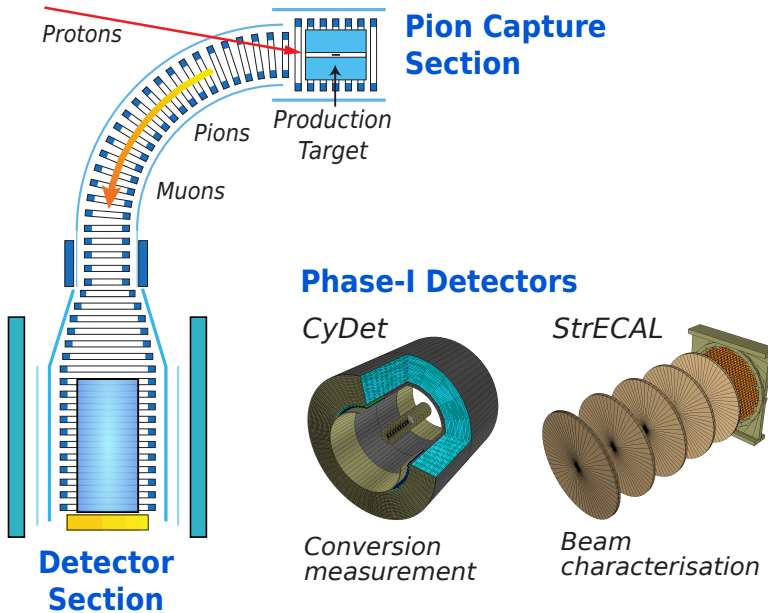


Figure 2.6.: Schematic layout of COMET Phase-I including the two detector systems that will run separately, being swapped in and out of the detector solenoid depending on the study.

1. measure μ -e conversion at a Single-Event Sensitivity (SES) of 3×10^{-15} ,
2. prepare for Phase-II by measuring the beam profile, particle yields and background rates, and prototype the detector technology.

Since the dynamics of bent solenoids are complicated, it is important to study the beam as close to the production target as possible. However, due to the high radiation environment around the production target, the detector and electronics cannot be placed too close and must be well shielded. Phase-I will therefore measure the beam after the first 90 degrees of bent solenoid using the same detector system to be used in Phase-II, namely the Straw tube tracker and Electromagnetic Calorimeter (**StrECAL**) detector – a series of Straw Tracker stations followed by an ECAL all sitting in the beam.

However, since the StrECAL detector will be hit by the full force of the muon beam, it would not be feasible to conduct a μ -e conversion search using this detector. As such, for Phase-I a second detector, known as the Cylindrical Detector (**CyDet**) will be used for this purpose. The **CyDet** uses a Cylindrical Drift Chamber (**CDC**) to reconstruct the trajectories of charged particles and a pair of Cherenkov and Scintillation counters (one upstream and one down) to trigger the read-out of the system. The **CyDet** escapes the

issue of the beam flash that the [StrECAL](#) would face at Phase-I since only the outer region is instrumented. Since the detector sits in a 1 T solenoid field (and both the detector and solenoid are co-axial), particles follow helical trajectories with the radius of gyration determined by the transverse momentum of the particle. The beam is introduced in the centre and typically remains in an envelope of 15 cm whilst the stopping target sits in the centre of the detector with a radius of 10 cm. As such the detector itself is geometrically blind to charged particles in the beam and electrons coming from muon [DIO](#) in the target with momentum less than 60 MeV/c which make up the majority of the [DIO](#) spectrum. To reconstruct the longitudinal position of the particle's trajectory an all-stereo configuration is used in the Cylindrical Drift Chamber, where each layer is rotated in the opposite direction compared to the previous layer by an angle of 4° with respect to the solenoid axis.

Because the Phase-I detector sits much closer to the stopping target than at Phase-II, there is greater exposure to hadrons emitted following nuclear capture of the stopped negative muons, such as protons, deuterons, alpha particles and so on. Despite being emitted with kinetic energies of a few tens of MeV, momenta above 60 MeV are readily achieved given the large mass of these particles. For similar reasons these particles are typically very heavily ionising, so if left unchecked could easily dominate the occupancy of the [CDC](#). The AlCap experiment has shown that for muon capture on Al-27 nuclei, the emission of a proton occurs for about 3% of every muon capture [30]. At this level, it is believed that no specific shielding is required beyond the carbon inner wall of the [CDC](#) needed to contain the gas mixture.

Four layers of scintillation bars will surround the outside of the detector to provide a veto for cosmic ray events. The most dangerous event would be a high energy muon reaching the target and decaying to a 105 MeV electron which is then detected. Dedicated cosmic runs will be performed prior to operation with a beam in order to understand the flux of cosmic muons.

2.4. COMET Phase-II

Since chapter 4 presents an in-depth optimisation of the design of Phase-II, I shall only give a brief introductory overview here, most of which is based on the design as laid out in the 2009 CDR [15].

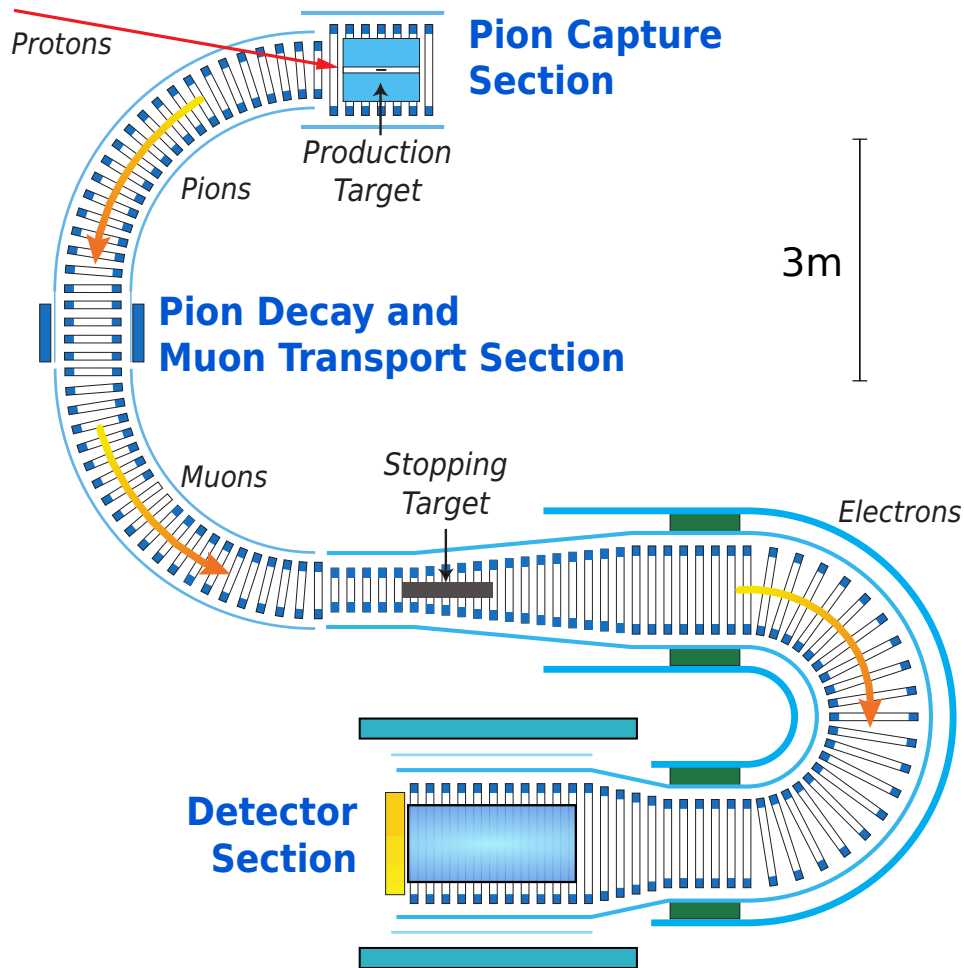


Figure 2.7.: Schematic layout of COMET Phase-II. The 8 GeV proton beam enters from the top-left, producing (amongst other things) pions. Pions and muons travelling backwards with respect to the proton beam are then transported around 180 degrees of bent solenoid, during which time most of the pions decay producing an intense muon beam. About 40% of these muons then stop in the stopping target (centre of image). Any electrons coming from μ - e conversion are then transported through another 180° bent solenoid into the detector system.

COMET Phase-II will be the final stage of the experiment. It will extend the muon beamline built in for Phase-I by an extra 90°, and add two extra solenoid sections: one to hold the stopping target, and a second 180° bent solenoid with a large aperture of 60 cm radius. This layout is shown in Fig. 2.7. The bent solenoid after the stopping target acts both as a spectrometer, but also to remove the low energy DIO electrons which otherwise could significantly increase the hit rate in the detector. The final detector system for Phase-II will use the **StrECAL** from Phase-I but probably with thinner diameter straw

tubes, thinner straw material, and more tracking stations in order to improve the energy resolution.

The stopping target itself has typically been designed as thin disks of aluminium, followed by a beam blocker. Even including the growth of the beam envelope as it passes from the 3 T field in the bent muon transport solenoids to the 1 T of the bent electron spectrometer solenoid the beam blocker removes all line-of-sight between the entrance of the electron spectrometer and the muon transport solenoids so that most of the beam flash is prevented from reaching the detector. The tapering of the field occurs almost completely across the target itself with the intention that signal electrons heading initially upstream will be magnetically mirrored back towards the detector.

As for Phase-I, an active cosmic ray veto will prevent triggering on events caused by cosmic muons. At least the detector solenoid will be covered, but there is some scope

2.5. Schedule and Status

The overall schedule for the COMET experiment is shown in Fig. 2.8. Phase-I is due to start data taking in Japanese Fiscal Year ([JFY](#)) 2018 so that construction and development is well underway.

At the time of writing, with regards to the facility, the building to house the experiment is now finished attached to the side of the existing Hadron Hall at the Japanese Proton

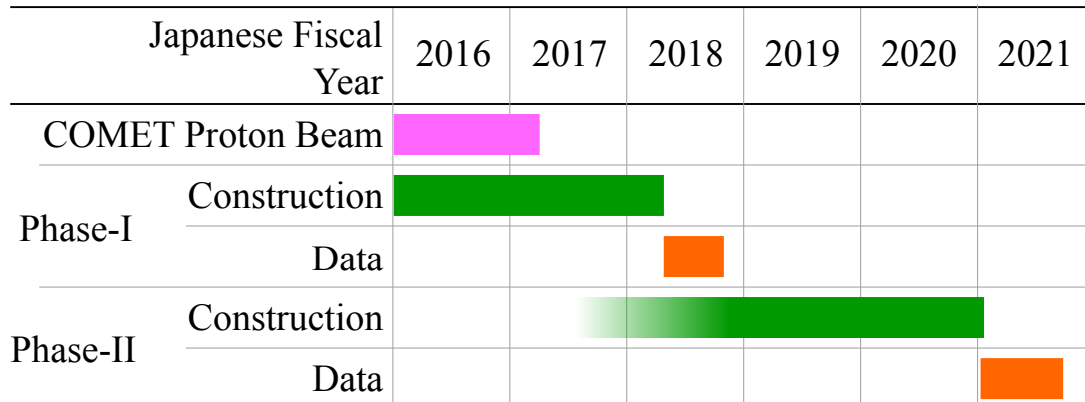


Figure 2.8.: A summarised timeline for the COMET experiment including Phase-I and Phase-II based on the 2016 TDR [29]. At the time of writing, construction of the detector solenoid is underway as well as the final stages of the facility.

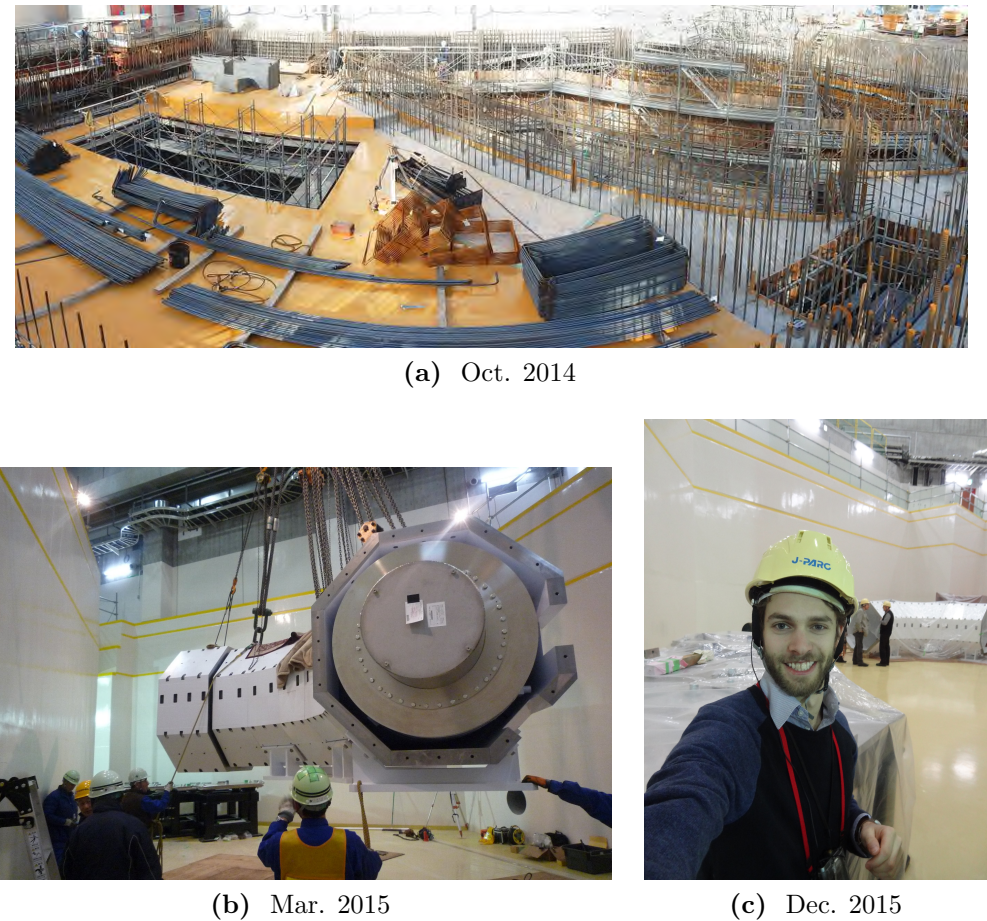


Figure 2.9.: Photographs of the experiment hall being constructed and first sections of beamline being installed.

Accelerator Research Complex ([J-PARC](#)). Cooling and power supplies are being installed and the shielding for the concrete hatch area is being produced. In the mean time the development of the new beamline to extract protons from the [MR](#) and deliver them to the COMET area is being installed. In particular, the Lambertson magnet which directs the protons towards COMET rather than the existing Hadron Hall has been built. For the muon beamline, the Phase-I section of the bent muon transport solenoids has been built and installed and is now under commissioning studies. Construction of the detector solenoid has also begun with the capture solenoids around the production target soon to begin. A selection of photographs that show the construction of the facility and installation of the bent transport solenoid are show in Fig. 2.9.

Much of the recent activity for the collaboration has been on the design and construction of the detector systems. Beam tests to understand the performance and resolution of prototype ECAL crystals, straw tubes and the [CDC](#) have taken place. For the [StrECAL](#),

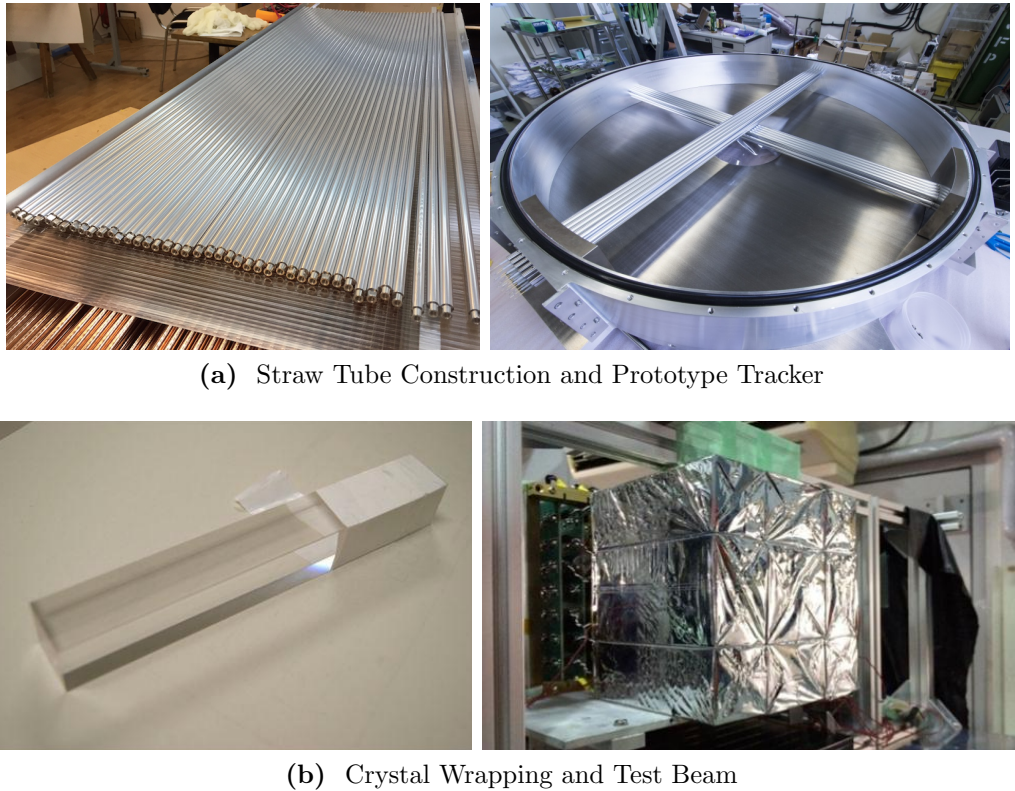


Figure 2.10.: Research and development for the [StrECAL](#) showing both the individual straws or crystal and a prototype set up used at test beams to characterise the sub-detectors.

production of all 2500 Phase-I straws has been completed and procurement of the Cerium-doped Lutetium Yttrium Oxyorthosilicate ([LYSO](#)) crystals for the ECAL is under way with some 200 or so crystals already purchased. Aging tests of the straw tubes are on-going with straws under pressure and tension being held for an extended duration at KEK. Beam-test data is being analysed to understand the position resolution for a given straw and the energy resolution of the ECAL although for the latter better than 5% resolution for 105 MeV electrons has already been shown. Fig. 2.10 shows photographs of the prototypes and beam test set-ups of the Straw Tube Tracker and the ECAL.

In the meantime the full [CDC](#) has been strung, with some 20,000 wires less than 10 microns thick (*((CHECK: is this the correct wire size))*) being inserted. Every wire has had its tension checked using a vibrational resonance method, which showed some .. *((CHECK: How many wires needed to be replaced))* wires were out of design tolerances. These have since been replaced. In June 2016, the inner wall of the CDC was successfully inserted, completing the CDC construction, so that leak tests can begin shortly. Fig. 2.11 shows photographs from the stringing of the [CDC](#). In parallel,

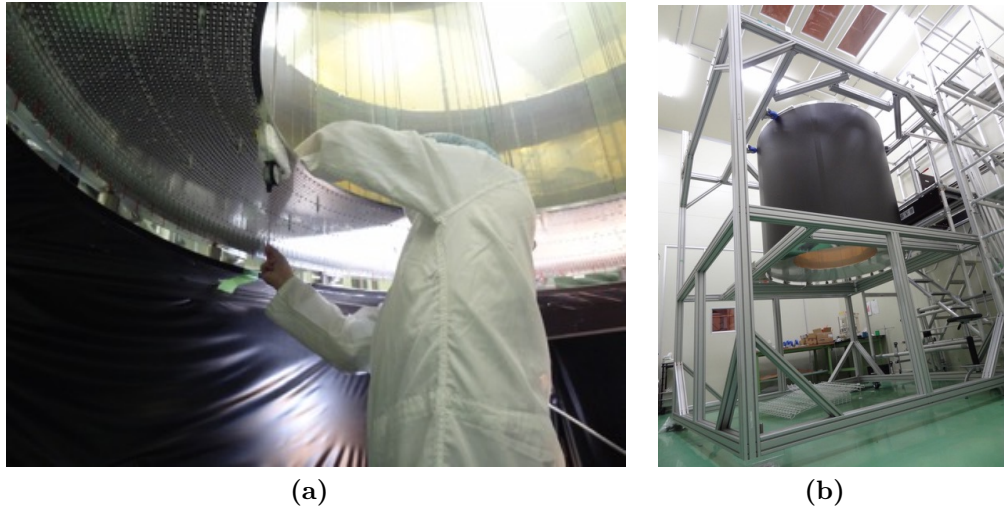


Figure 2.11.: The CDC being assembled and strung.

cosmic ray tests have been used to study to the performance of CDC prototypes and analysis of the data is under way to deduce the X-T curve for the CDC cells.

In the less-tangible realm that is software and simulation, in April last year the offline software reached its first stable release, and has since been used to perform three large-scale Monte Carlo productions of Phase-I. Reconstruction algorithms, including track finding and fitting in the [CDC](#) are under development and techniques to perform Particle Identification ([PID](#)) using the [StrECAL](#) in the Phase-I beam are also under development. More discussion on the software and simulation can be found in the next chapter.

Chapter 3.

Offline Software and The COMET Simulation

In 2013 when I first worked on the COMET experiment, there were many disparate stand-alone simulations being run and no unified approach for data structures and analysis. Since then, a single unified software framework has been prepared and is now being used throughout the collaboration. Developing this framework has been a large part of my work over the last four years , so this chapter presents both a summary of the framework and its development as well as an explanation of the techniques used.

3.1. Developing the COMET Offline Framework

Work to produce a common, standardised software framework for COMET began when funding was awarded for Phase-I. With some four years to go before the switch on, it was clear that the support structure to handle and analyse the data needed to be in place soon. Given the scale of the project and the available resources, the decision was taken to base the COMET offline framework on an existing one, which would reduce the amount of work needed and improve the reliability of the software since it would have been tested elsewhere. A requirements document [?] was drawn up with a list of items that the software should be able to do and a survey of existing experiments undertaken to build a list of candidate frameworks. The list contained:

art A framework being developed primarily at Fermilab [26] which is also being used by Mu2e amongst other experiments.

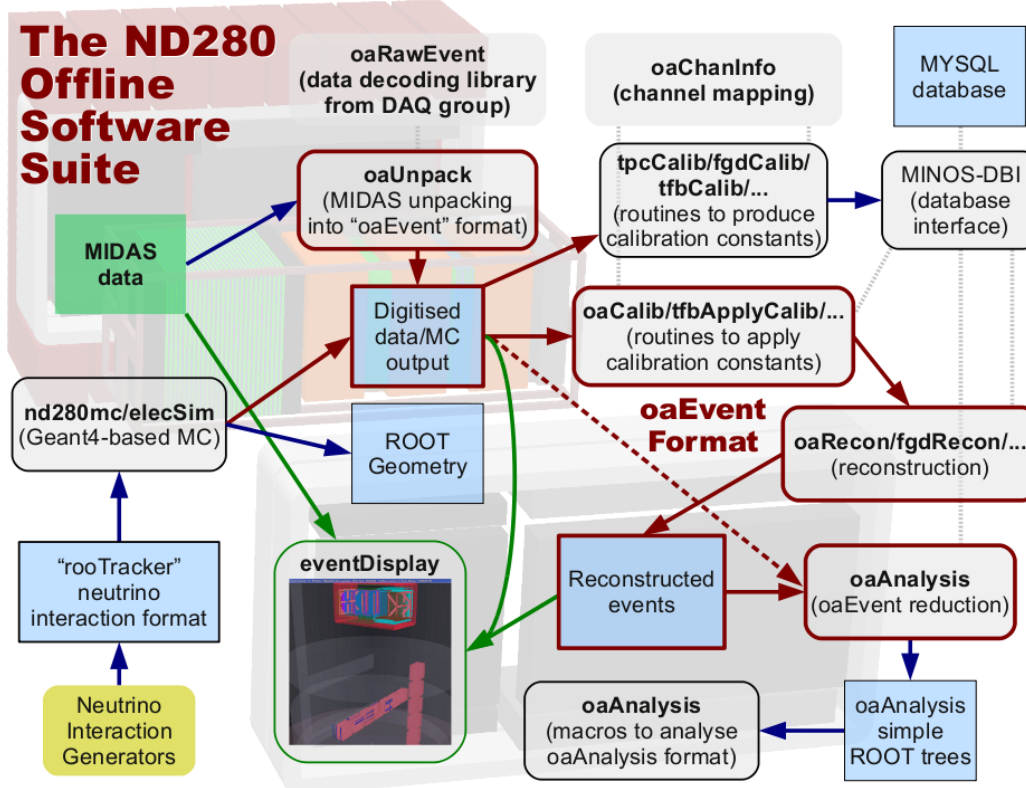


Figure 3.1.: Overview diagram for the ND280 framework.

ND280 The framework [6] used by the near detectors of the T2K experiment, which are also based at J-PARC.

GAUDI which is used by LHCb amongst other experiments [10].

MARLIN The software being developed for the International Linear Collider (ILC) [1].

The final decision was to use the ND280 framework¹ since GAUDI and MARLIN would have required too much effort to adapt to the COMET requirements; since art is used by Mu2e and keeping the software distinct is important for the two experiments to co-exist as cross-checks; and because the ND280 software was already known to a large part of the COMET collaboration and had been tested on real data at J-PARC.

Fig. 3.1 shows an overview of the ND280 framework, including its package structure and the various interactions between packages.

¹The term ‘ND280’ can refer to one of either the ND280 detector itself, the site at J-PARC that houses both the ND280 and INGRID detectors, or the software used to analyse and simulate the T2K near-detectors. For the purposes of this chapter, unless specified explicitly, the term ‘ND280’ should be taken as referring to the software.

With the decision to base the COMET experiment on the ND280 framework – and with the selection of the new name: ‘ICEDUST’ – the process of forking the software was begun. Since the ND280 framework had evolved somewhat organically a review of the conventions and code names was performed. For example, whilst the ND280 software prefixes all classes with a capital ‘T’, the ICEDUST conventions [25] agreed to swap this to a capital ‘I’ to reduce clashes with ROOT which also uses ‘T’. The package renaming scheme [?] was developed so that the purpose of a package and its role with the other packages could be more clearly identified.

Whilst fundamental, low-level packages have been left relatively unchanged higher-level packages which include more detector specific details had to be developed. Additionally some aspects of COMET needed considerably more support than had been present in the ND280 software. Some of the key changes that have been introduced between ICEDUST and ND280 are:

Simulation Although the fundamental data types have not been changed, the simulation has been nearly completely rewritten. In particular, support for hadron production codes have been added to model the production target; both the Geant4-based package (renamed to SimG4) and the detector response simulation (renamed as SimDetectorResponse) were given near-total makeovers; a new package (SimHitMerger) for resampling the G4Hits (simulated charge or energy deposits) was added. Custom physics models have been added to SimG4 to improve the modelling of the COMET-specific physics processes.

Magnetic Field handling whilst the ND280 detector has a fairly straight-forward magnetic field, the COMET experiment has anything but this. Accordingly significant work has been made to replace the way the magnetic field was handled from essentially a few constants to the ability to use complete fieldmap descriptions made with external field calculation software.

Geometry handling The unusual shape of the COMET experiment, the level of detail needed for background estimations in a high-precision experiment, and the changing nature of a staged experiment meant a more elaborate scheme for handling the geometry was necessary than had existed in ND280.

Reconstruction and Calibration packages As simply renaming of the packages, the interdependence of the calibration and reconstruction packages has been improved. Additionally, support for track fitting using Genfit2 [22] has been added as well as new track finding algorithms being developed.

In addition to the above changes to the way the software runs, the distribution of the software has changed from using CMT [2] with CVS version control to being based on git with a GitLab [16] web-based user interface for the official repository. The switch to GitLab also brought a ‘merge-request’ which has allowed development of ICEDUST to progress rapidly with only a small number of developers. Although initially the intention was also to switch the build system from CMT to CMake [3], this decision has since been reversed due to improvements in CMT.

In the 3 years since the initial work forking ND280 to produce ICEDUST in summer 2013 some 3,200 commits have edited about two million lines of code in the official version of the framework. This has been the work of some 25 collaborators whilst about 15 other users have GitLab accounts and use the software. ICEDUST has been used to run three large Monte Carlo productions, most recently simulating about 10^{11} Protons on Target (POT) events – equivalent to 18,000 Phase-I bunches – in some 100 TB of simulated data.

3.2. Overview of ICEDUST

ICEDUST Can Efficiently Do Useful Software Things and stands for the Integrated COMET Experiment Data User Software Toolkit. Fig. 3.2 shows the flow of data through the different packages of the framework and the data formats used.

Inside the framework, nearly all processing is done using a ROOT file-based format known as oaEvent. Files of this type contain header information providing run identification numbers as well as a description of the geometry and magnetic field. The data payload contained in oaEvent files is stored in a ROOT TTree with a single branch containing a single COMET event per entry. Each COMET event has a dynamic structure and can have any object which derives from the IDatum base class added to its list of data on an event-by-event basis.

Data from the detector systems is recorded in MIDAS [5] format which also contains data from the slow control monitors such as temperature sensors and high-voltage power supplies. The task of converting the MIDAS files into the oaEvent format is handled by the package oaUnpack which writes out new, converted files, and oaRawEvent which can convert the MIDAS files to oaEvent format on the fly.

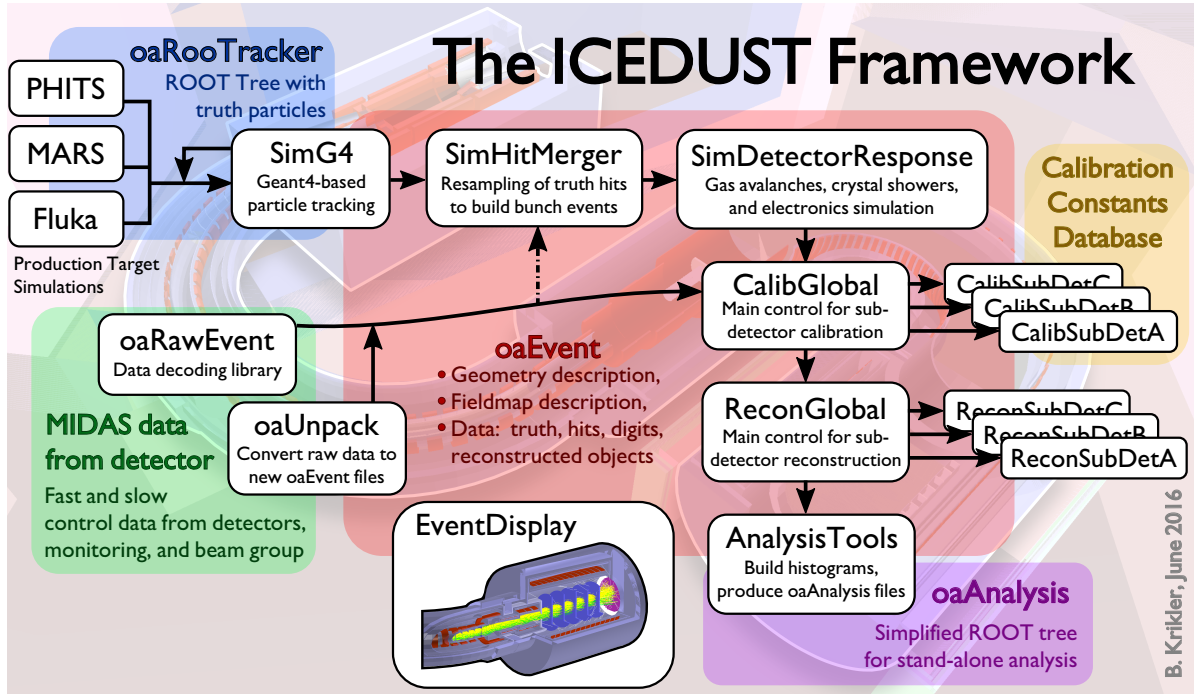


Figure 3.2.: Overview diagram for the ICEDUST framework. Data produced from simulation or taken in the real experiment are treated identically through the calibration and onwards up to analysis.

Simulated data is also produced in the oaEvent format and involves some 4 to 6 packages being called, described in more depth in section 3.3.

Once either simulated data has been produced or real data has been converted, calibration routines can then be applied. Each sub-detector is capable of pulling constants that were previously generated from a MySQL database and applying these to the detected (or simulated) energy deposits. These calibrated hits are then passed into the reconstruction stage. Here again each sub-detector system is first allowed to handle the data until a full reconstructed event is produced. For the tracking detectors this stage typically involves an initial track finding stage, where noise hits are removed and track candidates consisting of a list of hits are collected, and secondly a track fitting stage where the actual path of the underlying particle is reconstructed and key values like momentum and helical pitch-angle deduced.

Nearly all of the processing of data up to this stage has used the oaEvent format. The final analysis stage however moves into a simpler, flatter format, known as oaAnalysis, which produces a data summary tree (as opposed to tape) that can be accessed without a dependence on the full ICEDUST software.

Around all of this there are several utility packages, such as the event display which can visualise any oaEvent file, and IcedustControl which can run a single set of data through the data chain and is the main steering mechanism used for production running.

3.3. The COMET Simulation

The ability for an experiment to set stringent confidence limits in the event of a null-observation is determined both by the expected signal acceptance (which should be high) and the predicted number of background events (which should be low). For COMET’s target single-event sensitivity – which is only a measure of the signal efficiency – to translate to a comparable confidence limit if no signal is observed, fewer than one background events should occur during the run. By comparison, some 10^{19} and 10^{21} protons will impinge the production target in Phase-I and Phase-II respectively so it is clear that the ability to suppress backgrounds must be demonstrably high.

Simulation plays a crucial role in making such a demonstration. Before the experiment is built and operated it allows one to optimise crucial aspects of the geometry and parameters, such as the magnetic field strengths or timing cuts. In addition, using Monte Carlo techniques in an accurate simulation allows an estimation of the background rate by sampling the parameter space corresponding to each stage of the experiment. Clearly then the simulation itself must be as faithful a reproduction of the true experiment as possible.

The COMET simulation therefore needs to be both highly accurate and highly efficient. As well as custom physics modelling, and special handling for the magnetic field, several resampling techniques have been introduced to increase the statistical power. The steps needed to build up the COMET simulation are shown in Fig. 3.3.

To reduce the uncertainties associated with the production target and the muon and pion yield multiple hadron codes can be used, including PHITS [23], MARS [27], Fluka [20] and Geant4 [7]. The SimG4 package, which is based on Geant4, then takes over the muon beam simulation and tracking of particles to the detectors. These energy deposits, referred to as G4Hits, can then be converted to realistic electronic detector-readouts by the SimDetectorResponse package. On most occasions though, the G4Hits are first reshuffled with G4Hits from other Proton-on-target events so that a realistic bunch structure is built up and processed, since it is this structure that the true detector

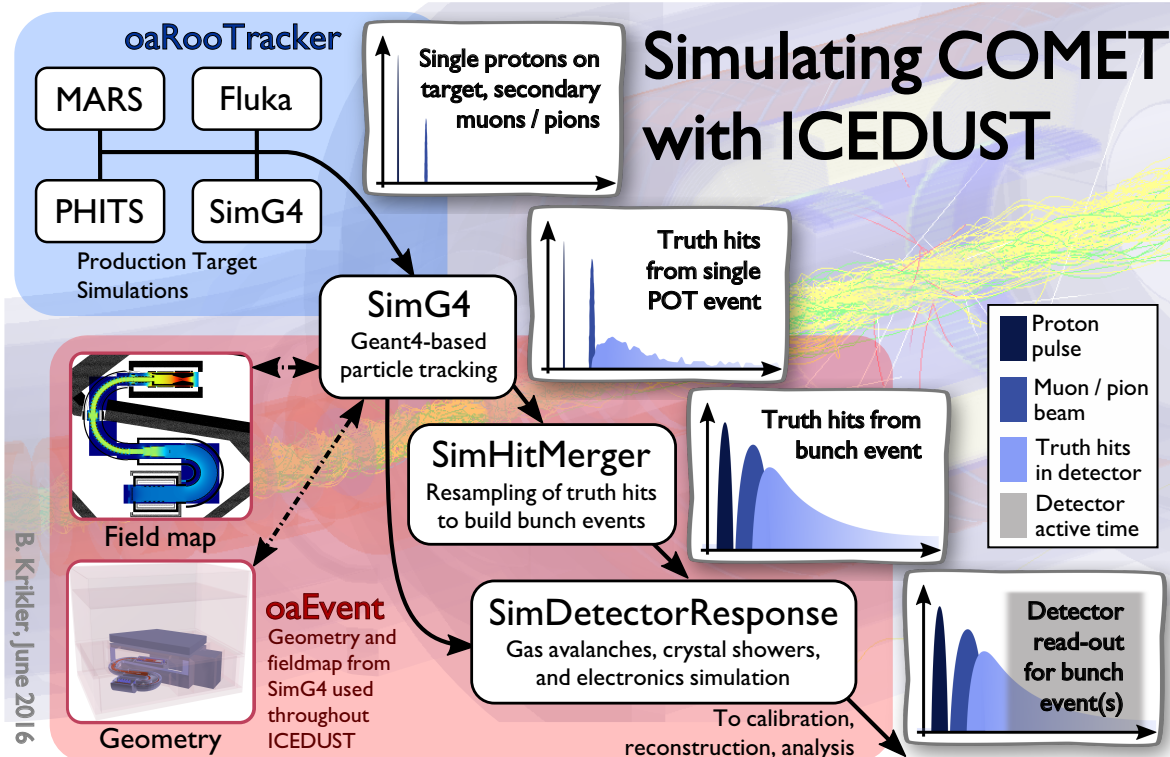


Figure 3.3.: Diagram showing the stages used to simulate COMET. The timing schematics on the right show how a simulated event is built up, firstly by producing many individual proton interactions with the production target, then by transporting the secondary particles to produce energy deposits in the detector, which are then combined with the truth hits from other proton events to produce a realistic bunch structure. Finally these bunch events are processed through the detector response simulation to produce fake waveforms and other detector read-outs.

will see. SimG4 produces one output event for every primary vertex introduced² whereas SimDetectorResponse needs to produce the same sort of data structure as will be seen in the real experiment, which is one event per proton bunch.

This requires some intermediate step, known as SimHitMerger to shuffle the events from SimG4 together and build up realistic bunch events. At this point, a degree of resampling is also introduced, since there are virtually no correlations between proton events. Within a SimG4 output event all timing is given with respect to the original primary vertex. Since protons on target are introduced at $t = 0$, all G4Hits have their timing given with respect to the proton arriving at the production target. In the process of building bunch events, a realistic timing structure for the proton beam is introduced

²This typically means one output event per proton-on-target, but in principle could be something else, such as one output event per signal electron in a dedicated trigger simulation

by shifting the time of all hits for a given proton event by a fixed amount, as if the proton had arrived slightly earlier or later.

A bunch event in Phase-I will consist of about 8×10^6 POT so, without resampling, a simulation of 8×10^8 POT events could only produce 100 bunches. Since the proton events are uncorrelated, by picking different proton events and applying different time shifts to each event, one can in principle build a much larger number of events.

An additional form of resampling can also be used during the Geant4 simulation, by dividing up the experiment into different stages and restarting the simulation multiple times at a later stage, reusing the output from the earlier section. For example, a simulation of the production target region is used to track particles up to the boundary of the muon beam line. The muon beam simulation is then repeated multiple times taking the particles leaving the production target section as an input and changing the initial random seed for each restart. This technique was used in the most recent large scale mass production twice – once at the production target section and again at the entrance to the detector solenoid region – restarting the simulation five times for each section, so that for each initial proton on target, 25 times this number of events were fed tracked through the detector solenoid.

Both of these resampling techniques must be handled with care since this can produce correlations between the events produced from resampled inputs. Reconstruction methods often employ machine learning techniques which are particularly sensitive to correlations within a dataset. To reduce any potential impact due to resampling, the resampled data is handled in distinct sets so that within a set no proton on target event is repeated in more than one output bunch event.

3.3.1. Handling Geometry

During the change from ND280 to ICEDUST, a new geometry handling scheme was introduced to the SimG4 package. This change was motivated by: the fact that COMET has a large number of components with a large variety of complexities, shapes and sizes; the COMET geometry will change dramatically throughout the lifetime of the experiment; all pieces of material closed to the beam could potentially contribute to background rates if, for example, they scatter high energy particles into a high-acceptance region in the phase space.

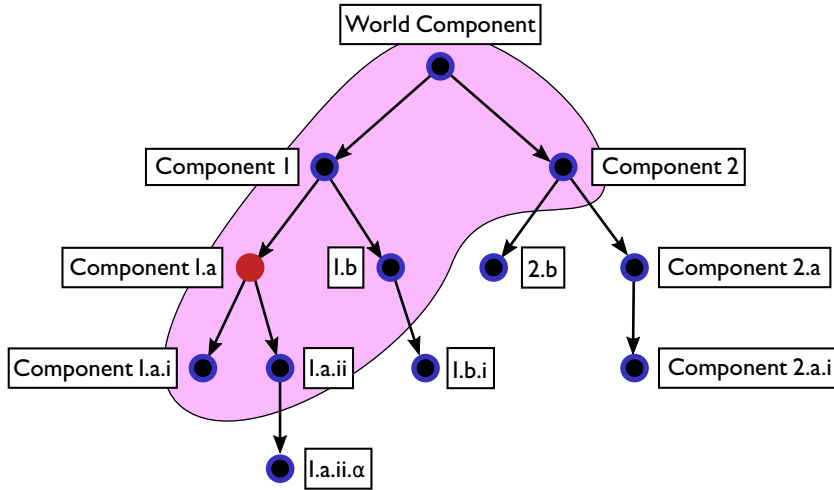


Figure 3.4.: How parameters are shared amongst different components. The Controller of component 1.a in red has access to the parameters managed by Controllers of components contained in the larger violet region.

The aim of the new geometry handling scheme tries to address these issues. The goals in developing the new were approach were to:

- define a clear mechanism for how the geometry is implemented and controlled,
- decouple the code for physically isolated parts of the experiment,
- provide the flexibility to add and remove parts of the experiment,
- maximise the maintainability of the code related to geometry,
- allow for easy inspection of both the geometry and the various parameters that control it.

The final scheme uses a nested component structure which is built up using compiled c++ to define the volumes hierarchy in a modular way with parameters provided at run-time to define the actual shapes and locations of the volumes. The run-time parameters are ‘owned’ by the component they are attributed to and can be assigned values using based on the values of other parameters and inspected easily by various print commands. Access to values of other parameters is given provided they are owned by an accessible component. Whether or not another component is accessible depends on its relative position of in the component hierarchy: the target component must either be an ancestor, immediate child, or share the same parent component, as demonstrated in Fig. 3.4.

To provide the value of a parameter, standard, human readable infix notation allows integers, doubles, three-vectors and rotation matrices to be combined and manipulated. In addition parameters can be easily repeated or indexed, such as for the positions of

```

/comet/Torus2/TS4_First/Dimension InnerR = 23*cm
/comet/Torus2/TS4_First/Dimension OuterR = [InnerR]+22*mm
/comet/Torus2/TS4_First/Dimension Length = 10*cm
/comet/Torus2/TS4_First/Material Material = Copper

/comet/Torus2/TS4_Middle/Dimension InnerR = 23*cm
/comet/Torus2/TS4_Middle/Dimension OuterR = [InnerR]+43*mm
/comet/Torus2/TS4_Middle/Dimension Length = 10*cm
/comet/Torus2/TS4_Middle/Material Material = Copper

/comet/Torus2/TS4_Last/Dimension InnerR = 23*cm
/comet/Torus2/TS4_Last/Dimension OuterR = [InnerR]+43*mm
/comet/Torus2/TS4_Last/Dimension Length = 10*cm
/comet/Torus2/TS4_Last/Material Material = Copper

/comet/Torus2/Count Coils:Count = 16
/comet/Torus2/Angle Coils:PositionPhiStart = 0*degree
/comet/Torus2/Angle Coils:PositionDeltaPhi \
    = ([PhiTotal]-2*[Coils:PositionPhiStart])/([Coils:Count]-1)
/comet/Torus2/Position (i<[Coils:Count]) Coils:Position \
    = ( r=[LargeRadius], theta=90*degree, \
        phi=[Coils:PositionPhiStart]+[i]*[Coils:PositionDeltaPhi])
/comet/Torus2/Rotation (i<[Coils:Count]) Coils:Rotation \
    = (axis=(1,0,0),angle=90*degree) \
    *( axis=(0,1,0), \
        angle=[Coils:PositionPhiStart]+[i]*[Coils:PositionDeltaPhi])

```

Figure 3.5.: An example set of parameter definitions which control the geometry for the Torus2. Parameter specifications use natural arithmetic notation and can references other parameters, use standard units. They can also be formed as sets where each element has a different value, such as the Coils:Position parameter.

crystals in the ECAL or straws in a straw tracker plane, where the i -th position depends on the value of i . A small demonstration of some valid parameter assignments is shown in Fig. 3.5.

Using this scheme, multiple geometries for different stages of COMET have been developed and can be easily swapped between. Each one is able to re-use much of the code for another, such as the experiment hall building which appears in every geometry. In addition it has been straight forward to build up significant complexity in key areas such as the production target. Fig. 3.6 shows some images of the geometry that has been created using this scheme.

A more thorough description of the geometry scheme in SimG4 as well as a users guide can be found at www.hep.ph.ic.ac.uk/~bek07/comet/SimG4/documentation/index.shtml.

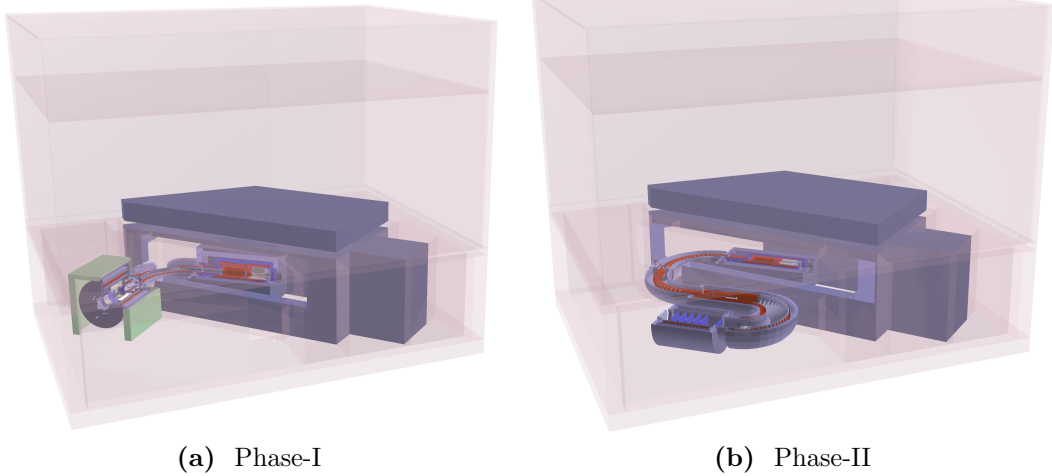


Figure 3.6.: Two of the possible simulation ‘worlds’ that can be selected at run-time: (a) Phase-I with the CyDet detector installed, and (b) Phase-II. Multiple Phase-I worlds exist, one for each potential running configuration.

Once SimG4 has created the geometry, it writes it out to a ROOT-based format alongside the data, using ROOT's TGeo classes [13]. This is then used by the other packages, such as calibration and analysis. The event display also uses this to show the various hits and tracks overlaid on the geometry.

3.3.2. Field Calculation

An essential aspect of the COMET experiment is the static magnetic field that is used along the beam line to capture, focus and disperse charged particles. Modelling this field accurately is important to ensure any outcomes of the simulation are reliable. In particular, dips in the field have a risk of mirroring particles backwards or even trapping particles for extended periods. This could be especially dangerous for COMET since in the process the timing information of the particle is lost which would reduce the efficiency of the timing cut to suppress backgrounds.

Magnetic field calculations can become quite computationally expensive. As a result approximations and assumptions are often made to simplify the process, such as the assumption of symmetry about an axis or plane to reduce the effective number of dimensions to the problem. As well as modelling the electric current flow, material effects must also be accounted for particularly in the yoke and surrounding material of the beamline. Often these material effects are linear, but in regions of high magnetic

field this linearity can be lost via processes such as saturation, further increasing the computational complexity.

There are two distinct types of magnetic field used in COMET, a solenoidal field produced by a winding of super-conducting cable in a spiral, and that of the dipole fields which are produced by a novel winding technique which is proprietary to Toshiba. Although there are several areas of 'bent' solenoid, these are actually formed by a series of smaller straight solenoid sections, and so do not need special treatment in the field calculation. Straight solenoids are used in many other applications so existing coil calculation methods are reliable. Calculating the dipole field however is not so straight forward since the exact configuration is owned by Toshiba.

The COMET collaboration have used several different methods to perform field map calculations. G4Beamline [21] is a simulation toolkit that makes numerous extensions to Geant4 and is able to perform simple solenoid calculations directly. Whilst it cannot model material effects its speed and simplicity allows quick and simple studies. The methods for solenoid calculations of this open-source project have been incorporated into SimG4, so that the package can directly produce the field for solenoid coils contained in its geometry. The resultant fieldmap is shown in Fig. 3.7b.

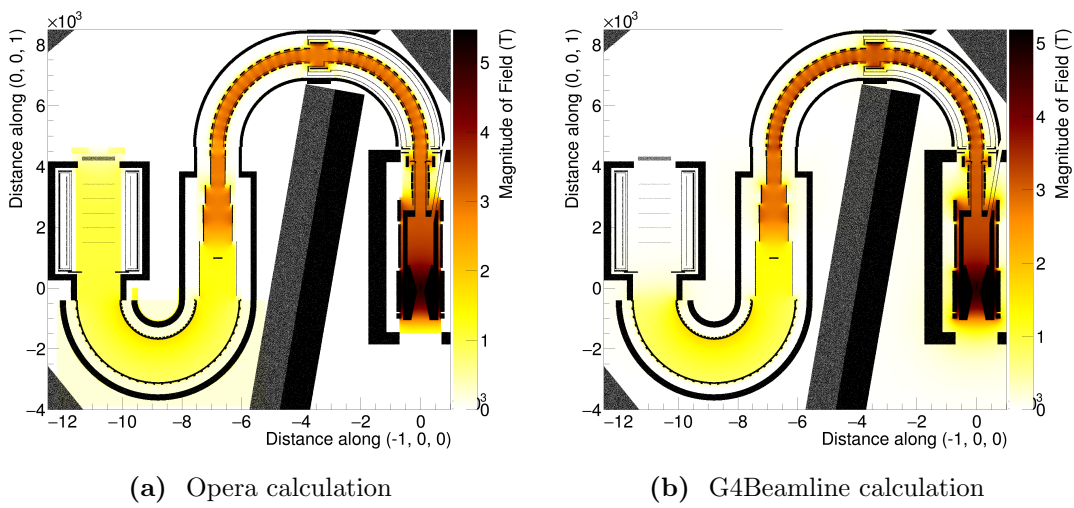


Figure 3.7.: Fieldmap produced by (a) Opera and (b) G4Beamline. Although the fringe field is larger with the G4Beamline calculation, the lack of material effects make this calculation less reliable. Note that the G4Beamline calculation does not include the detector solenoid.

For more elaborate calculations, Opera 3D finite-element-analysis software was used with the TOSCA submodule [?] for static electromagnetic fields. This calculation includes non-linear material effects in the yoke and shielding so that the final fieldmap should be much more accurate. Fig. 3.7a shows the fieldmap calculated by Opera in the plane of the beam line axis. The ratio between the G4Beamline and Opera calculations is given in Fig. 3.8 where it can be seen how the two models disagree most at the exit of the solenoids.

Whilst the above two methods have been used for the solenoid fields, calculating the dipole field structure is a different story, given that the winding is proprietary information belonging to Toshiba. For the dipoles in the muon beamline, Toshiba have provided a calculation for one octant of one winding, which is then mirrored and placed multiple

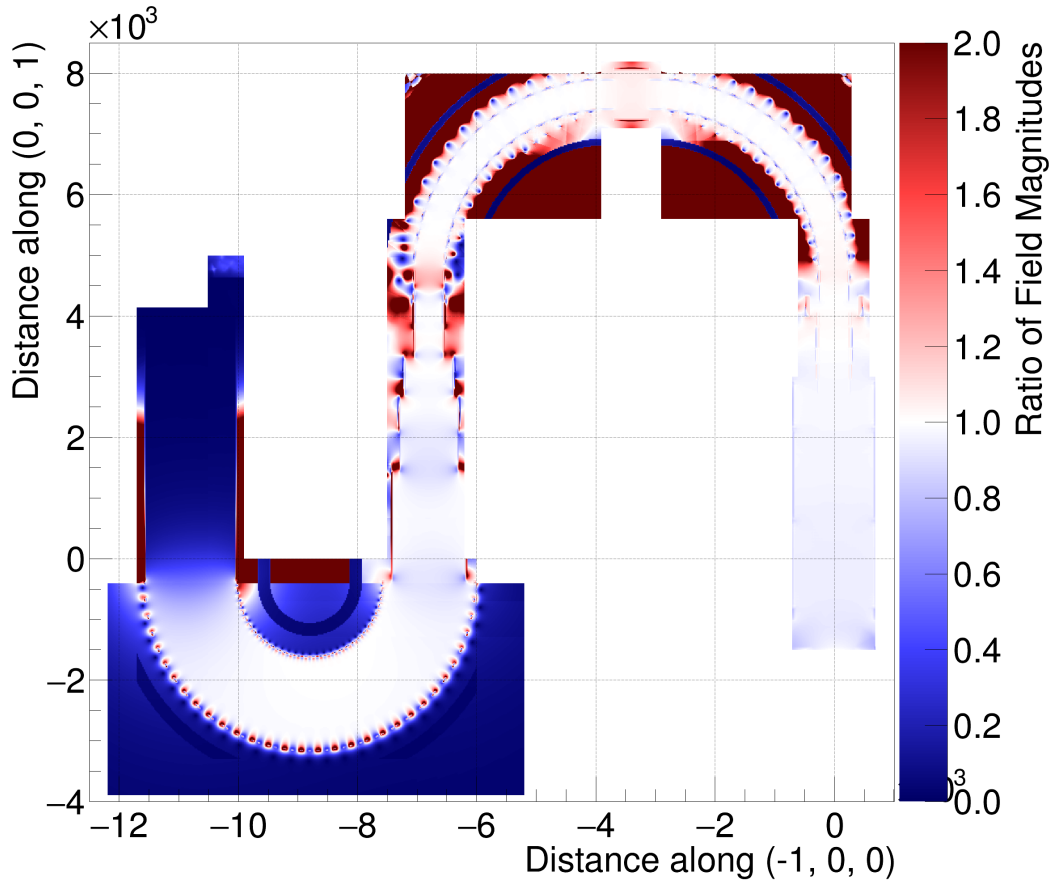


Figure 3.8.: The ratio of the Opera and G4Beamline calculations shown in Fig. 3.7. On-axis the fields are fairly similar although towards the ends of the solenoids the agreement is poorer.

times along the beamline. For the dipoles along the electron spectrometer of Phase-II, there is no accurate calculation at this time.

Whilst only magnetic fields have been used in the simulation up to now, ICEDUST is able to handle electric fields in exactly the same way. For instance future work might see the electric fields for the straw tracker and CDC included to account for the impact of these fields might have on particle scattering in the detector.

Field map files are treated as a single data file which are loaded in and placed with a given rotation and translation as well as an overall field scale factor. It is important that subsequent processing of data files are able to reproduce the same field as used to generate the data. Since many individual field map files are often loaded in to assemble an overall representation of the field to facilitate such book-keeping, a description of each of the used field map files is stored alongside the data similar to the way the geometry is handled. This information contains the name and a check-sum for the original field map as well as the rotation, translation and scale factor. All ICEDUST programs are therefore able to re-instantiate the field given a data file and the location of a directory containing the fieldmaps. Other field components such as solenoid fields produced with the incorporated G4Beamline code are also persisted in this manner.

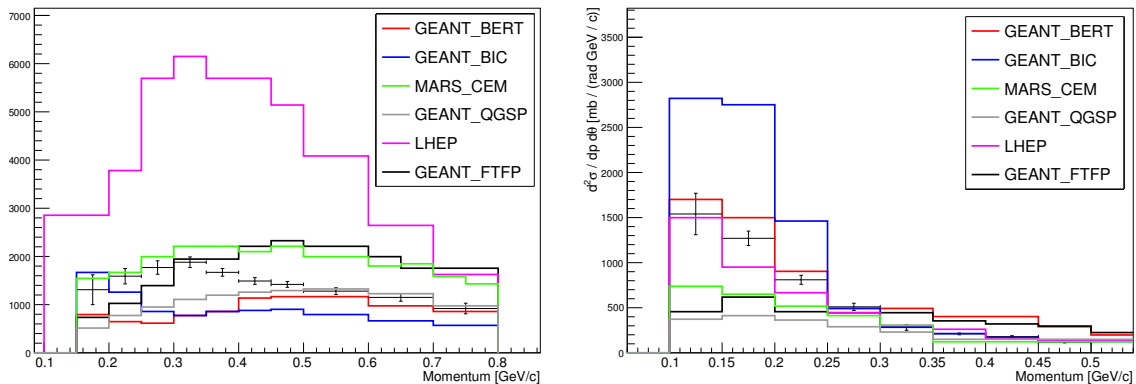


Figure 3.9.: Comparison of various hadron production codes with experimental data from the HARP experiment from the thesis of A. Edmonds [19]. Points with error bars are the experimental data. Left: double differential-production cross section for pion production from 20 to 32° with respect to the incoming proton direction, right: from 100 to 112°. The hadron production code that best reproduces the data depends strongly on which angular region one looks at.

3.3.3. Production Target Simulations

There is currently a lack of experimental data for interactions of protons with 8 GeV kinetic energy with a tungsten target, especially for production of negative pions in the backwards direction. Fig. 2.2 seems to be the best source of experimental data, but even this is problematic in that it represents 10.1 GeV protons striking a tantalum target and that the actual data points are not tabulated anywhere in the literature.

The HARP experiment [14] has also measured pion yields in the context of future neutrino beam facilities, and have used an 8 GeV proton beam with a tungsten target, but only observed pion yields at angles of less than around 2 radians (*((CHECK: What angles did HARP measure up to?))*).

As a result of this shortage of measured values, it is important to use as many hadron models as possible to pin down the uncertainty on the predicted pion and muon yield. Previous studies have compared the HARP data to predictions from several hadron codes [?, 19] some of which are reproduced in Fig. 3.9. From these it is clear that no one model can reproduce the experimental data accurately for all angular regions and all materials.

Currently PHITS [23], MARS [27], Fluka [20], and Geant4 [7] can all be used to run production target simulations and feed results into the rest of the experiment. The level of integration of these packages varies however. SimG4 (which is based on Geant4) and SimMARS (which interfaces MARS into ICEDUST) are able to read directly the standard ICEDUST geometry and fieldmap formats and they are able to output directly to a format known as oaRooTracker which the SimG4 package is able to read back in. Both Fluka and PHITS on the other hand (interfaced via SimFluka and SimPHITS, respectively) are written in Fortran and have proved harder to integrate. At this point in time, each must separately produce the geometry and fieldmap and have their outputs post-converted to the oaRooTracker format. Fluka also lacks a primitive Torus volume implementation, so that other studies such as neutron rates are further limited in Fluka at this stage.

3.3.4. Extending the Geant4 Physics Modelling

Geant4 physics modelling

Aside from the production target region, most of the tracking of particles and creation of secondaries takes place in the SimG4 package, which is built against the Geant4 library. The trajectory of a particle is built up in steps each of which terminates either by a physics process (which might change the particle's direction or energy and produce a secondary track) or by the boundary of a volume in the simulated geometry. To decide what actually limits the step taken by a given particle (for example a positron), Geant4 calls the list of possible processes this particle can undergo (for example Bremsstrahlung, annihilation, inverse Compton scattering, etc) and asks each process for a proposed step length. In the case of a geometry limit, the step length is the distance until the boundary of the geometry, including bending in the trajectory due to any electromagnetic field. On the other hand, for a physics process the proposed step length is typically selected randomly using a relevant probability distribution for this process. Often this involves a characteristic length or time of the process, for example the half-life of a particle that will decay. Out of all possible step limits the process proposing the shortest limit (or if the particle is at rest, the soonest limit) is chosen. The current position and momentum of the particle is updated accordingly and any secondary particles produced are prepared for tracking.

Determining which processes are applied to which particles and how each process is modelled is an important part of building a Geant4 simulation; the library provides a list of standard physics lists to help the process. Choosing the right physics list depends on the goal of the simulation, for example which particles are involved, what energy ranges are interesting, which background effects must be included. To simulate COMET the QGSP_BERT_HP physics list [?] was chosen as a starting point. This model is expected to perform well for low energy dosimetry, shielding and neutron calculations [4].

On top of this physics list, custom changes have been made to the way negative muons are treated once stopped in material. COMET is unusual in the field of modern particle physics for dealing with muons at very low energy, unlike at the Organisation europeenne pour la recherche nuclaire ([CERN](#)) experiments for example, where they are normally treated as minimally-ionising particles (MIPs). As a result, low-energy negative muons are somewhat crudely modelled by the default physics processes of Geant4. In

addition to this, for the COMET experiment it is important to add the process of coherent μ - e conversion, which as a currently unobserved process is not included in Geant4.

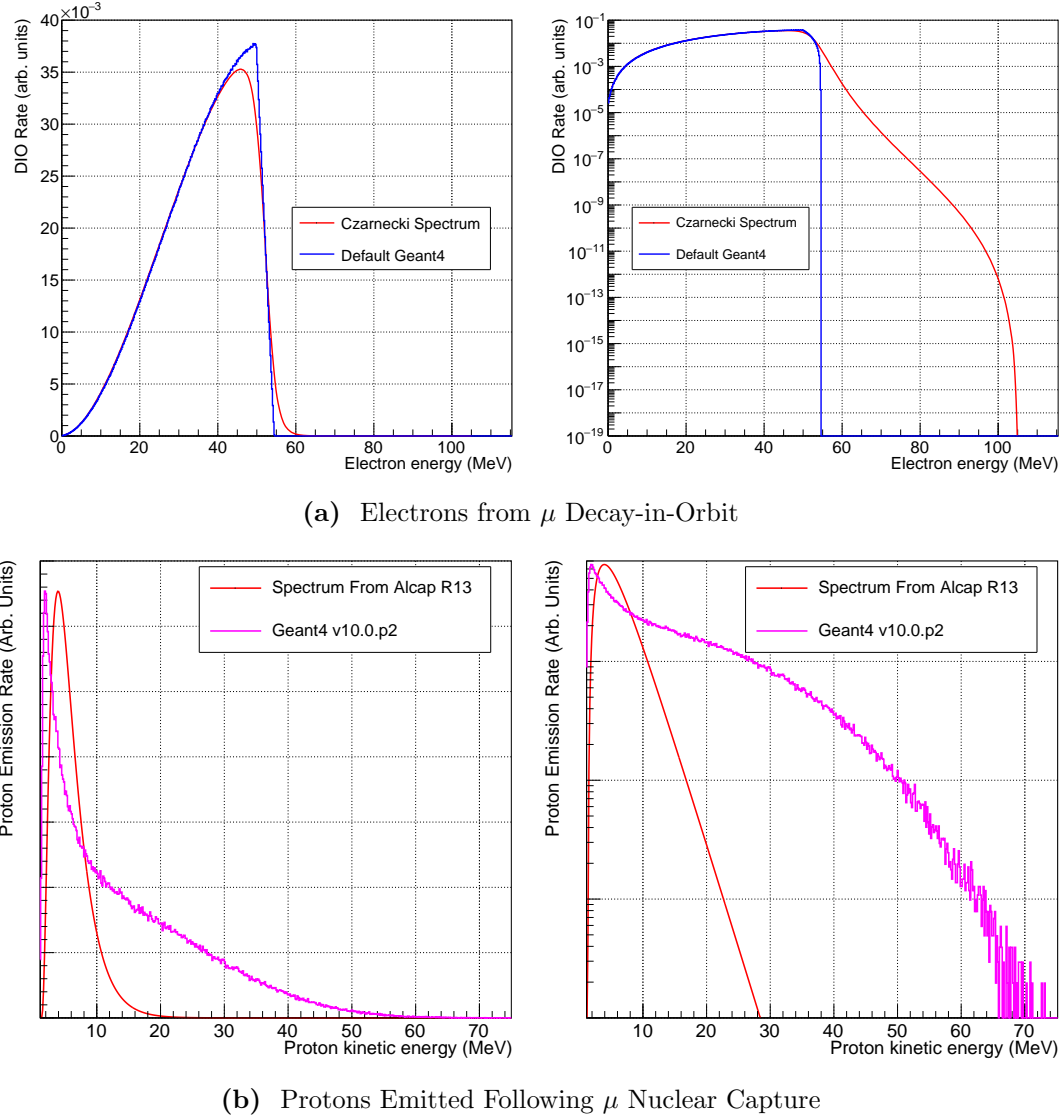


Figure 3.10.: Comparison of the realistic spectra for DIO electrons, (a) (normalised to agree at 35 MeV), and protons coming from muon nuclear capture, (b) (normalised to have the same maximum value), each on a linear scale (left) and a logarithmic scale (right). The DIO spectrum used in default Geant4 has a sharp cut-off slightly above the free muon decay end-point, to be compared with the long but steeply falling tail of the Czarnecki et al. theoretical calculation [17]. The comparison of protons coming from muon capture between the preliminary result from AlCap and default Geant4 shows that the true proton spectrum is much softer than the Geant4 model.

In the Standard Model ([SM](#)), a stopped negative muon that has been captured to an atomic orbital can either undergo decay or nuclear capture. As previously discussed, the end-point for electrons coming muon [DIO](#) reaches up to the μ - e conversion limit, or around 105 MeV/c. Vanilla Geant4 however is unable to produce this tail, and on aluminium is only able to produce electrons up to around 60 MeV/c. This is because the bound muon decay model in Geant4 uses the free muon decay spectrum and applies a boost in a random direction with a boost factor set by the muon binding energy. A comparison of the electron spectrum from this model and that proposed by Czarnecki et al. [17] is shown in Fig. 3.10a where it can be seen how the high energy tail falls far more rapidly in the Geant4 spectrum.

Similarly, for the nuclear capture of the muon, there are sizeable disagreements between the available but limited data and the default Geant4 model. For example, the AlCap experiment [8] has improved the knowledge of proton emission following muon nuclear capture in aluminium. This showed that proton emission occurs for around 3 % of all nuclear captured muons; Geant4 produces around 7 to 8 times more than this. The overall shape of the proton spectrum looks wrong as well. Although the AlCap result is still only preliminary, the spectrum observed there is much softer than produced by standard Geant4 as shown in Fig. 3.10b.

Standard Geant4 models nuclear capture of negative muons using a Bertini cascade which was developed using incident hadrons [31]. Muon nuclear capture is thought to occur via a combination of direct capture on a proton, producing a neutron, or via an interaction with a set of clustered nucleons. The latter is typically invoked to explain proton emission. The Bertini cascade model handles negative muon capture by first handling the prompt process of muon capture on the nucleons then cascading the resultant nucleons through the nucleus. A point within the nucleus is chosen homogeneously and either a proton or nucleon pair interacted with the muon. It is not clear what causes the discrepancy between this model and the experimentally observed result for proton emissions.

Extending the physics processes

To resolve the issues mentioned custom physics classes have been added to the COMET simulation. The key design goal of these classes was to allow future improvements in the experimental and theoretical inputs to be added yet decouple the implementation

from the normal Geant4 implementation so that future updates to Geant4 could easily be absorbed.

Fig. 3.11 shows the class interaction diagram for the extended physics modelling for stopped negative muons. The standard Geant4 model sets up these processes using the ‘G4MuonMinusCapture’ class, which passes concrete implementations for decay and nuclear capture into its base class ‘G4HadronStoppingProcess’. This base-class contains three instances of a ‘G4HadronicInteraction’: one to perform the electromagnetic cascade between the atomic orbitals, another to perform bound decay, and a third to perform the nuclear capture. The ‘G4HadronStoppingProcess’ class is also used to simulate stopped negative pions, kaons, and so on, and bound decay is only considered if a valid instance of such a process has been provided. When a stopped particle is processed through this class, the electromagnetic cascade is always run first which produces X-rays and Auger electrons. Then one of either bound decay or nuclear capture is chosen by asking the bound decay process whether or not it will kill the particle; if so bound decay is considered to have taken place and the nuclear capture is not run. Default Geant4 uses nuclear capture rates based on a 1987 paper by Suzuki et al. [28] which fill in experimental blanks by a semi-empirical models, and decay rates based on a largely theoretical 1980 model by Mukhopadhy [?]. Fig. 2.4 was produced by extracting these parameters.

To extend the default Geant4 modelling and improve the accuracy with the improved theoretical understanding of the DIO process and measurements of muon nuclear capture, three new classes have been written which mirror the way the default Geant4 model is implemented but add more detail. These new classes are shown in Fig. 3.11 in red. Currently they only play a role if the muon stops in aluminium otherwise they invoke directly the default Geant4 model. ‘COMETMuonMinusBoundDecayOrConversion’ takes over the task of bound decay by, if in aluminium, first deciding whether to capture, decay, or convert based on rates which can be adjusted at run-time by Geant4 commands but default to the normal Geant4 rates of capture and decay and a conversion rate of 10^{-15} (which is multiplied by the capture rate to get the total conversion branching ratio). If the conversion process is chosen an electron with total energy of 104.97 MeV is produced in a random direction. If decay is chosen a DIO spectrum is used to randomly generate an energy, which at the time of writing defaults to the 2011 Czarnecki spectrum [17] although other spectra can be specified at run-time. If neither of these processes are selected then the ‘COMETMuonMinusBoundDecayOrConversion’ class returns, leaving the muon status as alive such that the capture process takes place.

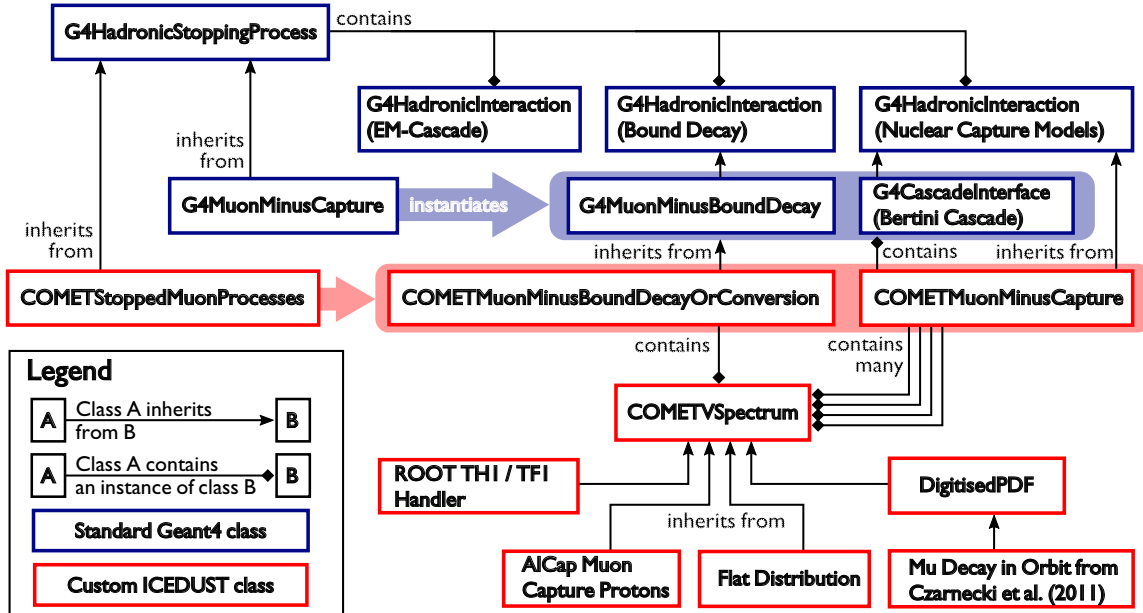


Figure 3.11.: The various classes involved in simulating the various processes of stopped negative muons. The standard Geant4 model is activated by registering ‘G4MuonMinusCapture’ which instantiates ‘G4MuonMinusBoundDecay’ and ‘G4CascadeInterface’ to run the DIO and nuclear capture respectively. To use the custom COMET muon physics, an instance of ‘COMETStoppedMuonProcess’ should be registered which sets up ‘COMETMuonMinusBoundDecayOrConversion’ to produce the electron (and possibly neutrinos) from DIO or conversion, and ‘COMETMuonMinusCapture’ to do the nuclear capture.

Control passes therefore over to the ‘COMETMuonMinusCapture’ class, which contains an instance of the default Geant4 Bertini Cascade model to use for materials other than aluminium, although even this can be re-enabled at run-time. The ‘COMETMuonMinusCapture’ contains a list of types of secondary particle which it is able to produce. For each possible secondary, both a total production rate per capture and spectrum must be supplied. When a muon captures in aluminium, firstly the default model is run. Then for each of the secondaries produced by this, if a custom rate and spectrum have been provided for this particle type the secondary from the Bertini cascade is removed. Then, for each of the particles that do have custom rates and spectra, a particle is produced with the given probability and each of these particles assigned an energy given randomly according to the selected spectrum. By using the default model first, particles for which experimental rates or spectra do not exist can still be produced in the simulation.

There are however some downsides to this approach. Although the remnant nucleus is not actually tracked, in principle energy conservation is not guaranteed since the custom

models do not work with the default model to ensure this. In addition, the custom models cannot simulate correlations between different particle types. For example, the probability of emitting a neutron or gamma particle might be dependent on whether or not an alpha particle is emitted. Although such details cannot be included in this modelling, the impact to the outputs of the simulation are expected to be small if not negligible since the detector will see particles from hundreds of thousands of stopped muons per bunch, and will not look at the correlations between different particle types.

Finally, to handle the various spectra that might be added to the simulation, a special spectrum and spectrum-factory class design was added. The ‘COMETVSpectrum’ base-class was added to represent the abstract idea of a 1-dimensional spectrum. Custom spectra such as the Czarnecki [DIO](#) spectrum or the AlCap protons from muon capture spectrum can be included by writing a concrete instance of a spectrum, derived from ‘COMETVSpectrum’. Custom physics processes can use these spectra as they like, and since the ‘COMETSpectrumFactory’ class is able to produce concrete spectra when given a string with the name of the desired spectrum, the custom physics models can easily have different spectra selected with run-time commands. In addition, a new primary particle generator has been added which allows the momentum or energy of a particle to be set according to a named spectrum, which will be identical to the spectrum used in the tracking process. This makes it very easy to run specific acceptance studies but also reduces the effort to add a new physics model since one spectrum can be written and is immediately accessible to both the primary generators and the tracking physics.

Chapter 4.

Phase-II Optimisation

The last study into the sensitivity of COMET Phase-II was performed in 2009 [15], before the staged approach and Phase-I design had even been considered. That study found that a SES of 2.6×10^{-17} could be achieved in 2×10^7 seconds of running with a total expected background count rate of fewer than 0.34 events over the entire run period. Since then, the collaboration’s focus has shifted to design and R&D for Phase-I and no further studies have been made of the Phase-II design.

The purpose of this chapter is to make use of the updates in the fieldmap calculation, the geometry handling, and physics modelling to revisit the design of Phase-II and demonstrate that it can do at least as well as the previous 2009 design. In addition to updates in the simulation some aspects of the actual design have been refined and fixed alongside Phase-I preparation such as the experiment hall and the coils and cold-mass of the first stages of the muon beamline. The aspects of the experiment that remain open for optimisation are shown in Table 4.1.

As an initial configuration, much of the design from the 2009 study will be used, with updates included for the areas of the experiment that have since been refined by the Phase-I design.

4.1. Optimisation Strategy

Some 32 parameters are listed in Table 4.1 and yet this number alone does not describe the full challenge of optimising the Phase-II design since many of these parameters will be correlated. For example, it would seem natural for correlations to exist between the muon

Region for optimisation	Approx. No. of parameters
Production target dimensions and location	$3 + 3$
Torus1 dipole field strength	1
Torus2 dipole field strength	1
Muon beam collimator shapes, position, and material	$3 + 1 + 1$
Stopping target shape and location	$4 + 3$
Beam blocker position, form, and material	$3 + 3 + 1$
Electron spectrometer dipole field strength	1
DIO blockers in the spectrometer	4
Approx. total number of parameters	32

Table 4.1.: The list of parameters that can be optimised and an estimate for the number of parameters that this represents. In the case of the target, beam blocker and collimator shapes the number of parameters is only approximate; crudely speaking there is at least a width, length and height but in principle one could have a very irregular shape that cannot be parametrised by only three numbers, for example shapes that change as a function of distance along the beamline.

beam collimator(s), the stopping target and the beam blocker, since all involve removing or stopping muons and other particles in the beam. Other less intuitive correlations might also exist and a complete optimisation should be able to include the impact of these as well.

A complete optimisation study then can be considered a scan through a parameter space with at least 32 dimensions. A brute force search of such a space would be nightmarishly slow and require an enormous amount of computing power. Machine learning algorithms or intelligent scanning techniques might be able to tackle such a problem, and perhaps in the future these methods will be used. In the meantime however I am forced to use the technique of 'physicists intuition' to approach the problem, whereby some parameters are assumed uncorrelated whilst others are disregarded on the expectation that their impact be small.

The goal of this chapter therefore is not only to optimise the experiment but also to evaluate the correlations. Ideally this will also identify which parameters are the most strongly correlated, which would help make future optimisation studies more efficient. The outputs of this optimisation should not be considered as final but should instead be treated as a baseline from which more intelligent approaches or physicists can improve.

4.2. Production Target Optimisation

In the Phase-II Conceptual Design Report ([CDR](#)), the production target is given as being 16 cm in length and 4 mm in radius [\[15\]](#). Since then, there have been changes to the magnetic field in this region, as well as the lengths and locations of solenoids, shielding and beam-pipe, and the proton beam. Previous studies have looked at comparing the tungsten target proposed for Phase-II to other materials [\[19\]](#), and also drawn a comparison between MARS [\[27\]](#), Geant4 [\[7\]](#) and the limited data available.

The goal in this study is to optimise the production target with the up-to-date configurations. This study aims to maximise the total muon and pion yield below 80 MeV at the entrance to the Torus1 bent solenoid, by varying the radius and length of the production target.

4.2.1. Configuration

Table [4.3](#) gives the key parameters for the beam input and other aspects of this simulation. The location and orientation of the target were held fixed, since the axis of the proton beamline is fixed to intercept the muon beam axis at a given point. Once a more realistic proton beam becomes available, the location and direction of the production target would also benefit from optimisation however. During the scan over length, the back face of the target was kept 8 cm away from the muon beam since the radiation shielding has previously been optimised, and since beyond this the magnetic field will no longer be able to capture the pions and muons produced.

It must be noted that at this point in time there is an appreciable uncertainty in the proton beam profile and position. In particular, whilst the upstream proton beamline has been delivered, the effect of the magnetic field and necessary dipole and quadrupole magnets is still being studied by the proton beamline group. The beam profile is given in the Phase-I Technical Design Report ([TDR](#)) as having a Gaussian position profile and energy distribution [\[29\]](#), although no divergence or location is specified. The effect of the proton beam distribution on the overall sensitivity shall therefore have to be considered in future studies.

Protons in the simulation originated from a plane (distributed as a two dimensional Gaussian across this surface) but since there is some scope to tune the proton beam's position, the input particle plane was moved to remain 1 cm away from the front surface

Proton Beam

Horizontal spread, σ_x	5.8 mm
Vertical spread, σ_y	2.9 mm
Mean energy, μ_E	8.01 GeV
Energy spread, σ_E	0.135 MeV

Target

Material	Tungsten
Orientation	10° between target's principal axis and the muon beam axis.
Location	Back face fixed 8 cm away from muon beam axis.
Length	16 cm in CDR. Varied in steps of 4 cm from 4 to 32 cm.
Radius	4 mm in CDR. Varied from 2 to 10 cm in steps of 2 cm and from 10 to 30 cm in steps of 4 cm.

Software configuration

Packages	heads/1512w51_develop(3a0ee59)_3_UNCOMMITTED_
Externals	heads/Patch_Geant4-G4MultiLevelLocator(11fc8f0)
Fieldmap	160104 ((CHECK:))

Sample Sizes

Length scan	3×10^5 POT (30 runs of 1×10^4)
Radius scan	4.9×10^5 POT (49 runs of 1×10^4)
Final scan	

Table 4.2.: Key parameters in the configuration of the Production Target optimisation.

of the target. Since the aim is to maximise the muon and pion yield by varying only the length and radius, shifting the proton beam input plane in this way removes any variation of target acceptance due to divergences of the proton beam in the field before the target.

4.2.2. Length Scan

Different length targets were simulated with 3×10^5 POT per length. The target length was varied in steps of 4 cm from 4 to 32 cm, whilst the target radius was held fixed at the CDR value of 4 mm.

Fig. 4.1 shows the momentum distributions of pions and muons for different target lengths, which are given as half-length following the Geant4 convention. Fig. 4.2 then

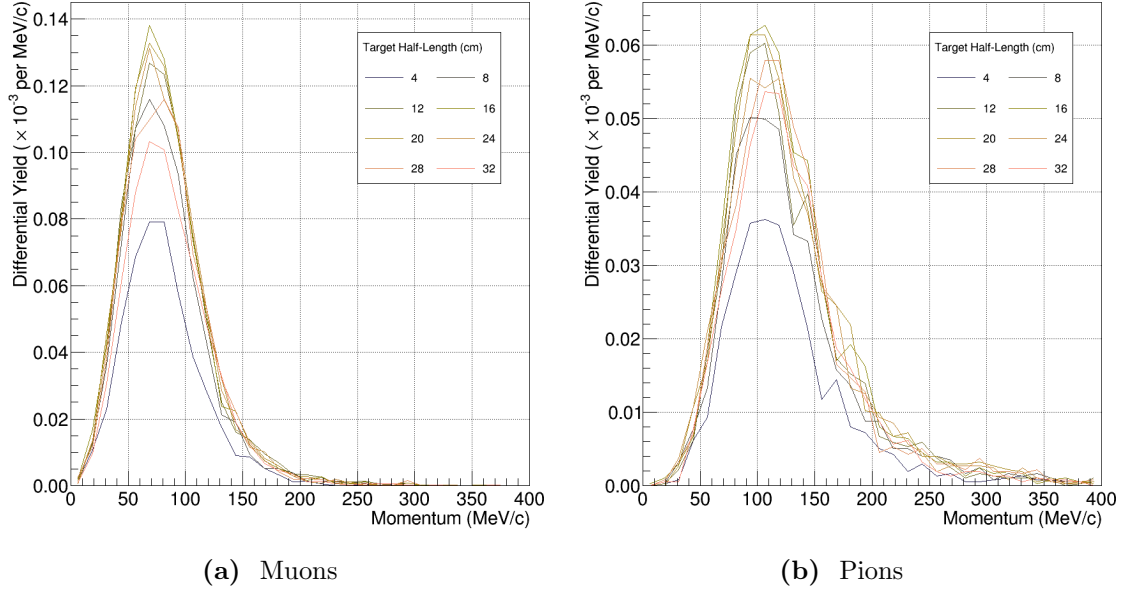


Figure 4.1.: Change to momentum distributions at the entrance to the first 90 degrees of the bent muon beam solenoid for different target lengths. Target length is given as half-length which is the Geant4 convention.

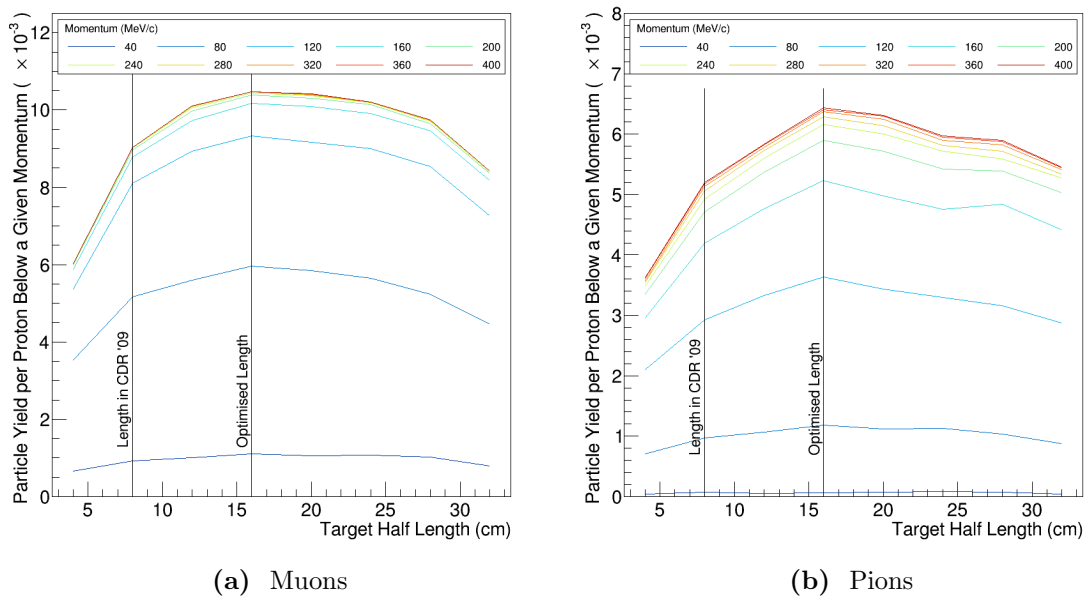


Figure 4.2.: Integrated muon and pion yields up to a certain momentum at the entrance to the first 90 degrees of the bent muon beam solenoid as a function of target length.

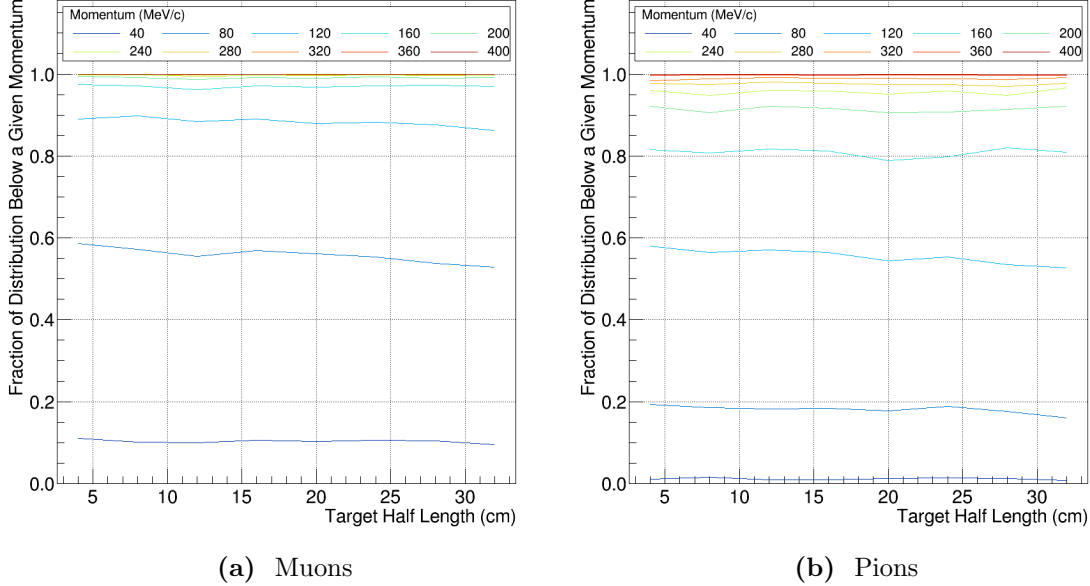


Figure 4.3.: Change in the momentum distribution of muons and pions at the entrance to the first 90 degrees of the bent muon beam solenoid as a function of target length.

shows these distributions integrated up to different momenta. From these plots it can be seen that for both muons and pions, the optimum target length occurs around a total length of 32 cm.

Additionally it can be seen from Fig. 4.3 that the shape of the momentum distributions changes only weakly as a function of the target length. These plots were produced by normalising the integrated momentum contours of Fig. 4.2 to the total integral below 400 MeV. As a result, it is possible that the actual shape variation is even weaker than apparent here, since in the present sample size, the high momentum tail is not well sampled at small target lengths, such that a skew in the normalisation might occur.

4.2.3. Radius scan

In parallel to the length optimisation scan, different radii targets were also simulated. Targets with radii of 2, 4, 6, 8, 10, 14, 18, 22, 26, and 30 mm were tested. The target length was held at the CDR value of 16 cm in total.

The results of these scans can be seen in Fig. 4.4 and Fig. 4.5, where it can be seen that a maximum in both the muon and pion yields at the entrance to the Torus1 section

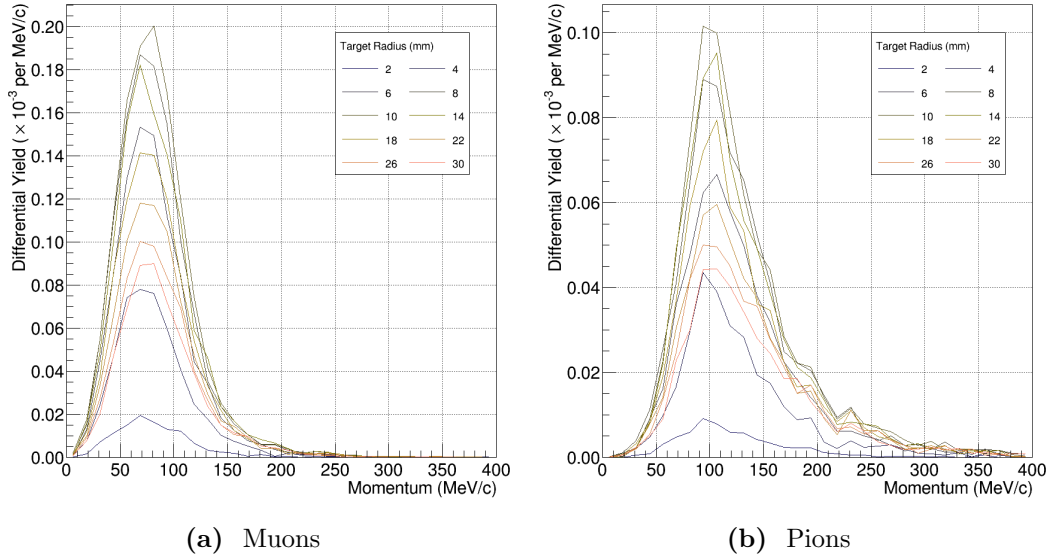


Figure 4.4.: Change to momentum distributions at the entrance to the first 90 degrees of the bent muon beam solenoid for different target radii.

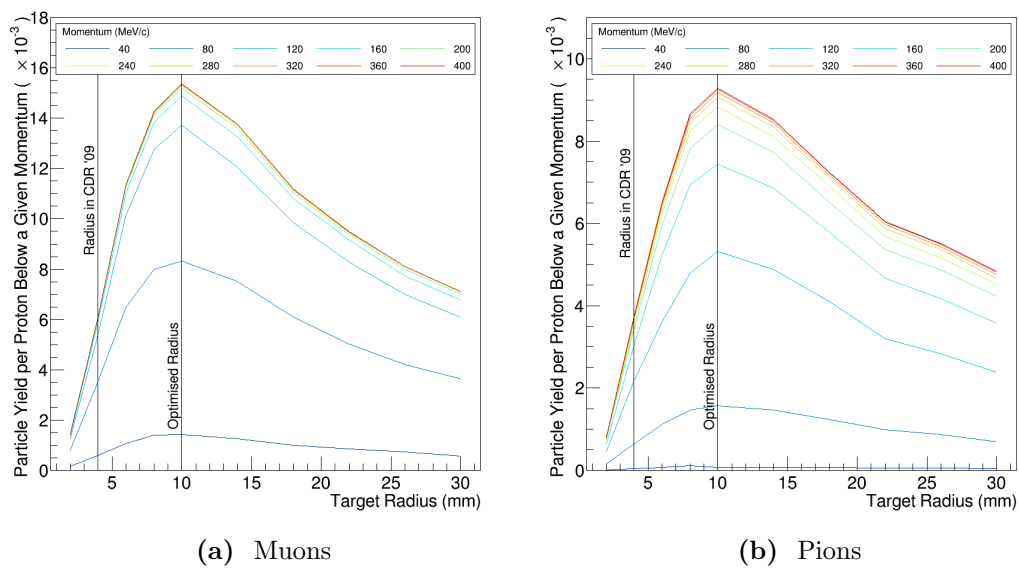


Figure 4.5.: Integrated muon and pion yields up to a certain momentum at the entrance to the first 90 degrees of the bent muon beam solenoid as a function of target radius.

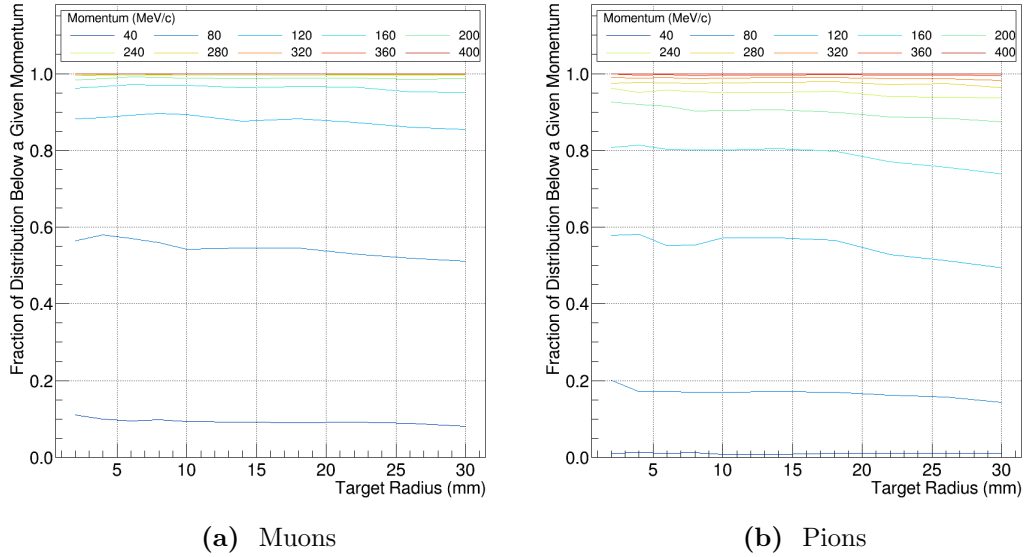


Figure 4.6.: Change in the momentum distribution of muons and pions at the entrance to the first 90 degrees of the bent muon beam solenoid as a function of target radius.

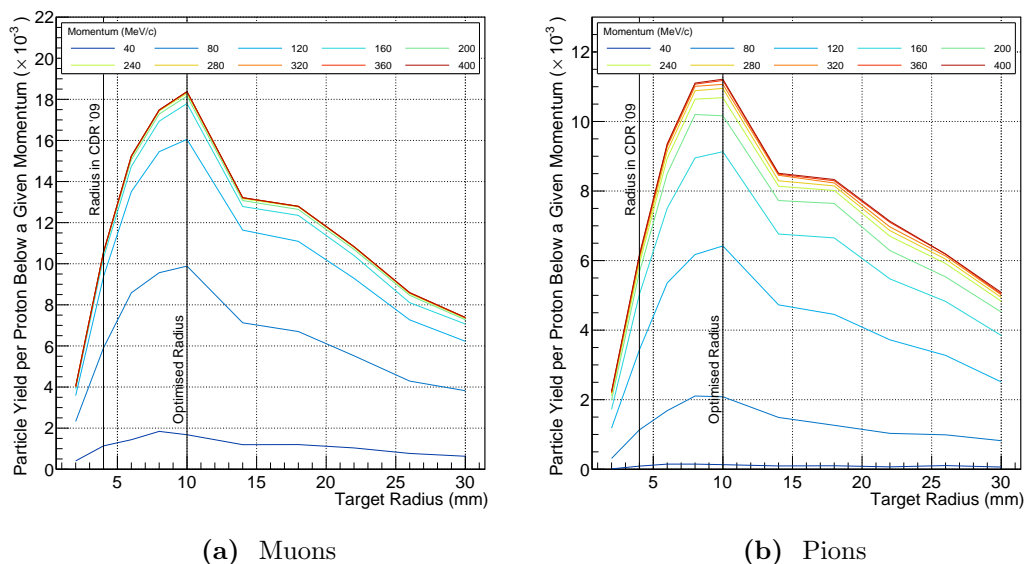


Figure 4.7.: Variation in muon and pion yields as a function of target radius when the total target length is set to the optimised value of 32 cm. Despite the longer target length the optimal radius is still 1 cm.

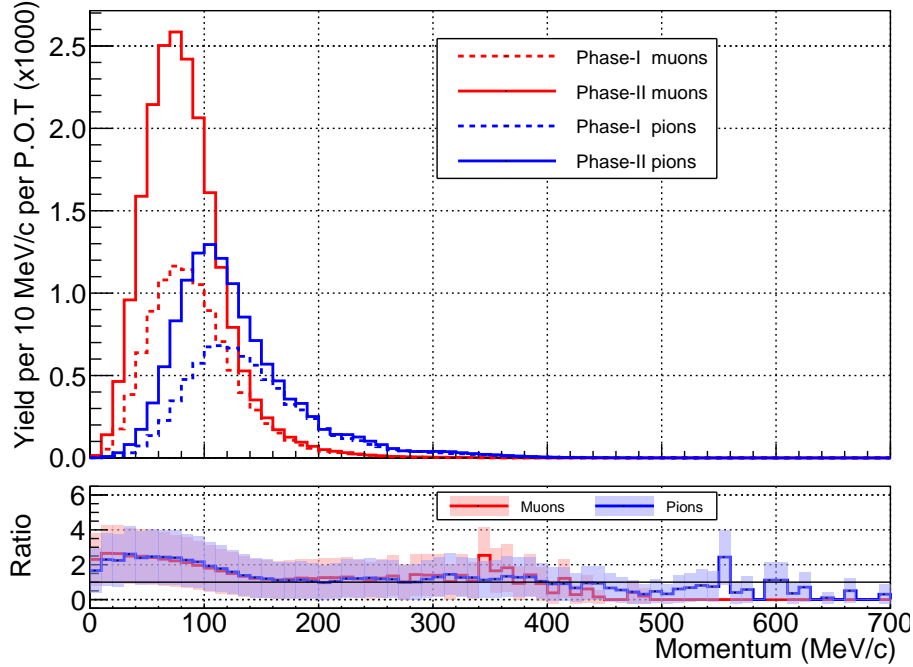


Figure 4.8.: Comparison of the muon and pion yields per POT for Phase-I and Phase-II. The difference arises from the change of target material between the phases.

is achieved at a radius of about 10 mm. As in the length scan, the variation in the shape of the momentum distributions is rather weak as a function of target radius.

4.2.4. Final Result

Since the length and radius scan were performed in parallel, a final cross check was performed where the optimal radius was confirmed at the optimised target length. The integrated spectrum is shown in Fig. 4.7 where it can be seen that the optimum radius once the target length is increased to 32 cm is still 10 mm.

Fig. 4.8 shows the total muon and pion yields at the entrance to the Torus1 for the final optimised Phase-II target and compares this to the optimised Phase-I target design. The increased yield in the low momentum range is due to the heavier target nucleus which produces more low-momentum pions in the backwards direction. Since only muons below around 50 MeV/c tend to stop in the target, this increase in the low momentum yield amounts to a factor 2 or so gain in the stopping muon rate per POT.

<i>((CHECK: Fill this table in properly))</i>	
Pions and muons from Prod. Tgt. simulation	
Software configuration	
Packages	---
Externals	---
Fieldmap	160104 <i>((CHECK:))</i> with additional scale factors applied to Torus dipole field
Sample Sizes	
Final scan	

Table 4.3.: Key parameters in the configuration of the muon beamline dipole field optimisation.

4.3. Dipole Strengths of the Muon Beamline

The full 180° bent solenoid that makes up the bulk of the muon transport beam line is actually broken down into two 90° pieces – Torus1 and Torus2 (also known as TS2 and TS4 by the magnet group). Each of these sections has its own dipole field which need not provide the same dipole field strength. The Torus1 section has been built already and was previously optimised for both Phase-I [29] and Phase-II [15]. The dipole coils that it contains are designed to produce a dipole field of 0.055 T. By running a lower current through these coils one could reduce the Torus1 dipole field without too much effort. However if Phase-II should require a greater dipole field strength for this region that might be trickier since it could require additional windings to be inserted – this would not be impossible but might costly.

4.3.1. Large-sample Production Target Simulation

Before the muon beam section could be optimised, a large set of **POT** events were produced transporting all particles up to the entrance of the muon beam section. In total, 2.3×10^8 POT were simulated through this stage, equivalent to about 1.5 bunches at Phase-II. The production target used the optimised geometry from the previous section. All particles that hit the surface of the Torus1 container volume were read out for later re-use in a way that ensured double-counting of particles could not occur. In addition, particles entering the proton beam dump were also saved if later simulations wished to study their impacts.

4.3.2. The Optimised Dipole Field Strengths

The figure-of-merit for this optimisation is the muon stopping rate, which will be maximised at the optimal field configuration. To identify such a configuration, a 2D-grid scan was done where the Torus1 and Torus2 dipole fields were simultaneously varied. Varying the field strength was done by applying a scale factor to the fieldmaps for each 90° section described in 3.3.2. These scale factors were varied in steps of 0.125 (equivalent to 6.875 mT) and for each point muons and pions from 8×10^6 POT were transported to the stopping target. The stopping rate for each combination of scale factors was then assessed.

The muon stopping rate as a function of the two dipole field strengths are shown in Fig. 4.9. A scale factor of 1 on the x-axis means no change to the current Phase-I design and since there is little improvement by moving to larger values for Torus1 the optimal scale factors are chosen to be 1 and 0.5 for the Torus1 and TTorus2 respectively. This translates to dipole field strengths of 0.055 and 0.0275 T respectively.

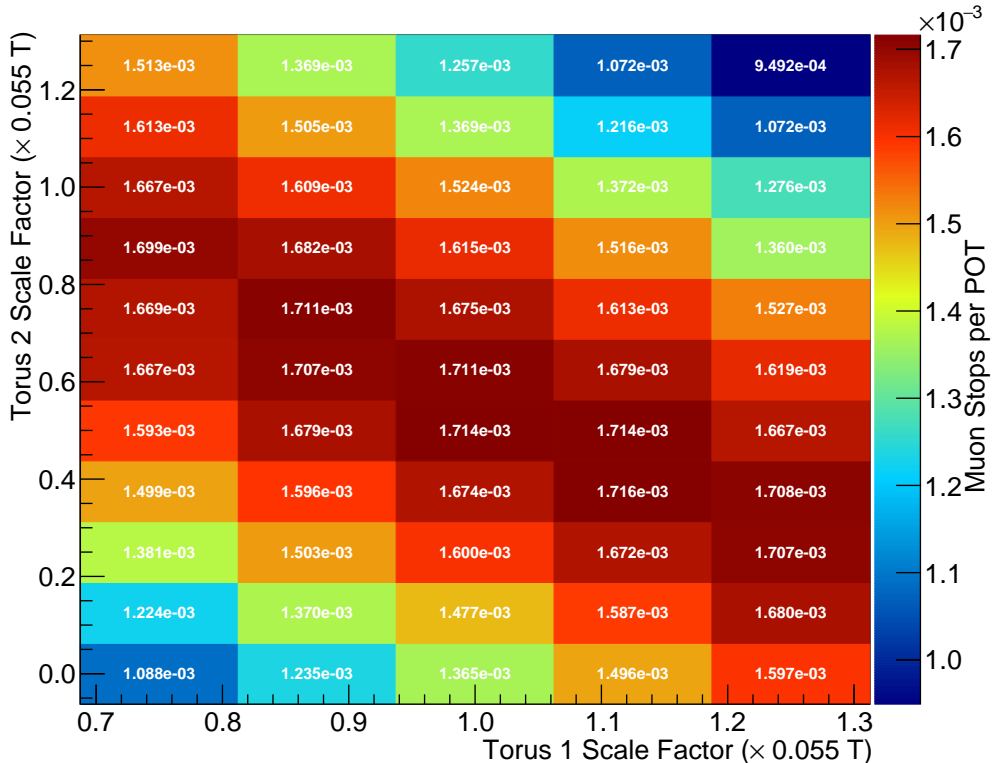


Figure 4.9.: Muon stopping rate as a function of the two dipole field strengths (given relative to the Phase-I design specification). A clear anti-correlation is visible which is discussed in the text.

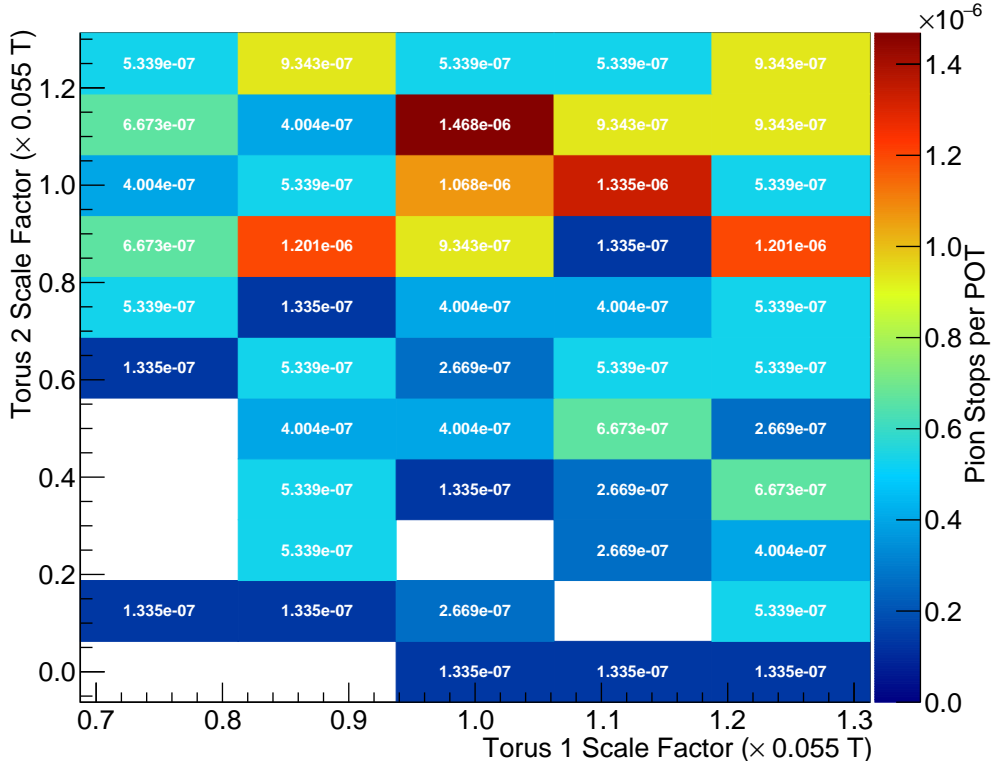


Figure 4.10.: Pion stopping rate as a function of the two dipole field strengths (given relative to the Phase-I design specification). At the level of statistics used to generate each point, no clear trend is obvious. Empty squares are those where no pions stopped in the run.

Also striking from Fig. 4.9 is the anti-correlation between the two dipole field strengths. Roughly speaking the sum of the optimal dipole field values is constant, i.e. $B_1^{\text{optimal}} + B_2^{\text{optimal}} = \text{const}$. Although this was not previously foreseen, such a correlation can be understood accordingly. The stopping target geometry and position is held fixed in this parameter scan, which essentially fixes the upper momentum of muons that can stop in the target. The drift of a particle due to the dipole field is proportional only to the distance travelled in that dipole field and the dipole field strength, and does not depend on the particle's momentum. This means that the total drift due to the Torus1 and Torus2 dipole components is proportional to the weighted sum of the two dipole field strengths, where the weight is the distance travelled through each of the two sections. Since each section is the same length, the time for a particle to pass through Torus1 will be roughly the same as the time in Torus2 so that the weights would be roughly equal. This leads to the total drift being proportional to the sum of the two dipole fields. Since the production target (as the source of muons) and stopping target (as the muons'

destination) are at a fixed height with respect to one another the optimal vertical drift is also fixed so that the sum of the dipole field strengths should also be roughly fixed.

With that said, the Torus1 section has a higher pion flux which causes some assymetry between the two sections. Keeping more pions on-axis in the Torus1 section means that more muons will enter the Torus2 section from those pions that have decayed. But since the pion momentum distribution is slightly higher than the muon distribution keeping pions on axis requires a larger dipole field strength. This could explain the slight assymetry where the muon stopping rate appears slightly larger if Torus1's field is larger than that of Torus2.

It is also interesting to consider the pion stopping rate as a function of the dipole field strengths. However, as can been from Fig. 4.10 the stopping rate is close to the level of POT events used in the simulation so that the plot is dominated by statistical fluctuations.

4.4. Electron Spectrometer's Dipole

The next element in the beamline after the muon transport solenoids will be the stopping target. However, in order to study the impact of changing the stopping target parameters one will need to look at the impact on the signal acceptance into the detector. To study that requires the components of the beamline intermediate to the target and the detector be optimised, namely the electron spectrometer. The key free parameter in this section is the dipole field strength along the spectrometer. The solenoidal field and solenoid aperture could also be optimised in principle, but these are considered beyond the scope of this study at this point and so the CDR values are held fixed here. The point of this section is to establish the optimal dipole field strength given fixed target parameters which will then be studied separately together with the stability of the dipole field tune checked.

4.4.1. Method and Potential Short-comings

To study the effect of the dipole field on signal acceptance, a realistic muon stopping distribution in the target was produced by transporting muons from the production target simulation through to the stopping target. Signal electrons were then injected at

the target with the realistic stopping distribution and propagated through the beamline to the detector with different dipole field strengths.

A non-trivial short-coming of the current study is that the dipole field along the spectrometer is poorly modelled – no realistic coil simulation exists, unlike for the bent muon transport beamlines. As a result, a perfectly uniform dipole field is assumed with a sharp switch on and off at the entrance and exit of the spectrometer. The impact that this has on the final result is not clear: one might expect it to be small given the relative strengths of the dipole and solenoidal fields and overall it is the integrated field that tends to matter. However, the sharp switch-on of the field at the entrance and exit of the spectrometer is clearly not physical. Given that the gradient introduced in the field by bending is present before the actual entrance and exit of the spectrometer (as a fringe field), some drift can be anticipated in this region. A realistic dipole field with a realistic fringe field might overcome some of this drift however, so that the uniform field used here will most likely not capture this effect. Nevertheless, given the absence of a realistic dipole field and scope of this study, the uniform one is the only real option at this point.

4.4.2. Results

Fig. 4.11 shows the projection of electron trajectories to the beam axis coordinate system for three different dipole field values. The potency of this approach is clear from these plots; the tuneable dipole fields allow the momentum of electrons which remain on-axis to be accurately controlled (during run-time), which will benefit systematic and calibration studies that wish to study the DIO spectrum at a lower energy. Fig. 4.12 then collects these plots with other dipole field strengths, plotting the mean height for all simulated electrons against the distance along the beam axis. From this plot it can be seen how a dipole field of about 0.18 T appears optimal to keep the signal electrons on axis.

The probability for electrons to reach a given point in the beamline is shown in Fig. 4.13, and indeed from this it can be seen that to maximize the probability of an electron reaching the detector a dipole of around 0.18 T is desirable. The behaviour of the low dipole field values (0 to 0.08 T) in this plot was not expected, but it is believed this is an artifact of the way this plot is made, coupled with a degree of mirroring at the entrance to the spectrometer which is enhanced as the dipole field strength increases. If correct, a realistic dipole field calculation would be important to quantify and confirm this behaviour.

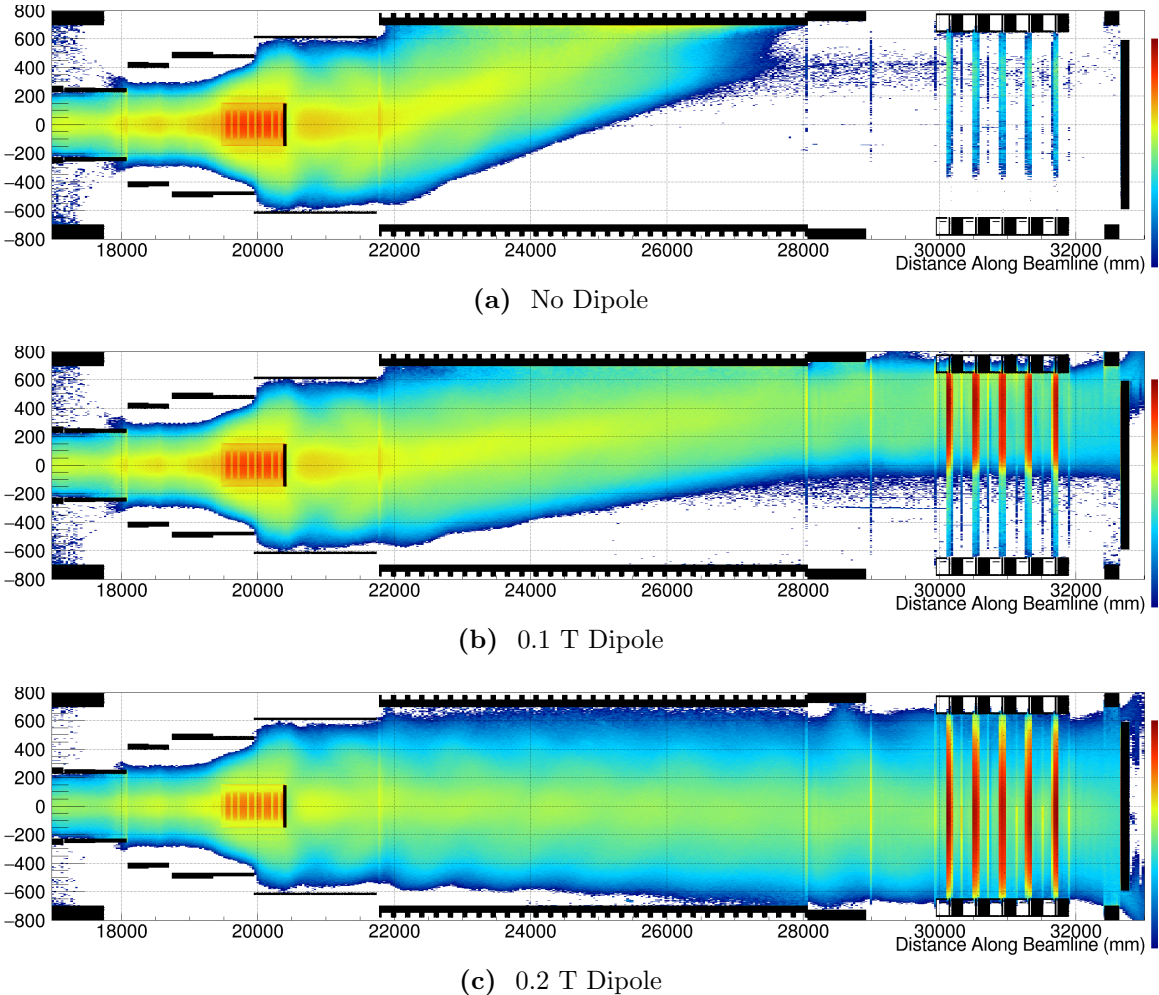


Figure 4.11.: The heights of signal electrons for different dipole field values.

Finally, to confirm the optimal dipole field strength the true geometric acceptance of the detector system is checked as a function of the dipole field strength, which is shown in Fig. 4.14. An electron is considered to have been geometrically accepted by the detector in this simulation if it produces at least one hit in the detector system. In principle this could be in any straw plane, but in practice this is almost always in the first layer of straws. Since this is a different way to analyze the acceptance compared to the survival probability it would not suffer to the artifact seen for low dipole field values in Fig. 4.13. Nonetheless, Fig. 4.14 confirms that the optimal dipole field strength is very close to 0.18 T.

A second important conclusion can be drawn from the fact that the dependence on the dipole field strength is relatively weak around the optimal value of 0.18 T. A change

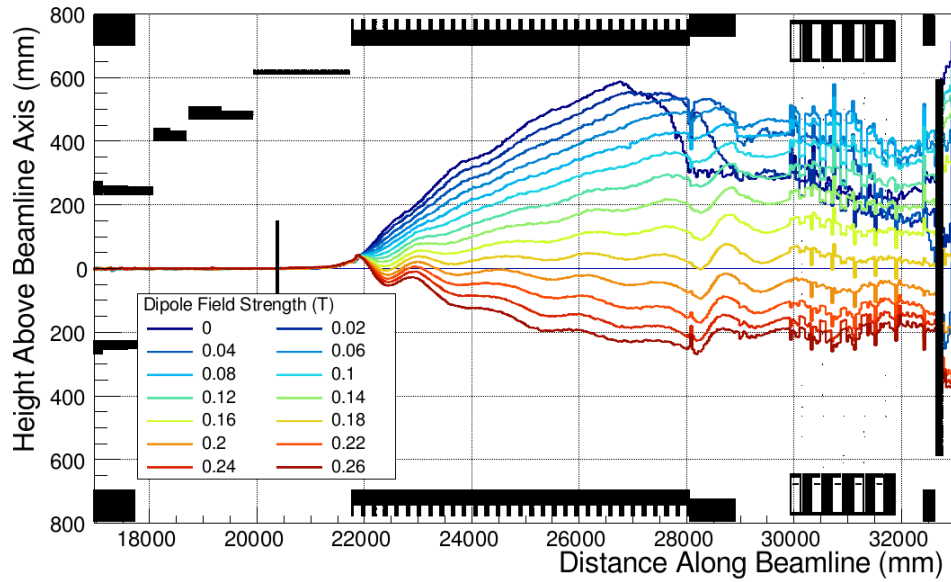


Figure 4.12.: Mean height of signal electrons for different values of the dipole field strength.

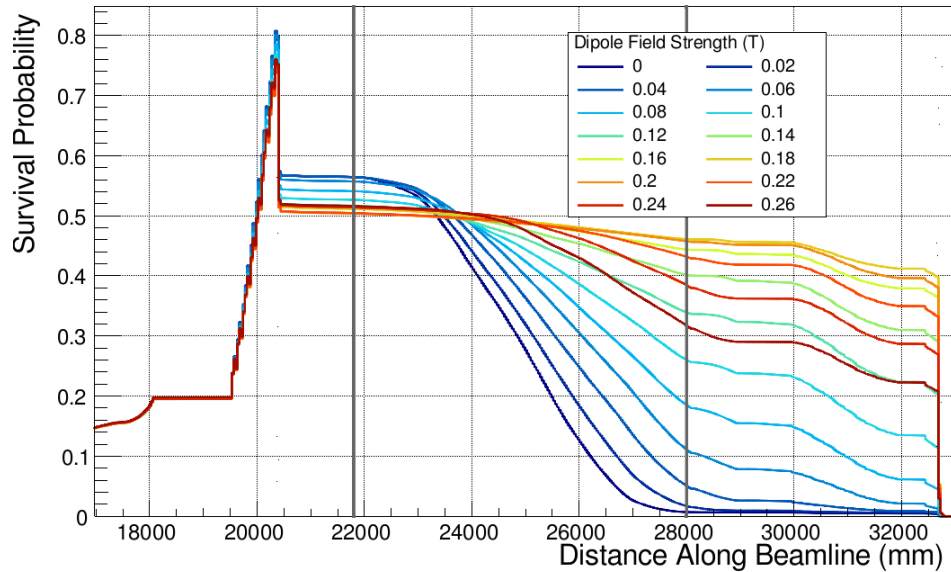


Figure 4.13.: Survival probability for signal electrons as a function of the distance along the beamline for different values of the electron spectrometer's dipole field strengths.

of about 10% in the dipole field strength only reduces the signal acceptance by about 3% whilst a change of about 5% would see a reduction of only about 0.7%.

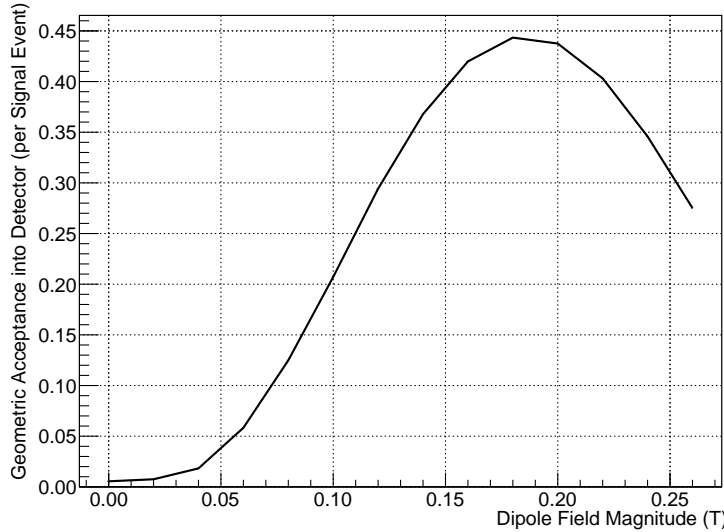


Figure 4.14.: Geometric acceptance into the StrECAL detector as a function of the dipole field strength over the electron spectrometer.

4.5. Stopping Target Position

The final aspect to be studied with regards to maximizing the signal sensitivity is the stopping target. In principle there are many parameters related to the stopping target such as the location, disk shape (profile and thickness), and disk spacing. In addition the beam blocker should be considered in parallel with the stopping target since it sits so close to the target itself and can be expected to have a big impact on the signal acceptance. However, this leaves far too many parameters to be considered all at once.

Since the field around the target tapers sharply various competing factors must be considered. For example, prior to the stopping target region the muon beam is transported through a 3 T solenoidal field. The magnetic field in the target region, however, tapers to about 1 T, which would cause the envelope of the muon beam to grow. Moving the stopping target downstream would mean that the muon beam arrives with a larger aperture, and would therefore prefer a larger stopping target or else fewer muons will actually hit the target. On the other hand, from the perspective of signal acceptance, the tapered field can be used to mirror signal electrons that are initially produced heading upstream therefore increasing the signal acceptance. Moving the target further upstream then will reduce this effect as the difference between the magnetic field strengths at the exit of the bent muon transport solenoid and at the stopping target is reduced.

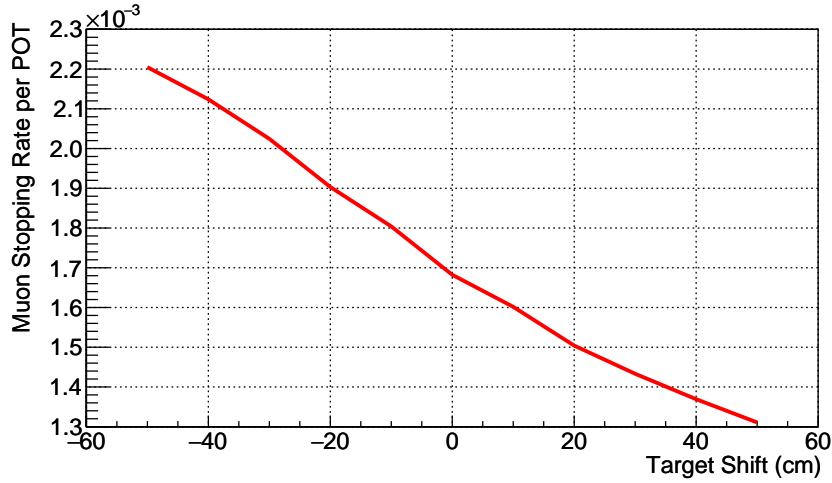


Figure 4.15.: Muon stopping rate per POT for different target positions. The linear behaviour arises from the reduced field strength and fixed target radius such that fewer muons impact the target as it is moved downstream.

Given this and the need to reduce the number of parameters inspected, the target and beam blocker design was held fixed in this study and only the position was changed by moving the target upstream and downstream by ± 50 cm with respect to the nominal target location as given in the CDR [15]. Given that the target disks will occupy in total about 1 m, a shift of 50 cm corresponds to half the target length. In each different position of the stopping target, as for the spectrometer dipole optimisation, a realistic stopping distribution was produced by running muons from the large-scale production target simulation through to the target. This stopping distribution was then re-used to introduce signal electrons accordingly. Additionally, low momentum electrons were also studied in order to study the impact of target position on the height of both signal and low-energy electrons as they pass through the spectrometer. This is important both to check the correlation of the dipole field tune with the stopping target position, but also how the subsequent DIO blocker height optimisation will correlate the target position.

Fig. 4.15 shows how the rate of muon stops per POT is affected by changing the position of the stopping target. The relationship is roughly linear, dropping from around 2.2×10^{-3} muon stops per POT when the target is shifted upstream by 50 cm to about 1.3×10^{-3} muon stops per POT if the target is shifted 50 cm in the other direction. This relationship is as expected given the fixed radius of the target and the growth of the muon beam aperture arising from the reduction in the field strength.

In Fig. 4.16 one can see the way the electron acceptance changes for different target positions. Acceptance here is defined as producing at least one hit in the detector and

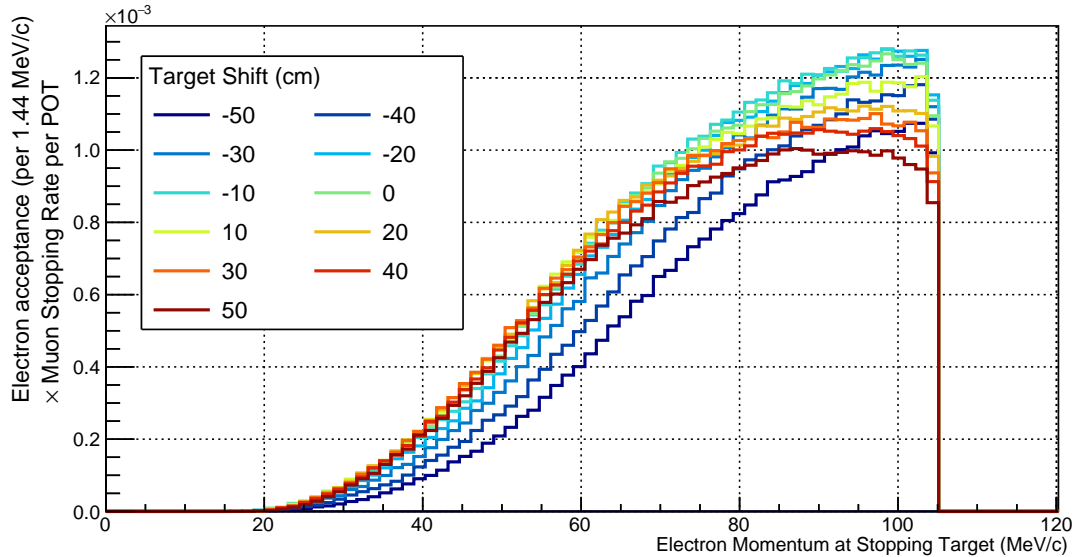


Figure 4.16.: The momentum dependence of the electron acceptance into the detector for different target positions. The spectrum for each target position is normalised to the muon stopping rate for that position, such that each The linear behaviour arises from the reduced field strength and fixed target radius such that fewer muons impact the target as it is moved downstream.

the momentum shown is the momentum at the target, which is not necessarily the same as the momentum at which the electron is observed. Each histogram in Fig. 4.16 is normalised to the number of primary electrons introduced at the target per MeV/c and then scaled to the muon stopping rate. This normalisation makes the value of each curve proportional to the sensitivity of the experiment to different momentum electrons, up to factors such as analysis cuts like timing and reconstruction quality.

Since the parameter we wish to optimise here is the location of the stopping target, Fig. 4.17a represents the same data as in Fig. 4.16 but with each line representing the content of a different $5 \text{ MeV}/\text{c}$ bin as a function of the target position. For signal, it is the $105 \text{ MeV}/\text{c}$ line (dark burgundy) that is most important and it can be seen that this is optimised for shifts upstream of the nominal position from between 10 and 20 cm. It is also interesting to note that the acceptance of lower energy electrons is relatively decreased as the target is moved upstream, as can be seen in Fig. 4.17b. This could be useful as a way to suppress hit rate from DIO electrons later.

Whilst we do not intend to optimise the beam blocker at this point, to check the impact that it has on the optimisation of the target position simulations were performed where the blocker was completely removed. Fig. 4.18 shows the product of the stopping rate and electron acceptance when the blocker is removed. From this the trend is much

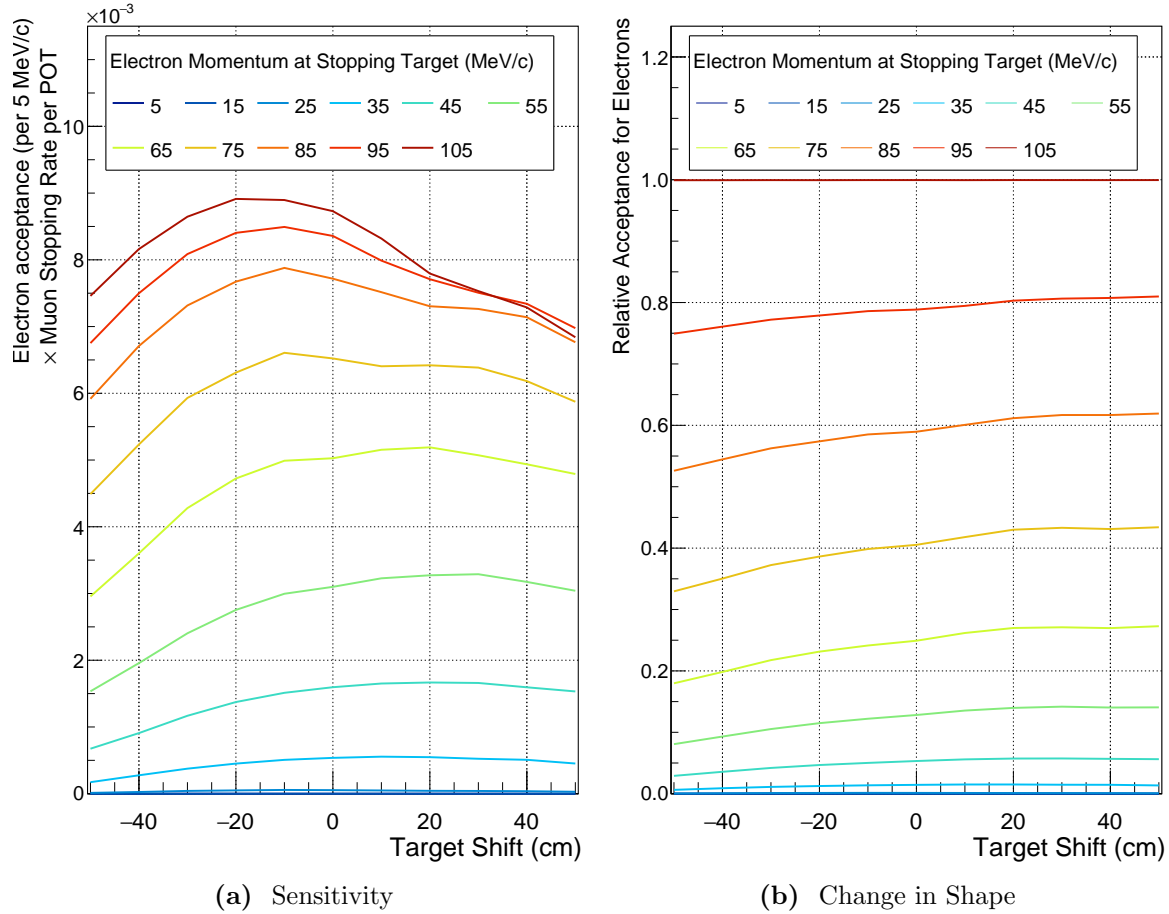


Figure 4.17.: (a) The variation in sensitivity (acceptance \times stopping rate) to electrons with different momenta as a function of the target position with respect to the nominal location. The darkest red line towards the top of the plot represents the sensitivity to signal, and it is that line that should therefore be maximised. (b) The change in the shape of the acceptance vs. momentum spectrum as a function of the stopping target location.

cleaner, electrons below 70 MeV/c are suppressed as you move the target upstream whereas the high energy electron acceptance increased.

Finally the relationship between the stopping target position and the mean height of electrons through the spectrometer is demonstrated in Fig. 4.19. Each plot shows the mean heights for electrons with a given momentum for different stopping target positions and it is clear that there is some correlation between the mean height and the position of the stopping target. For this reason, a more complete optimisation should consider optimising the two parameters simultaneously. Nonetheless the change is not particularly large, only about a few cm difference by the end of the spectrometer for signal electrons.

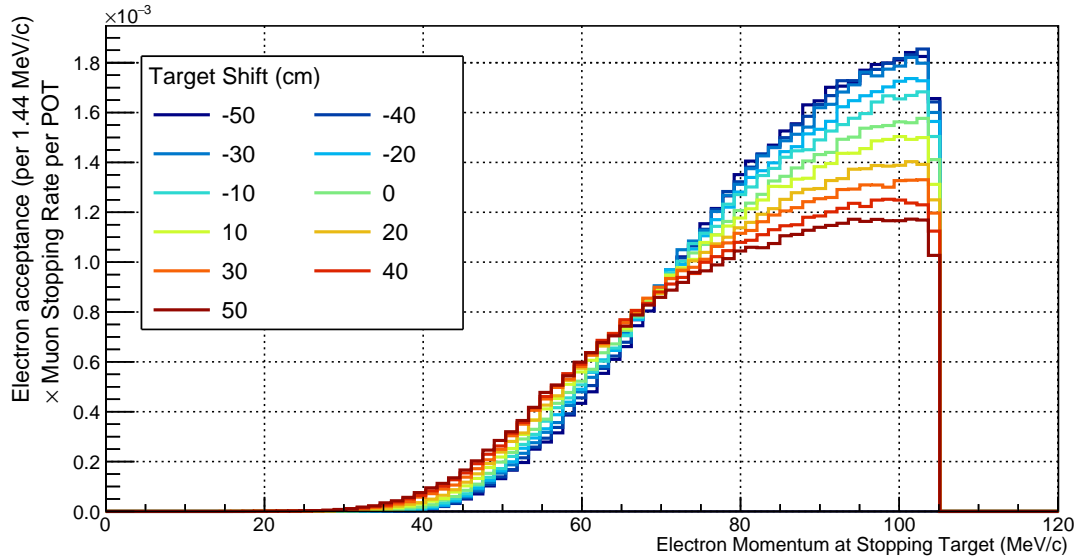


Figure 4.18.: The momentum dependence of the electron acceptance into the detector for different target positions when the beam blocker is removed.

This correlation is also likely related to the way the acceptance changes for different target positions when the beam blocker is removed.

The second striking feature from the plots in Fig. 4.19 is the way the mean height acquires a strong sinusoidal component for large target shifts upstream. This suggests that when the target is shifted upstream the electrons passing the entrance to the spectrometer tend to have a particular value for the pitch and phase angles of the trajectories. Several separate mechanisms could produce this effect. Firstly the acceptance around the target itself could acquire a stronger preference for certain pitch and phase angles when the target is moved upstream. Secondly, since the stopping target disks will see more of the muon beam upstream, the muon stopping distribution could become less homogenous. Whilst electrons are produced isotropically path with less target material along them will tend to accept outgoing electrons more readily such that if more muons stop at one side of the target than the other a dependence on pitch and phase could arise.

Clearly then the stopping target region is a very complicated area; even though this study has focussed on a single parameter – the position of the target itself – it is clear that this correlates to many other variables. This is a region in the experiment most ripe for further optimisation then, and indeed appendix C shows some of the first steps that have made in this direction since the optimisation described here was completed. Unfortunately, at the time this work was carried out an error in the normalisation of these plots lead to the conclusion that the optimal shift was between 0 and 10 cm upstream.

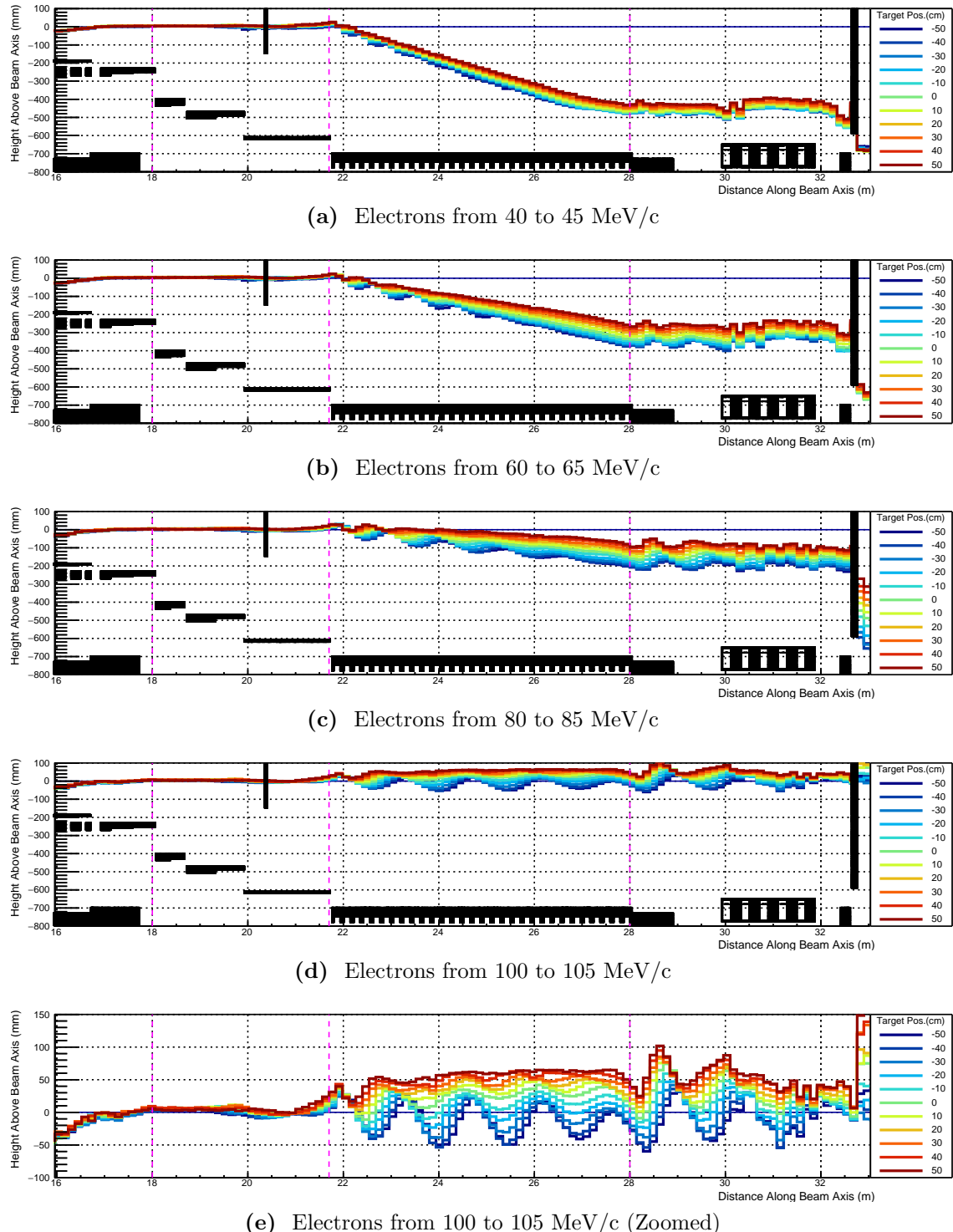


Figure 4.19.: The effect of stopping target position on the height of electrons with a fixed momentum as they pass through the Electron Spectrometer. The size of the variation indicates the stability of the dipole tune; the two parameters are clearly correlated. Also striking – particularly in (e) – is the way the dependence on the helical pitch angles is affected by the stopping target position.

Given the complexity of the optimisation in this region, it was therefore decided to keep the stopping target at the nominal location for the subsequent steps. Having corrected the normalisation of the plots, the conclusion now is that the optimal location is between 10 and 20 cm upstream, so perhaps the target should have been shifted back. However the improvement to the sensitivity would have been small: shifting the target back about 20 cm improves the sensitivity by around 2% compared to the signal acceptance at nominal position.

4.6. Collimators in the Muon Beamline

With the beam line optimised for high signal efficiency, one can look at improving the background by adding collimators into the muon beam line to reduce the flux of high-momentum muons and pions.

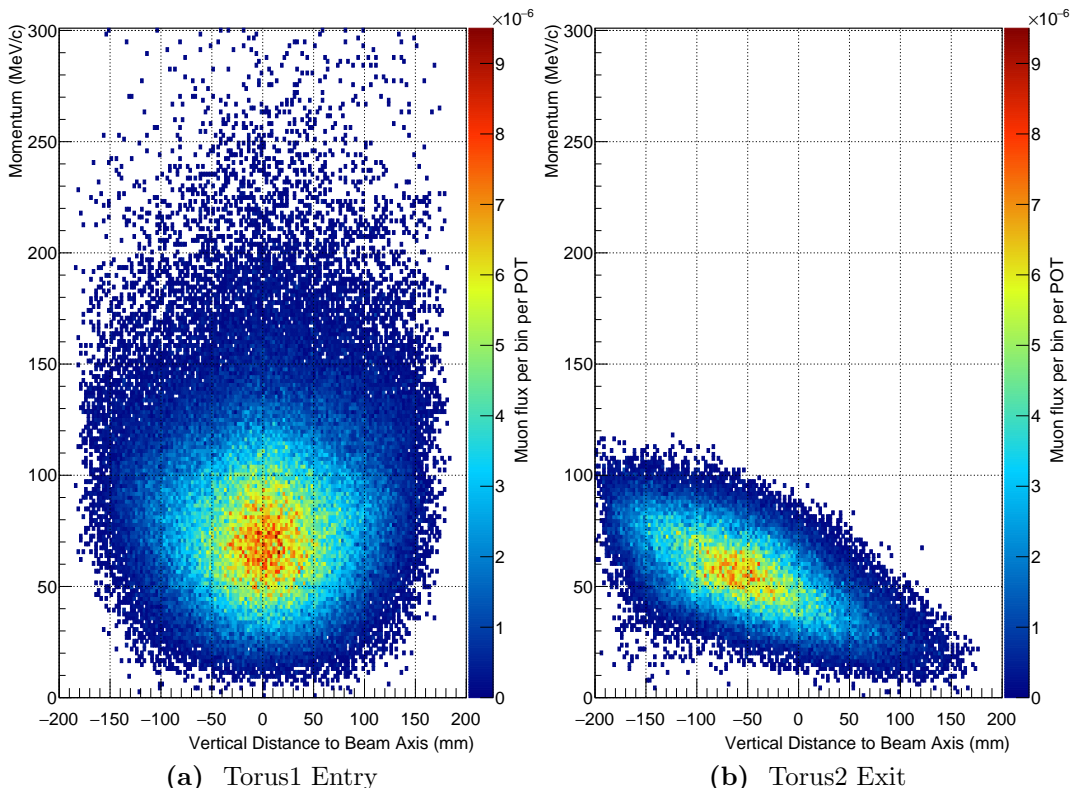


Figure 4.20.: Dispersive effect of the 180° bent transport solenoid and dipole field on muons. No collimating material is yet included, so the high-energy muons being removed is due purely to the beam-pipe itself.

Fig. 4.20 shows the dispersive effect of the bent solenoid and dipole field on muons passing through the beamline. Thanks to this dispersion low momentum muons that can stop in the target and high momentum muons which could produce backgrounds are separated sufficiently so that material in the beam pipe can selectively remove the dangerous, high-momentum muons with only a small impact on the muon stopping rate.

4.6.1. Collimator Placement

The plots in Fig. 4.21 give a sense of where best to locate the collimating material. In Fig. 4.21a the paths of all muons along the beamline is shown. Fig. 4.21b then separates out the muons that stop in the target which should be compared to Fig. 4.21c showing the paths of muons that reach the stopping target region with momentum greater than 70 MeV/c (the threshold for a muon to decay to an electron with $p > 100$ MeV/c).

It is interesting to note the apparent asymmetry in the high-momentum muons at the entrance to the Torus1 that can be seen in Fig. 4.21c. This is not because of some momentum-dependence in the acceptance of the preceding beamline, but due to the fact that muons in that plot are only included if they are ‘dangerous’ in the region around the stopping target. Even without additional collimators, the beam pipe itself removes high momentum muons that enter in the lower half of the beamline. The validity of only tagging high momentum muons around the stopping target region comes from the assumption that the products of high-momentum muons that decay before this region can be reliably removed. It is important then that this assumption be checked, but for this work this is left as a task for the future.

Finally then in Fig. 4.21d the difference between the high-momentum muons and the paths of those that stop is shown. Regions in blue on this plot show where many more high-momentum muons pass than stopping muons; it is in these locations that collimator material will be most effective. This approach could also be improved, since taking the straight difference between the two plots implies equal weighting for stopping muons and high-momentum ones. In reality, whilst a muon tagged as stopping is definitely going to stop, a high-momentum muon should be weighted by the probability to produce a signal-like electron and the probability that this electron survives to be accepted into the detector, passing all analysis cuts. This would make the weighting for the high-momentum muons be a function of the beamline distance itself which again requires a study into how high-momentum electrons are accepted. However for the purposes of obtaining a qualitative sense of where to collimate the unweighted difference should be sufficient.

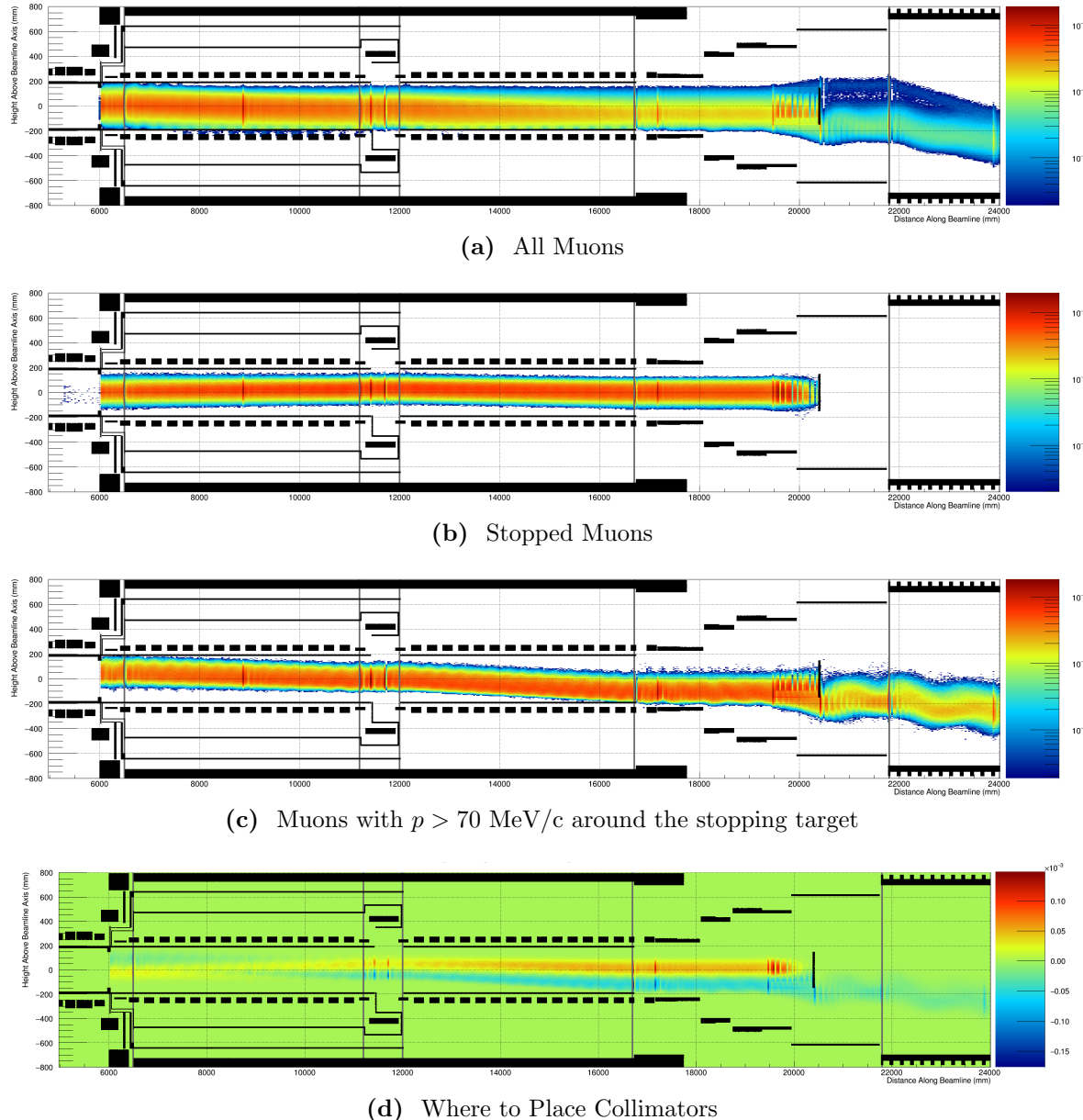


Figure 4.21.: The heights of muons as they pass along the beamline. (a) The path of all muons. (b): The paths of muons that stop in the target. (c): The heights of muons with momentum greater than $70 \text{ MeV}/c$ when they enter the region around the stopping target. These could potentially decay in flight to give electrons with $100 \text{ MeV}/c$ or greater. (d): The difference between plot (b) and plot (c). Regions in dark blue would give the greatest impact in removing high momentum muons whilst leave the stopping muons untouched. These plots should be compared to those of Fig. 4.26 once collimators have been introduced.

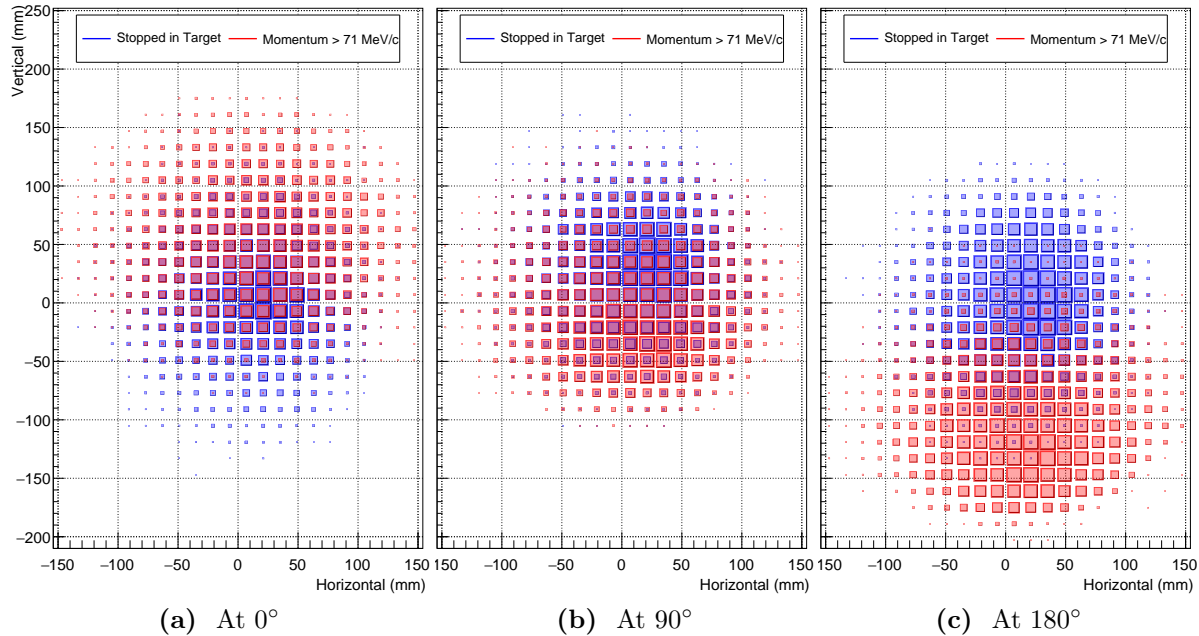


Figure 4.22.: The separation between stopping and dangerous muons. The separation is largest at the exit (180°), reasonable at the entrance (0°), and smallest around the mid-point (90°).

Two regions of interest appear: in the upper half of the entrance to Torus1 and the lower half of the exit of Torus2. Collimating at the Torus1 entrance is justified by the basis that high momentum muons will tend to have larger gyroradii compared to the muons that stop, and that at this point the beam is largely on-axis and has not yet been dispersed. Collimating at the exit of Torus2 is readily understood on the grounds that the high momentum muons will have all drifted downwards by this point, compared to the low momentum stopping muons which are kept on-axis by the dipole fields.

These conclusions are backed by the plots shown in Fig. 4.22 which show transverse slices through the beamline at the entrance to Torus1 (0° of bent solenoid), the midpoint between Torus1 and Torus2 (after 90° of bent solenoid) and at the exit of Torus2 (after 180°). From these plots one can also see how in the middle of the bent solenoids (at 90°) the separation between muons that will stop and those that will have momentum greater than or equal to 70 MeV/c in the stopping target region is weakest, and hence collimators in this location will not be so effective.

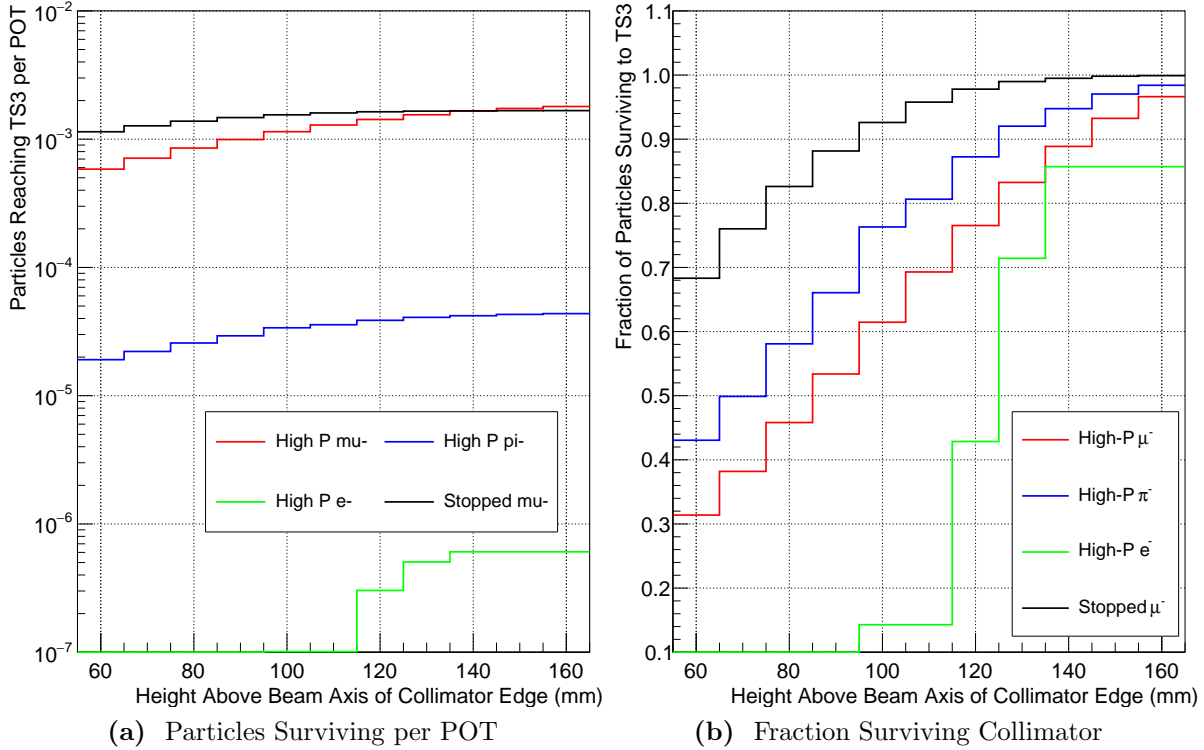


Figure 4.23.: The effect of changing the height of the collimator in Torus1 on the particle distributions.

4.6.2. Collimator Height Optimisation

To identify the optimum height for the collimators in a computationally efficient way, events were generated without any collimators included. The full three dimensional trajectory of all particles as well as the decay tree were persisted. This allows for a ‘virtual’ collimator to be used, where particles that enter a defined region and their secondaries are removed from the downstream plots. Whilst this method allows for many collimator shapes and heights to be tested quickly, it comes with a couple of limitations. Firstly, the accuracy depends on the trajectory sampling density, which should be fine but this results in large data sizes. Secondly, realistic material effects of the collimator cannot be captured, such as the probability a particle is simply scattered rather than stopping completely, or the result of secondary particles produced in the collimator itself.

Fig. 4.23 shows the results of lowering the bottom edge of the collimator material in Torus1. Fig. 4.23a shows the probability per POT that different types of particle (stopped muons and high momentum muons, pions, and electrons) pass the collimator as a function of the collimator height. On the other hand, Fig. 4.23b shows the same plots

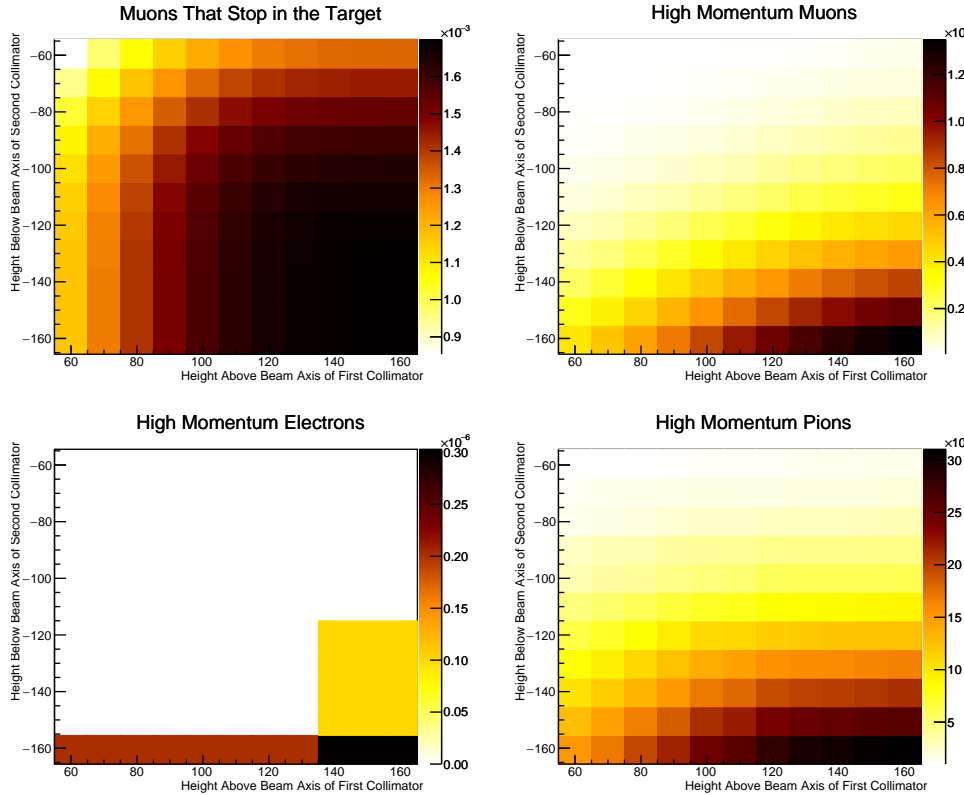


Figure 4.24.: The number of particles reaching the end of the Torus2 solenoid relative to the number that enter the Torus1 solenoid (i.e. the survival probability) for different heights of both collimators in Torus1 and Torus2.

but normalised to the total number of each particle type that reaches the collimator in the first place, therefore showing the survival probability along just the collimator region. Based on these plots, for a collimator that starts at 120 mm above the beamline axis, 14% of high momentum pions are removed, high momentum muons are suppressed by 14% whilst the muon stopping rate is reduced only by 3%.

For the second collimator at the exit to Torus2, the situation is slightly more complicated since in principle the optimum height could be correlated to the height of the upstream Torus1 collimator. To account for this, the virtual collimator technique was applied for both the Torus1 and Torus2 collimator sections simultaneously. As a result, the 1-dimensional plots of Fig. 4.23 become 2D as can be seen in Fig. 4.24, which is normalised to the particle flux just before the collimator similar to Fig. 4.23b.

Fig. 4.25 represents the stopping and high-momentum plots in a way that is easier to compare the two directly. Each line in that plot is a contour showing a change of 2.5 percentage points to the yield. Total acceptance, or 100% is in the bottom right

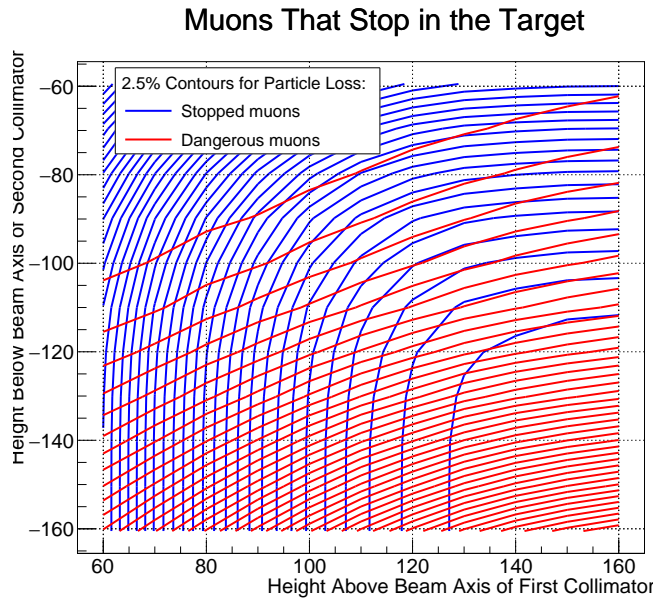


Figure 4.25.: 2.5% contours showing how changing the collimator height affects the stopped and high-momentum muon rates. Each contour represents a reduction of 2.5 percentage points to the particle flux, with 100% acceptance sitting in the bottom right. Blue lines represent the flux of stopping muons, whilst red lines represent the flux of high-momentum muons. For example, for collimator heights within the first blue contour towards the bottom-right corner, less than 2.5% of stopped muons are lost.

corner. From this plot it can be seen that whilst keeping more than 97.5% of the muon stopping rate (the bottom-right most blue contour), the maximum high momentum muon suppression is achieved when the Torus1 collimator sits about 140 mm above the beam axis, and the Torus2 collimator sits about 120 mm below it. To be precise, at these collimator values the muon stopping rate is kept at 99% of the no-collimator rate, whilst high momentum pions, muons and electrons drop to 27.6%, 20.9% and 11% (although this last value is very statistically limited) respectively, compared to their no-collimator rates. At this point the selected values for the collimator heights give conservative background suppressions and tighter values could be chosen. Given that backgrounds from high-momentum muons are suppressed compared to the actual rate of ‘dangerous’ muons by the geometric acceptance of the remaining beamlne and the timing and momentum cuts this seems reasonable at this stage although this will of course be investigated in the next chapter.

Finally, for comparison to the original plots, Fig. 4.26 shows the impact the new collimators have on the muon components of the beam. It is clear how greatly reduced the number of muons passing the stopping target region has now become.

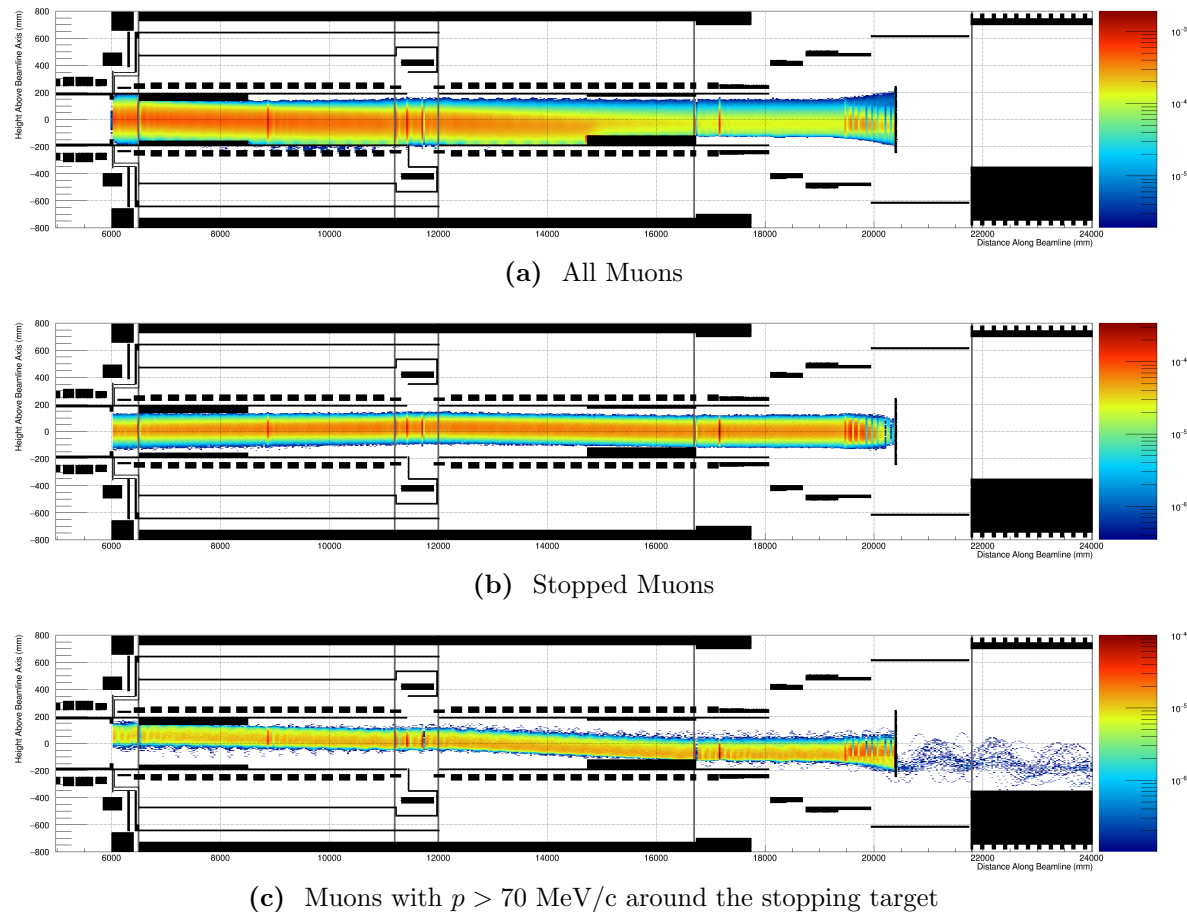


Figure 4.26.: The heights of muons as they pass along the beamline. (a) The path of all muons. (b): The paths of muons that stop in the target. (c): The heights of muons with momentum greater than 70 MeV/c when they enter the region around the stopping target. These could potentially decay in flight to give electrons with 100 MeV/c or greater. These plots should be compared to those of Fig. 4.21 before collimators were introduced, where it is clear how well the dangerous muons are being suppressed.

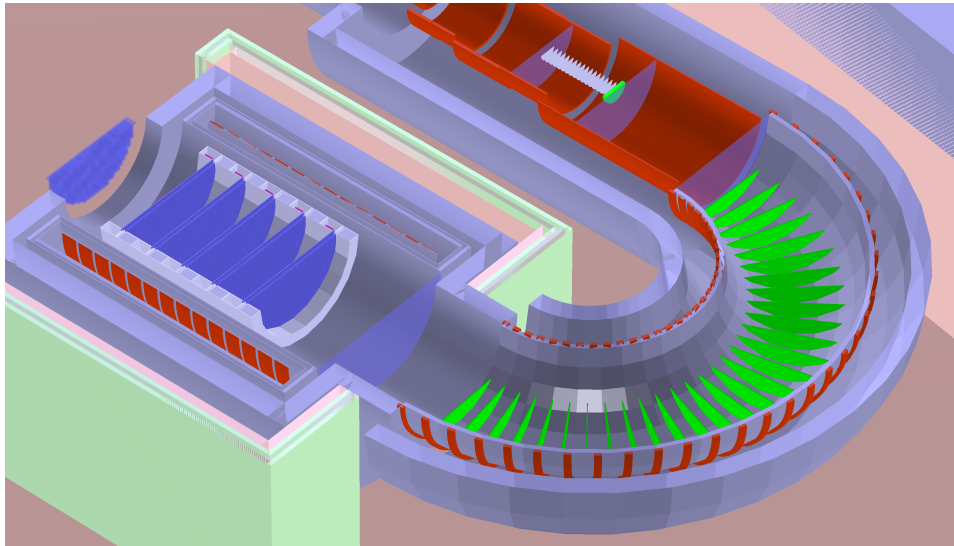


Figure 4.27.: Location of the beam blocker and one possible geometry for the DIO blockers, both highlighted in green, shown here before optimisation.

4.7. The Beam and Decay-in-Orbit Blockers

For every muonic atom formed in the stopping target some 39% will undergo decay in orbit (DIO). With some 1.4×10^8 POT per bunch and a muon stopping efficiency around 1.7×10^{-3} stops per POT, one can expect about 9×10^4 DIO events per bunch. If the detector system were exposed to this level of hits it would be impossible to resolve any signal electrons. However, above the end-point energy for electrons coming from free muon decay, the DIO spectrum falls extremely quickly, with around 99% of DIO electrons being produced with less than 59 MeV/c. To this end the electron spectrometer's primary purpose is to disperse away the electrons below 60 MeV/c whilst keep signal electrons on-axis, such that material in the beamline can be tuned to remove the low energy DIO electrons. The beam and DIO blockers are highlighted in green in Fig. 4.27.

Fig. 4.28 demonstrates the dispersion that appears at the end of the spectrometer with the nominal beam blocker design and no DIO blockers in place. The DIO blockers will be inserted along the bottom of the spectrometer and tuned to scrape away a sufficient number of DIO electrons, which will tend to travel towards the bottom of the beam pipe. However whilst the centre of gyration drifts with a well-behaved proportionality in a bent solenoid, the actual separation between signal and DIO electrons is in reality less clear as can be seen by the lower plot in Fig. 4.28.

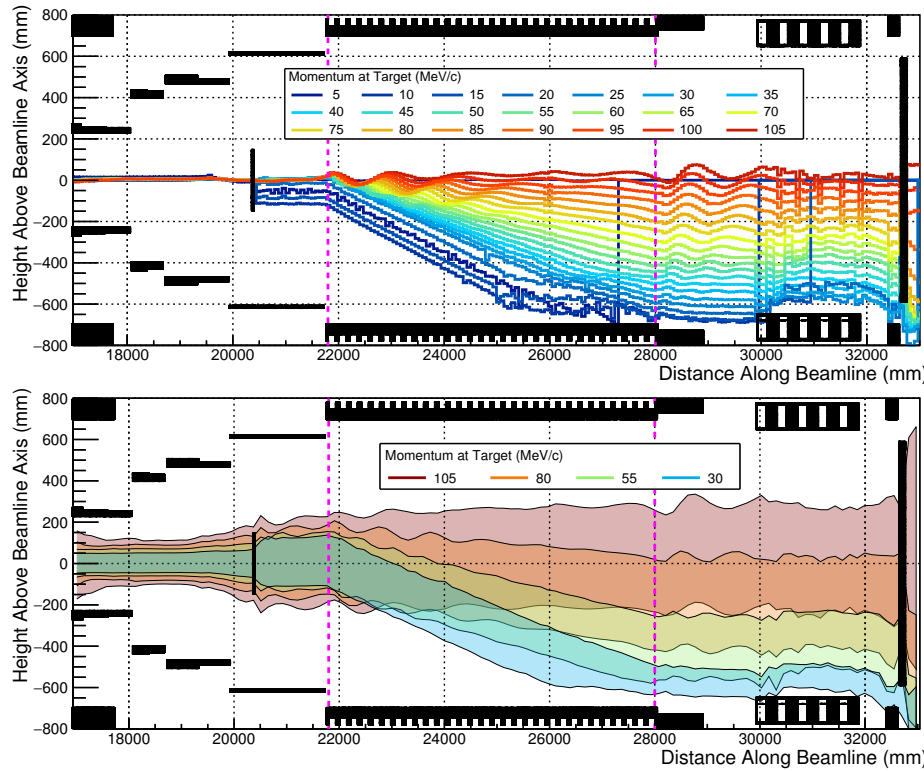


Figure 4.28.: Momentum-dependent dispersion of electrons passing through the spectrometer. Top plot: the mean height of different momenta electrons as a function beamline distance, showing how the drift of the centre of gyration is truly proportional to the momentum. Bottom plot: single standard deviation bands for electrons at different momentum, which shows how the envelope for different momenta overlap considerably, reducing the effectiveness of any collimators.

In addition to the DIO blockers along the spectrometer, the material of the beam blocker immediately after the stopping target also plays a role in suppressing the **DIO** rate since low energy electrons remain closer to the beam axis, as can be seen in the lower plot of Fig. 4.28 around the stopping target.

This section therefore describes a simultaneous optimisation of the beam blocker radius and the DIO blocker height. The overall goal is to suppress the DIO rate to less than a single DIO electron per bunch whilst maintain maximal signal acceptance. As for the muon beam collimators, we use the analysis-based collimator approach, where no blocking material is included during simulation. Instead a high-sampling density for particle trajectories is used such that during analysis particles and their secondaries can be ‘killed’ if they enter a region that would contain material of either the DIO or beam blocker.

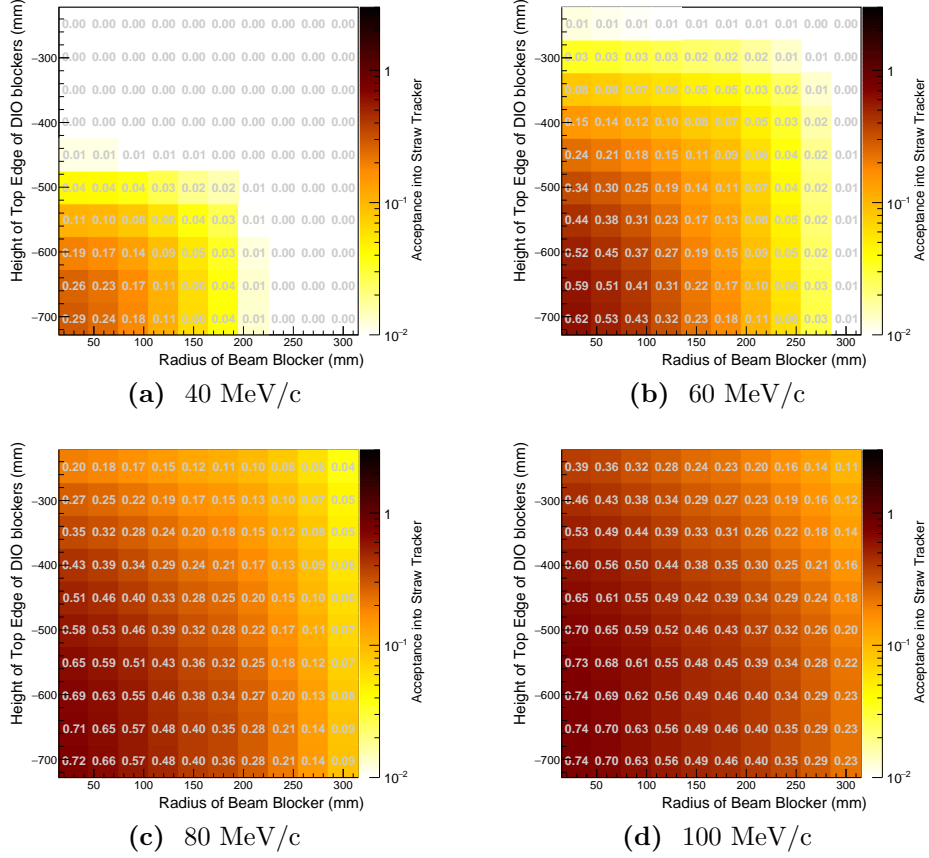


Figure 4.29.: Acceptance into the straw tracker for electrons with different momentum at the stopping target as a function of the beam and DIO blocker dimensions. Note the logarithmic scale for the colour bar.

The results of this study are shown in Fig. 4.29, where the geometric acceptance into the detector is shown for four different electron momenta as a function of the beam blocker radius and DIO blocker height. It is clear that for all values of the blockers' dimensions, electrons above 100 MeV/c have a much better acceptance.

The mean hit rate per DIO event is shown in Fig. 4.30a. It is formed by, for each combination of DIO and beam blocker dimension, the weighted integral of the acceptance of electrons as a function of momentum with the mean DIO rate in each momentum bin. To compare the hit rate to the acceptance of signal, the ratio between the hit rate and the high-momentum electron acceptance is shown in Fig. 4.30b. It is clear from this figure how quickly (note the logarithmic colour scale) the DIO hit rate is suppressed by increasing the DIO and beam blocker dimensions compared to the signal acceptance.

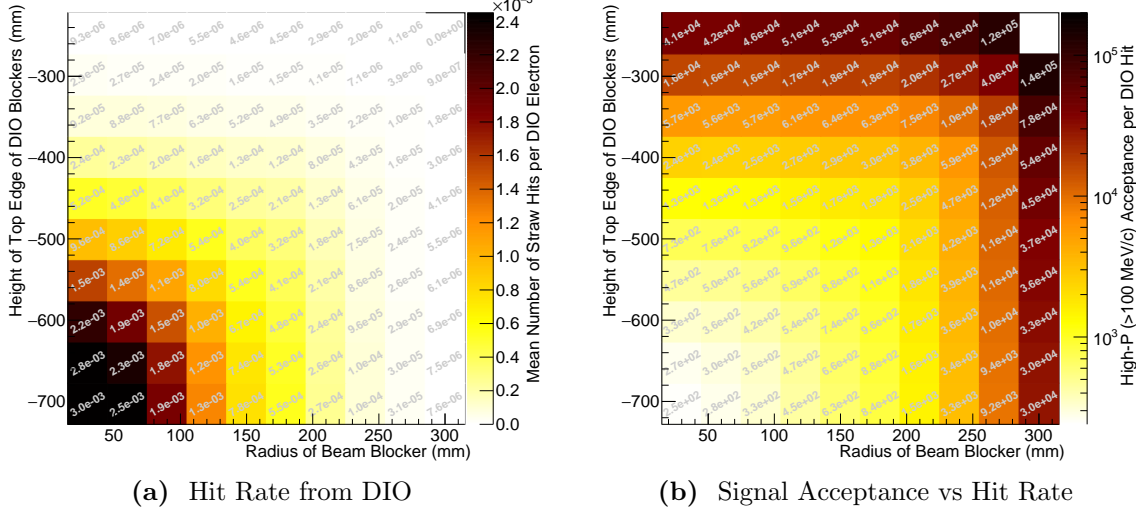


Figure 4.30.: (a) Number of straw tracker hits per DIO electron. (b) Ratio between the high-momentum electron ($p > 100$ MeV/c) acceptance to the number of hits per DIO electron. Colour is on a logarithmic scale.

With a beam blocker of 24 cm radius and DIO blockers set to 35 cm below the beam axis, the DIO hit rate is about 2.2×10^{-5} per DIO event, or about 2 DIO hits per bunch. For the same blocker dimensions, the geometric signal acceptance is about 0.22%. Given the steep drop-off in hit rate versus signal acceptance around these values a finer scan in this region is an important check for the future. What hit rate in the straw tracker is tolerable is a number for future studies. In Phase-I, the straw tracker is expected to operate with a hit rate around 1 kHz per straw. Phase-II will likely use finer straws, but with the current Phase-I design, some 133 straws occupy a layer, so that a total hit rate into the Straw Tracker of around 200 kHz should be acceptable.

Given the scope for future improvements in the granularity of the Phase-II straw tracker and the sensitivity to the beam and DIO blocker dimensions, the somewhat non-conservative values described above of 24 cm and 35 cm for beam blocker radius and DIO blocker depth below the beam axis are selected here.

4.8. Summary of optimised parameters

The complete set of optimised parameters is shown in Table 4.4.

Parameter	Value	Comments
Production Target Length	32 cm	Placed asymmetrically about muon beamline axis
Production Target Radius	1 cm	
Torus1 (TS2) Dipole Strength	0.055 T	same as Phase-I
Torus2 (TS4) Dipole Strength	0.0275 T	same as Phase-I
Torus1 Entrance Collimator Height	14 cm above beam axis	From top of beam pipe downwards
Torus2 Exit Collimator Height	12 cm below beam axis	From bottom of beam pipe upwards
Stopping Target Location	0 cm	Unchanged from CDR value
Electron Spectrometer Dipole	-0.18 T	Negative compared to Torus1 and Torus2 dipole fields
Beam Blocker Radius	24 cm	
DIO Blocker Height	35 cm below beam axis	From bottom of spectrometer upwards

Table 4.4.: Optimised values for the parameters studied in this chapter. Many more parameters remain to be optimised that were considered beyond the scope of the present work.

4.9. Future optimisations

The primary goal of this work is to update the previous optimisation from the 2009 CDR and provide a new baseline design. However whilst touching every aspect of the layout of Phase-II, the optimisation developed here is not exhaustive and there is much scope for further work.

The following list is a short summary of some of the areas that could be developed further:

Refine the optimisation criteria In many of these studies only the signal efficiency, or even some proxy, is used to identify the optimal value of the parameter under question. In reality one ought also to study simultaneously the background rates. These two quantities should be combined into the expected confidence limits given a null or background-only measurement. At the same time other quantities such as

cost and run-time will also need considering, although the latter is likely reduced simultaneously with maximising the overall sensitivity.

High energy electron acceptance vs. beamline distance When tuning the muon beam collimators, the key goal is to remove high-energy particles that can produce high energy electrons. A particularly useful study would be to evaluate the acceptance to signal-like electrons which originate along the beamline. This should include those electrons which originate with momentum greater than 105 MeV/c but which arrive at the detector with signal-like energies. With this information, it becomes easier to identify how soon along the beamline one must collimate away the high-energy particles which may lead to improvements in the muon stopping rate or the signal acceptance.

Stopping target shape, thickness, and disk spacing This study has focussed only on the position of the stopping target. Clearly the actual shape should be studied as well. In particular, given the dispersion in the muon beam, and the changing solenoidal field strength around the target, a target design that uses disks of varying profile or even thickness has potential to improve the experimental sensitivity.

Correlation between dipole fields and stopping target shape Since the bent solenoids introduce dispersion into the beam and the dipole fields compensate for this, the height and momentum of the muon beam at the stopping target can be controlled to a degree. Whilst in the optimisation of the muon beam dipoles of this thesis the target shape was held fixed, in principle some of the identified correlations might be different if the target design was allowed to vary simultaneously. Such a study would clearly involve an enormous parameter space, so perhaps this is a study that could be best performed with a smarter machine-learning based approach.

Spectrometer's solenoidal field strength and aperture Since the dispersive effect of a bent solenoid is inversely proportional to the solenoidal field strength, reducing the field in the spectrometer will likely improve the DIO–signal separation, reducing the hit rate. This could however also affect the signal acceptance since the trajectories will acquire larger envelopes. Increasing the spectrometer aperture size could compensate this, but then one faces an increase in the cost of the spectrometer and the detector solenoid which would need to be considered.

Chapter 5.

Phase-II Signal Sensitivity

Chapter 6.

Phase-II Backgrounds

6.1. Antiproton Induced Backgrounds

Antiprotons can be produced when the primary 8 GeV proton beam interacts with the production target, creating a proton-antiproton pair:

$$p + N(A, Z) \rightarrow p + N^*(A, Z) + p + \bar{p} \quad (6.1)$$

Given their relatively large mass, antiprotons travel much more slowly than other products of the same momentum which results in a smearing of the beam's time-structure for antiprotons and their secondaries. The pulsed beam and time-gated detector window are therefore not effective at suppressing the induced backgrounds.

6.1.1. Antiproton Production Rate and Spectrum

There is really very little literature on the production of antiprotons from a tungsten target for a range of angles. Accordingly most hadron models are particularly under-constrained when it comes to antiproton production, and indeed the QGSP_BERT_HP model used as the basis for SimG4 is completely unable to produce antiprotons.

In the COMET TDR....

Although tungsten targets seem not to have been studied at all at the right angles and proton energies, a set of papers [12, 24] do exist covering antiproton production up to 2 radians for a tantalum target (which is adjacent to tungsten on the periodic table) and with 10 GeV protons. These measurements provide the invariant triple-differential

cross section as a function of antiproton momentum for production angles of 10, 59, 97 and 119°, defined as:

$$F(p, \theta, \phi) = E \frac{d^3\sigma}{dp^3} = E \frac{d^3\sigma(p, \theta, \phi)}{p^2 dp d\Omega} \quad (6.2)$$

$$f = F/A \quad (6.3)$$

where A is the relative atomic mass of the nucleus, E and p the antiproton energy and momentum. Fig. ?? shows the data from these papers. In much the same way as for pion production, it is clear the spectrum becomes considerably softer whilst the overall rate falls quickly as you move to larger angles. To convert the differential invariant cross sections given in the literature into a differential production rate per POT, $d^3R(\theta)/dpd\Omega$, the following formula is used:

$$\frac{d^3R(p, \theta, \phi)}{dp^3} = \frac{F(p, \theta, \phi)}{E} \frac{\rho N_A l}{m_N} \quad (6.4)$$

where ρ is the mass density of the target, 19.25 g/cm³ for Tungsten, m_N the atomic mass, 183.86 g/mol for tungsten, l the length of the target, and N_A is Avodadro's number.

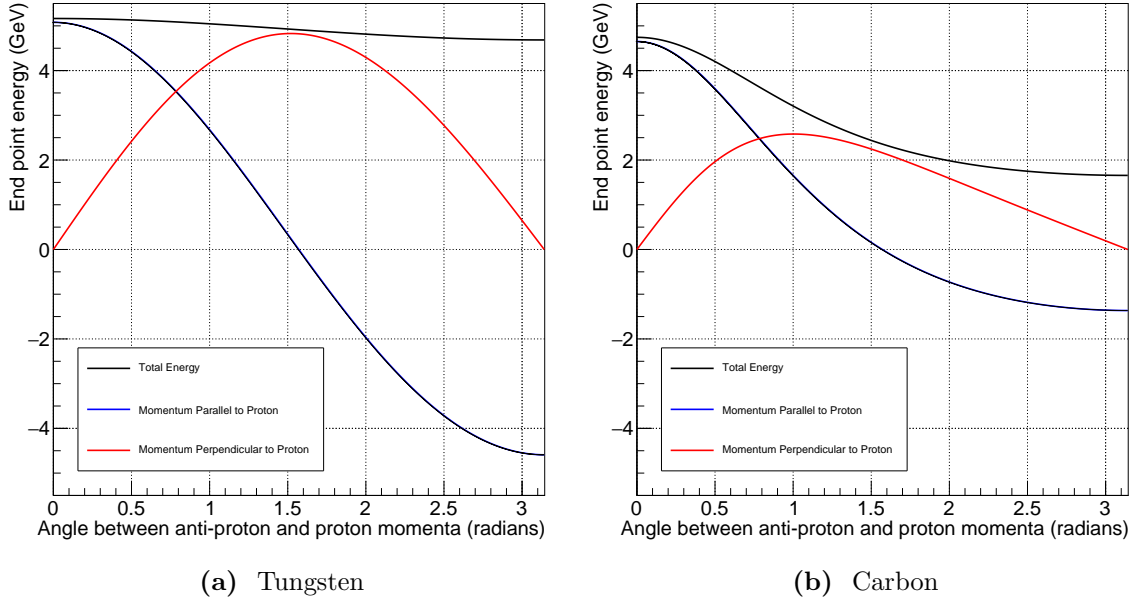


Figure 6.1.: The kinematic end-point for antiproton production as a function of the out-going antiproton direction with respect to the incoming proton in the frame of the target nucleus (the lab frame). The absolute end-point is only achieved when the nucleus and out-going protons recoil coherently.

To build the limited number of data-points from this paper into a complete but conservative spectrum, empirical fits to the data were performed after adding two data points for the minimum and maximum momentum. The minimum momentum only added the constraint that at zero momentum the cross section also be zero. On the other hand, to calculate the maximum momentum the kinematic end-point was found by considering the entire nucleus and two out-going protons to recoil directly against the antiproton. The value of the end-point kinetic energy and longitudinal and transverse momenta for tungsten and carbon are shown in Fig. ?? using the formulae derived in appendix ???. This end-point will be a highly conservative estimate, since in reality not all the nucleus will recoil coherently; the de Broglie wavelength for a proton with 8 GeV kinetic energy is about 0.15 fm, compared to the 7 fm or so of a tungsten nucleus. Additionally, achieving this end-point configuration would be highly phase-space suppressed.

With the addition of these two end-points a fit was constructed by fitting the data up to the final measured point with a polynomial of order 4 to 6 (depending on the number of available data points). For the high-momentum tails of each spectrum two fits were tried: a straight line fit between the last measured value and the kinematic end-point described above; and an exponential plus constant fitted to the end-point and last two data points. Fig. ?? shows the results of this fitting procedure, where it can be seen that a low momentum peak is visible and a high momentum tail well described. Whilst these spectra are very likely not an accurate representation of the true production spectrum, they serve as useful upper bounds which can be used as inputs to estimate the antiproton background rate.

Region	Data source	Fitted Momentum Function	Total \bar{p} per POT
$0 \leq \theta < 59^\circ$	10° [24]		5.32×10^{-4}
$59 \leq \theta < 97^\circ$	59° [24]		2.80×10^{-8}
$97 \leq \theta < 119^\circ$	97° [12]		2.39×10^{-12}
$119 \leq \theta < 180^\circ$	119° [12]		1.22×10^{-12}

Table 6.1.: Regions and fits used to simulate antiproton production. The values in the final column are result of converting to rates per POT and integrating the differential cross-sections measured in [12, 24].

6.1.2. Simulating Antiprotons

To study the resultant backgrounds, antiprotons were generated uniformly in the production target. Four separate simulations were run, corresponding to the four angular regions given in the data, as shown in Table 6.1. For each simulation, antiprotons were generated isotropically within a cone parallel to the incoming proton beam, with minimum and maximum values of theta defined by the angular region being studied. The momentum distribution used the fitting procedure described above for the angle at the lower edge of the region (for the region from 0 – 59°, the fit to the 10° data was used).

Given the strong angular dependence visible from the measurements, events were reweighted based on the angle between the initial antiproton direction and the proton beam. The combined procedure of generating isotropically with a momentum distribution based on the fit to the data, then reweighting based on the angle, amounts to the following factorisation of the measured differential cross section:

$$F(p, \theta, \phi) = \left(\frac{E}{p^2} \frac{dP(p)}{dp} \right) \left(\frac{1}{2\pi} \frac{d\Phi(\theta)}{d\theta} \right) \quad (6.5)$$

For a given value of θ the momentum distribution dP/dp is chosen to match the first spectrum measured at a larger value of θ . When these distributions are used to generate particles they are essentially normalised so their integral is unity. $d\Phi/d\theta$ is then used to vary the overall normalisation as a function of theta. Boyarinov et al. state [12] that the angular dependence will take the form:

$$\frac{d\Phi(\theta)}{d\theta} = \alpha e^{\beta \cos \theta} \quad (6.6)$$

where α and β are constants. Fig. ?? shows how the integrals of the fitted spectra vary with the measured angles.

This factorisation injects the assumption that the momentum distribution at a given angle is independent of the angle. Whilst this should not be the case for a realistic spectrum, to produce limits on the background rate it is a valid assumption. The ϕ dependence of $\Phi(\theta, \phi)$ is assumed constant.

6.1.3. Antiproton Transmission

Fig. ?? shows how antiprotons are transmitted along the beamline. Material at the join between the production target capture region and the first bent muon transport solenoid designed to keep the vacuum seal and cryogenic conditions is also acting to remove antiprotons. Fig. ?? shows the timing of antiprotons reaching the entrance of the bent muon transport solenoid.

Based on these simulations, the probability that an antiproton will enter the bent muon transport solenoid is well less than XXXX per POT.

6.1.4. Delayed Pion Production

A larger

5. Pion stops per pion passing Torus2 monitor = 3.21826657700288808e-04

6. RPC background rates:

6.1. Prob. of RPC = 2.15% per stopped pion

6.2. Prob. of RPC producing signal-like electron in detector = 1.05e-5 per RPC event

7. Total probability of RPC event per pion passing Torus2 monitor = 7.26523679758401863e-11

8. Number of pions at Torus2 monitor:

8.1. For region 1 ($0 - 59^\circ$): 2.1e-9 pions per antiproton in this range

9. Total backgrounds from pions from antiprotons:

9.1. For region 1: $5.32\text{e-}4 * 2.1\text{e-}9 * 7.3\text{e-}11 = 8.5\text{e-}23$ per POT

10. Assumes no timing cut, but actually timing cut will help reduce this

Appendix A.

Drifts in a Bent Solenoid

The Lorentz force:

$$\frac{d\vec{p}}{dt} = \frac{q}{m} \vec{p} \times \vec{B} \quad (\text{A.1})$$

A.1. Uniform Solenoidal Field

B field is uniform and parallel to axis of solenoid. Define the Larmor frequency, ω , and radius, a , as:

$$a = \frac{\gamma m \vec{v} \times \vec{B}}{qB^2} = \frac{p_T}{qB} \quad (\text{A.2})$$

$$\omega = \frac{qB}{m} \quad (\text{A.3})$$

A.2. Field in a Bent Solenoid

Producing a cylindrical solenoid channel can be imagined as directly bending that of a normal uniform and linear one. By symmetry it can be seen that any gradient introduced to the magnetic field can only be radially, in the plane of the bending. Further, by considering Ampere's law with a current loop in the plane of bending formed by two radial straight lines (with length $|r - R| < L$, where R and L are the bending and aperture radii of the solenoid channel) and an arc, it can be seen that the variation in

the field is given by:

$$\frac{\nabla \vec{B}}{B} = \frac{1}{r} \hat{r} \quad (\text{A.4})$$

((CHECK: Sketch or figure?))

A.3. Drift Calculation

There are two sources of drift in a bent solenoid: the gradient in the field, and the centrifugal force arising from the circular coordinate system needed to describe the field lines. The two can be treated separately in the sense that the motion of a particle moving through a field with straight field lines but with a transverse gradient given by $\nabla B/B \propto 1/r$ would be described by an equation of motion equivalent to that from the first source of drift in the bent solenoid system. Similarly, a system with a uniform field but field lines that follow circular paths would exhibit drift equivalent to the second component mentioned above.

A.3.1. Gradient Drift

“Grad-B” drift is well described in text books, but in the interest of completeness a short derivation shall be given here. The drift arising due to the gradient in the field can be treated as a perturbation of the motion of the particle in a uniform solenoidal field. The total velocity \vec{V} , is given by:

$$\vec{V} = \vec{v} + \vec{v}_g, \quad (\text{A.5})$$

where \vec{v} is the unperturbed velocity of the particle in the transverse plane, and \vec{v}_g is the velocity arising due to the gradient in the field.

Treating the field as a Taylor expansion:

$$\vec{B}(\vec{r}) = \vec{B}_0 + (\vec{r} \cdot \nabla)|_{\vec{r}=0} \vec{B} + \dots \quad (\text{A.6})$$

and substituting equations (A.5) and (A.6) into the Lorentz force, gives:

$$m \frac{d(\vec{v} + \vec{v}_g)}{dt} = q(\vec{v} + \vec{v}_g) \times \left(\vec{B}_0 + (\vec{r} \cdot \nabla)|_{\vec{r}=0} \vec{B} \right) \quad (\text{A.7})$$

$$(\text{A.8})$$

so that to first order, the perturbing velocity is given by:

$$\frac{d\vec{v}_g}{dt} = \frac{q}{m} \left(\vec{v} \times (\vec{r} \cdot \nabla)|_{\vec{r}=0} \vec{B} + \vec{v}_g \times \vec{B}_0 \right) \quad (\text{A.9})$$

Since we are only interested in steady-state solutions where \dot{v}_g is close to zero, the above equation gives:

$$\vec{v}_g = \frac{q}{m} \frac{\vec{B}_0 \times \left(\vec{v} \times (\vec{r} \cdot \nabla)|_{\vec{r}=0} \vec{B} \right)}{B_0^2} \quad (\text{A.10})$$

which by considering the form after time averaging becomes:

$$\langle \vec{v}_g \rangle_t = \frac{\vec{B}_0 \times \left(\vec{v} \times (\vec{r} \cdot \nabla)|_{\vec{r}=0} \vec{B} \right)}{B_0^2} \quad (\text{A.11})$$

Appendix B.

Kinematic End-point for Anti-proton Production

Appendix C.

Revisiting the Stopping Target Region

List of Acronyms

CDC Cylindrical Drift Chamber

CDR Conceptual Design Report

CERN Organisation européenne pour la recherche nucléaire

CyDet Cylindrical Detector

DIO decay in orbit

JFY Japanese Fiscal Year

J-PARC the Japanese Proton Accelerator Research Complex

LYSO Cerium-doped Lutetium Yttrium Oxyorthosilicate

MR J-PARC Main Ring

PID Particle Identification

POT Protons on Target

RCS J-PARC Rapid Cycling Synchrotron

SES Single-Event Sensitivity

SM Standard Model

StrECAL Straw tube tracker and Electromagnetic Calorimeter

TDR Technical Design Report

Bibliography

- [1] see: <http://ilcsoft.desy.de/marlin>.
- [2] see: <http://www.cmtsite.org>. No longer maintained.
- [3] see: <http://www.cmake.org>.
- [4]
- [5] MIDAS (Maximum Integration Data Acquisition System). <http://midas.psi.ch>. Accessed: 22-May-2015.
- [6] K. Abe, N. Abgrall, H. Aihara, Y. Ajima, J.B. Albert, and D. Allan. The t2k experiment. *Nuclear Instruments and Methods in Physics Research Section A: Accelerators, Spectrometers, Detectors and Associated Equipment*, 659(1):106 – 135, 2011.
- [7] S. Agostinelli, J. Allison, K. Amako, J. Apostolakis, H. Araujo, P. Arce, M. Asai, D. Axen, S. Banerjee, G. Barrand, F. Behner, L. Bellagamba, J. Boudreau, L. Broglia, A. Brunengo, H. Burkhardt, S. Chauvie, J. Chuma, R. Chytracek, G. Cooperman, G. Cosmo, P. Degtyarenko, A. Dell'Acqua, G. Depaola, D. Dietrich, R. Enami, A. Feliciello, C. Ferguson, H. Fesefeldt, G. Folger, F. Foppiano, A. Forti, S. Garelli, S. Giani, R. Giannitrapani, D. Gibin, J.J. Gmez Cadenas, I. Gonzlez, G. Gracia Abril, G. Greeniaus, W. Greiner, V. Grichine, A. Grossheim, S. Guatelli, P. Gumlplinger, R. Hamatsu, K. Hashimoto, H. Hasui, A. Heikkinen, A. Howard, V. Ivanchenko, A. Johnson, F.W. Jones, J. Kallenbach, N. Kanaya, M. Kawabata, Y. Kawabata, M. Kawaguti, S. Kelner, P. Kent, A. Kimura, T. Kodama, R. Kokoulin, M. Kossov, H. Kurashige, E. Lamanna, T. Lampn, V. Lara, V. Lefebure, F. Lei, M. Liendl, W. Lockman, F. Longo, S. Magni, M. Maire, E. Medernach, K. Minamimoto, P. Mora de Freitas, Y. Morita, K. Murakami, M. Nagamatu, R. Nartallo, P. Nieminen, T. Nishimura, K. Ohtsubo, M. Okamura, S. O'Neale, Y. Oohata, K. Paech, J. Perl, A. Pfeiffer, M.G. Pia, F. Ranjard, A. Rybin, S. Sadilov, E. Di Salvo, G. Santin, T. Sasaki, N. Savvas, Y. Sawada, S. Scherer, S. Sei, V. Sirotenko, D. Smith, N. Starkov, H. Stoecker, J. Sulkimo, M. Takahata, S. Tanaka, E. Tcherniaev, E. Safai Tehrani, M. Tropeano, P. Truscott, H. Uno, L. Urban, P. Urban, M. Verderi, A. Walkden, W. Wander, H. Weber, J.P. Wellisch, T. Wenaus, D.C. Williams, D. Wright, T. Yamada, H. Yoshida, and D. Zschiesche. Geant4 - a simulation toolkit. *NIM in PRS A*, 506(3):250 – 303, 2003.
- [8] AlCap Collaboration. Study of muon capture for muon to electron conversion ex-

- eriments. http://muon.npl.washington.edu/exp/AlCap/R-13-03.1_BV44.pdf. Accessed: 28-October-2015.
- [9] D. Armutliiski, Ts. Baatar, Ts. Batsaikhan, T. Kanarek, E.N. Kladnitskaya, M.U. Sultanov, R. Togoo, G.P. Toneeva, and D. Tuvdendorzh. Hadron spectra in hadron - nucleus collisions. 1991.
 - [10] G. Barrand, I. Belyaev, P. Binko, M. Cattaneo, R. Chytracek, et al. GAUDI - A Software Architecture and Framework for Building HEP Data Processing Applications. *Comput.Phys.Commun.*, 140:45–55, 2001.
 - [11] Wilhelm H. Bertl et al. A Search for muon to electron conversion in muonic gold. *Eur.Phys.J.*, C47:337–346, 2006.
 - [12] S. V. Boyarinov, I. I. Evseev, Yu. T. Kiselev, G. A. Leksin, A. N. Martemyanov, K. R. Mikhailov, S. A. Pozdnyakov, Yu. V. Terekhov, V. I. Ushakov, and V. A. Sheinkman. Yields of p, anti-p, pi+-, and K+- emitted at an angle of 97-degrees in the laboratory system from nuclei irradiated by 10.14-GeV protons. *Phys. Atom. Nucl.*, 57:1379–1388, 1994. [Yad. Fiz.57,1452(1994)].
 - [13] R. Brun, A. Gheata, and M. Gheata. The ROOT geometry package. *Nucl. Instrum. Meth.*, A502:676–680, 2003.
 - [14] M. G. Catanesi et al. The HARP detector at the CERN PS. *Nucl. Instrum. Meth.*, A571:527–561, 2007.
 - [15] COMET Collaboration. Conceptual design report for experimental search for lepton violating μ^-e^- conversion at sensitivity of 10^{-16} with a slow-extracted bunched proton beam (COMET), J-PARC P21.
 - [16] Comet group on Gitlab. <https://gitlab.in2p3.fr/comet>.
 - [17] Andrzej Czarnecki, Xavier Garcia i Tormo, and William J. Marciano. Muon decay in orbit: Spectrum of high-energy electrons. *Phys.Rev.*, D84(1):013006, 2011.
 - [18] Rashid M. Djilkibaev. Meco muon yield simulation using experimental data. Technical report, Department of Physics and Astronomy, University of California.
 - [19] Andrew Williams John Edmonds. *An Estimate of the Hadron Production Uncertainty and a Measurement of the Rate of Proton Emission after Nuclear Muon Capture for the COMET Experiment*. PhD thesis, U. Coll. London, 2015.
 - [20] Alfredo Ferrari, Paola R. Sala, Alberto Fasso, and Johannes Ranft. FLUKA: A multi-particle transport code (Program version 2005). 2005.
 - [21] G4Beamline. G4beamline homepage. 2009. <http://www.muonsinternal.com/muons3/G4beamline>.
 - [22] C. Hoppner, S. Neubert, B. Ketzer, and S. Paul. A Novel Generic Framework for Track Fitting in Complex Detector Systems. *Nucl. Instrum. Meth.*, A620:518–525,

2010.

- [23] H. Iwase, K. Niita, and T. Nakamura. Development of general-purpose particle and heavy ion transport monte carlo code. *Journal of Nuclear Science and Technology*, 39(11):1142–1151, 2002.
- [24] Yu. T. Kiselev, V. A. Sheinkman, A. V. Akindinov, M. M. Chumakov, A. N. Martemyanov, V. A. Smirnitsky, Yu. V. Terekhov, and E. Ya. Paryev. Probing of compact baryonic configurations in nuclei in $A(p, \bar{p})X$ reactions and antiproton formation length in nuclear matter. *Phys. Rev.*, C85:054904, 2012.
- [25] Ben Krikler, Ajit Kurup, Yoshi Uchida, Andrew Edmonds, Phill Litchfield, and the COMET Collaboration Software Group. Icedust conventions. *Internal Document*.
- [26] Robert K Kutschke. art: A framework for new, small experiments at fermilab. *Journal of Physics: Conference Series*, 331(3):032019, 2011.
- [27] Nikolai V. Mokhov. The MARS code system user’s guide version 13(95). 1995.
- [28] T. Suzuki, D. F. Measday, and J. P. Roalsvig. Total nuclear capture rates for negative muons. *Phys. Rev. C*, 35:2212–2224, Jun 1987.
- [29] The COMET Collaboration. COMET Phase-I: Technical Design Report. Technical report, KEK, April 2016.
- [30] Nam Hoai Tran. A Study of Proton Emission Following Nuclear Muon Capture for the COMET Experiment. *Thesis*, 2014.
- [31] D. H. Wright and M. H. Kelsey. The Geant4 Bertini Cascade. *Nucl. Instrum. Meth.*, A804:175–188, 2015.